Doctoral Dissertation

ELECTROKINETICS-ASSISTED ELECTRICAL SENSORS FOR RAPID DETECTION OF BACTERIA

Chang-Ho Han

Department of Mechanical Engineering
(Mechanical Engineering)

Ulsan National Institute of Science and Technology

2021

ELECTROKINETICS-ASSISTED ELECTRICAL SENSORS FOR RAPID DETECTION OF BACTERIA

Chang-Ho Han

Department of Mechanical Engineering
(Mechanical Engineering)

Ulsan National Institute of Science and Technology

Abstract

An array of microfabricated interdigitated electrodes (IDEs) is the most commonly used form of electrode geometry for dielectrophoretic manipulation of biological particles in microfluidic biochips owing to simplicity of fabrication and ease of analysis. However, the dielectrophoretic force dramatically reduces as the distance from the electrode surface increases; therefore, the effective region is usually close to the electrode surface for a given electric potential difference. Here, I present a novel two-dimensional computational method for generating planar electrode patterns with enhanced volumetric electric fields, which I call the "microelectrode discretization (MED)" method. It involves discretization and reconstruction of planar electrodes followed by selection of the electrode pattern that maximizes a newly defined objective function, factor S, which is determined by the electric potentials on the electrode surface alone. In this study, IDEs were used as test planar electrodes. Two arrays of IDEs and respective MED-optimized electrodes were implemented in microfluidic devices for the selective capture of *Escherichia coli* against 1-μm-diameter polystyrene beads, and I experimentally observed that 1.4 to 35.8 times more bacteria were captured using the MED-optimized electrodes than the IDEs ($p < 0.0016$), with a bacterial purity against the beads of more than 99.8%. This simple design method offered simplicity of fabrication, highly enhanced electric field, and uniformity of particle capture, and can be used for many dielectrophoresis-based sensors and microfluidic systems.

Dielectrophoresis (DEP) is usually effective close to the electrode surface. Several techniques have been developed to overcome its drawbacks and to enhance dielectrophoretic particle capture. Here a simple technique was presented of superimposing alternating current DEP (high-frequency signals) and electroosmosis (EO; low-frequency signals) between two coplanar electrodes (gap: 25 μm) using a lab-made voltage adder for rapid and selective concentration of bacteria, viruses, and proteins, where the voltages and frequencies of DEP and EO were controlled separately. This signal superimposition technique enhanced bacterial capture (*Escherichia coli* K-12 against 1-μm-diameter polystyrene beads) more selectively (>99 %) and rapidly (~30 s) at lower DEP (5 Vpp) and EO (1.2 Vpp) potentials than those used in the conventional DEP capture studies. Nanometer-sized MS2 viruses and troponin I antibody proteins were also concentrated using the superimposed signals, and significantly more MS2 and cTnI-Ab were captured using the superimposed signals than the DEP (10 Vpp) or EO (2 Vpp) signals alone ($p < 0.035$) between the two coplanar electrodes and at a short exposure time (1 min). This technique has several advantages, such as simplicity and low cost of electrode fabrication, rapid and large collection without electrolysis.

Electrokinetic technologies such as AC electro-osmosis (EO) and dielectrophoresis (DEP) have been used for effective manipulation of bacteria to enhance the sensitivity of an assay, and many previously reported electrokinetics-enhanced biosensors are based on stagnant fluids. An effective region for positive DEP for particle capture is usually too close to the electrode for the flowing particles

to move toward the detection zone of a biosensor against the flow direction; this poses a technical challenge for electrokinetics-assisted biosensors implemented within pressure-driven flows, especially if the particles flow with high speed and if the detection zone is small. Here, a microfluidic single-walled carbon nanotubes (SWCNTs)-based field-effect transistor immunosensor was presented with electrohydrodynamic (EHD) focusing and DEP concentration for continuous and label-free detection of flowing *Staphylococcus aureus* in a 0.01× phosphate buffered saline (PBS) solution. The EHD focusing involved AC EO and negative DEP to align the flowing particles along lines close to the bottom surface of a microfluidic channel for facilitating particle capture downstream in the detection zone. For feasibility, 380-nm-diameter fluorescence beads suspended in 0.001× PBS were tested, and 14.6 times more beads were observed to be concentrated on the detection area with EHD focusing. Moreover, label-free, continuous, and selective measurement of *S. aureus* in 0.01× PBS was demonstrated, showing good linearity between the relative changes in electrical conductance of the SWCNTs and logarithmic *S. aureus* concentrations, a capture/detection time of 35 min, and limit of detection of 150 CFU/mL, as well as high specificity through electrical manipulation and biological interaction.

Table of Contents

List of Figures and Tables

Nomenclature

2D: two-dimensional
3D: three-dimensional
Ab: antibody
AC: alternating current
AHA: azidohomoalanine
ANOVA: analysis of variance
CCD: charge-coupled device
CFU: colony forming unit
CM: Clausius-Mossotti
CTB: cholera toxin subunit B
cTnI: cardiac troponin I
DAPI: 4',6-diamidino-2-phenylindole
DEP: dielectrophoresis
DI: deionized
EDC: N-(3-dimethylaminopropyl)-N'-ethylcarbodiimidehydrochloride
EHD: electrohydrodynamic
EO: electroosmosis
EP: electrophoresis
ET: electrothermal
FDM: finite difference method
FEM: finite element method
FET: field-effect transistor
FITC: fluorescein isothiocyanate
IDE: interdigitated electrode
ITO: indium tin oxide
LB: Luria-Bertani
LoD: limit of detection
MED: microelectrode discretization
nDEP: negative dielectrophoresis
NHS: N-hydroxysuccinimide
PBS: phosphate buffered saline
pDEP: positive dielectrophoresis
PFU: plaque forming unit

PS: polystyrene

RCC: relative electrical conductance change

Rh-B: rhodamine B

RoI: region of interest

S/N: signal-to-noise ratio

SRC: stabilized relative electrical conductance change

SWCNT: single-walled carbon nanotube

twDEP: traveling-wave dielectrophoresis

d_p: diameter of particle

$\overline{E}$: electric field intensity vector

$\overline{E}_{rms}$: root-mean-squared electric field intensity vector

$\overline{F}_{ACET}$: alternating current electrothermal force vector

$\overline{F}_{buoyancy}$: buoyant force vector

$\overline{F}_{DEP}$: dielectrophoretic force vector

$\overline{F}_{drag}$: drag force vector

$\overline{F}_{gravity}$: gravitational force vector

f_{CM}: CM factor

$\overline{g}$: gravity vector

m_p: mass of particle

r_p: radius of particle

$\underline{\nabla T}$: temperature gradient vector

$\overline{u}$: flow velocity vector

v_{ACEO}: electroosmotic slip flow velocity

$\overline{x}_p$: position vector of particle

ε_m: electrical permittivity of medium

ε_p: electrical permittivity of particle

λ_D: Debye length

μ: dynamic viscosity

ρ_p: density of particle

φ: electric potential

φ_0: initial potential

Ω: non-dimensional frequency

ω: angular frequency

Chapter 1. Introduction

1.1. Dielectrophoresis with Planar Microelectrodes

Dielectrophoresis (DEP) is the movement of a polarizable particle in a non-uniform electric field, and it is extensively used for manipulating or collecting micrometer- and nanometer-sized particles. It usually involves microfabricated electrodes such as interdigitated (Li Bashir 2002; Del Moral-Zamora *et al.* 2015), spiral (Wang *et al.* 1997), polynomial (Gagnon *et al.* 2010), square microwell (Rosenthal Voldman 2005), castellated (Ramadan *et al.* 2006), slanted (Wei *et al.* 2014), and curved (Khoshmanesh *et al.* 2009) electrodes, and an array of interdigitated electrodes (IDEs) is most commonly used due to its simple fabrication and ease of analysis. However, the DEP force over these electrodes decreases exponentially with distance from the electrode surface; hence DEP is usually effective close to the electrode surface for a given applied electric potential (Das *et al.* 2005; Gadish Voldman 2006).

To maximize the DEP-effective region towards high-throughput and highly effective particle manipulation, many studies have been conducted on the development of new electrodes. In recent years, three-dimensional (3D) electrodes have been presented, such as vertical electrodes (Voldman *et al.* 2002; Demircan *et al.* 2015) and top-bottom electrodes (Dürr *et al.* 2003; Tada *et al.* 2016); however, these electrodes can be difficult to implement because of difficulties in alignment, complicated fabrication processes, and relatively high cost (Li *et al.* 2014). Insulator-based DEP has also been developed to generate non-uniform electric fields throughout the entire channel height along with chemically inertness (Nakano *et al.* 2015) using glass, silicon, and polymers. However, high external voltages, for example up to an order of a kilovolt, may need to be applied to the fluid reservoirs of these devices along with the additional safety consideration (Chou *et al.* 2002; Lapizco-Encinas *et al.* 2003) and Joule heating throughout the entire channel length (Zellner *et al.* 2013).

Novel planar electrode patterns that can generate higher electric fields than those generated by conventional IDEs without complicated fabrication processes and large external electric power consumption would be desirable. Although there have been many studies on the design optimization of IDEs and other pre-existing electrodes, such as the length, width, and spacing of the electrodes, to enhance the electrodes' dielectrophoretic performances (Albrecht *et al.* 2004; Liang *et al.* 2004; Jubery Dutta 2013; Sadeghian *et al.* 2017), optimization studies on the development of general planar electrode patterns to achieve these goals have received little attention. Yoon and Park (Yoon Park 2010) presented a topological optimization procedure using the finite element method, where the objective function was the spatial distribution of the square electric field for the entire domain. The developed electrode patterns were not experimentally demonstrated for practicability. Kinio and Mills

(Kinio Mills 2016) also presented a design procedure using simplified particle trajectories as the objective function for two flow velocity profiles. The developed design was also not verified experimentally, and a greater computation time was required compared to the approach with DEP force-based objective functions.

In this study, a simple and effective two-dimensional (2D) computational method was proposed to generate new planar electrode patterns to enhance the electric field intensity and dielectrophoretic particle capture. First, a novel objective function, which is factor **S**, was defined on the electrode surface, enabling the 2D computation of the volumetric DEP force generated by the planar electrodes. Conventional IDEs were then discretized into small rectangular cells, and for all possible connections of the discretized electrodes, **S** values were computed using the second-order central finite difference method without considering flow velocities with MATLAB R2018a, which will be referred to as the "microelectrode discretization (MED) method." The electrode pattern with the greatest value of **S** showed the MED-optimized electrode pattern in terms of volumetric downward DEP forces and was compared with the original IDEs. Here, **S** values were computed for all possible connections of the discretized electrodes generated from IDEs for comparison with the IDEs; however, this method can be applied to any planar discretized electrodes with modifications of boundary conditions.

Two MED-optimized electrodes were generated from two arrays of IDEs, where each consisted of six IDEs, and both the electrode width and gap were 20 μm in one case, and the electrode width was 20 μm and the gap was 10 μm in the other case. These two arrays of IDEs and respective MED-optimized electrodes were implemented in dielectrophoretic bacterial sorters separately, and DEP-assisted selective capture of bacteria *Escherichia coli* K-12 from 1-μm-diameter polystyrene beads were experimentally conducted and compared for the same electric (alternating current (AC) potentials, frequencies) and fluidic (flow rates) conditions.

1.2. Electrokinetic Manipulation of Biological Particles

Dielectrophoresis (DEP) refers to the movement of polarizable particles in a non-uniform electric field (Pohl 1951, Yang *et al.* 2000). This technique is an effective means of manipulating a specific type of biological particle, for example, particular species (Becker *et al.* 1995), size (Wang *et al.* 1998), or life state (Li Bashir 2002) in a heterogeneous particle mixture (Morgan *et al.* 1999). Coplanar electrodes such as interdigitated electrodes have been widely used to generate DEP due to their simple fabrication and ease of analysis. However, the DEP force over such electrodes generally decreases exponentially with the height above the electrode surface (Green *et al.* 2002); hence it is usually effective close to the electrode surface (Markx Pethig 1995; Gadish Voldman 2006). Furthermore, it is not easy to manipulate nanometer-sized biological particles, such as viruses and

proteins, rapidly by using DEP because the dielectrophoretic mobility decreases with the square of the particle diameter (Morgan *et al.* 1999).

On the contrary, alternating current (AC) electroosmosis (EO) is fluid motion induced by electrode polarization when AC electric potentials are applied to planar microelectrodes at intermediate characteristic frequencies (Ramos *et al.* 1999). This technique has been applied in several fluidic applications, such as micropumps with arrays of asymmetric electrodes (Brown et al. 2000; Studer et al. 2004; Huang et al. 2010) and micromixers for chemical species and electrolytes (Sasaki *et al.* 2006; Chen *et al.* 2009; Chen *et al.* 2013) with low applied electric potentials. As AC EO is exerted on fluids rather than particles, the use of AC EO alone may be limited in several applications such as sorting, separation, selective concentration, and focusing based on their electrical properties.

In this regard, DEP and EO need to be combined to enable the selective and rapid concentration of particles far from the electrodes as well as near the electrodes onto a particular spot, such as a sensing element, thereby increasing the sensitivity of a sensor to biological particles such as bacteria, proteins, and viruses (Gong 2010; Sharma *et al.* 2016). Few studies have been conducted using both EO and DEP on planar electrodes; in those studies, two electrodes generating DEP were implemented in the gaps between two outer electrodes inducing EO (Heeren *et al.* 2007; Cheng *et al.* 2013). Therefore, the shapes and sizes of the planar electrodes were limited, and more care needs to be taken to avoid electrical shorts between the electrodes.

Other studies in which a pair of sinusoidal signals between two planar electrodes were used have also been reported on; in those cases, both DEP and EO needed to occur at the same AC frequency (Gong 2010; Gagnon Chang 2005; Zhou *et al.* 2005; Lin *et al.* 2016; Rezanoor Dutta 2016) or to be generated in alternating time intervals (Melvin *et al.* 2011) (Table 1-1). However, AC EO generally occurs when the frequency is less than a few kHz (Green *et al.* 2000) while DEP capture usually works effectively in higher frequencies, for example, kHz or MHz regions (Park 2009; Sang 2016) therefore, applying a pair of sinusoidal signals to generate both DEP and EO may not work in many cases. Moreover, there are risks in this case that electrode damage or air bubble generation may occur by electrolysis at low frequencies (Castellanos *et al.* 2003), when the electrical potential needs to be increased for better particle manipulation.

Here, a simple and effective method was proposed of concentrating bacteria, viruses, and proteins rapidly and selectively on two coplanar electrodes via superimposing AC DEP and EO signals for biosensor applications. Signal superposition techniques have been previously employed in several studies using two sets of sinusoidal waves (Pethig *et al.* 2003; Valero *et al.* 2010; Han *et al.* 2013), and pulsed sinusoidal waves (Cui *et al.* 2009; Kumemura *et al.* 2011; Honegger Peyrade 2013); however, they involved only electrical forces exerted on the particles suspended in fluids such as DEP, traveling wave DEP, and electrorotation for sorting, separation, trapping etc., and hence many of the particles located far from the electrode could not be manipulated rapidly. In the present study, EO was combined

with DEP to enhance particle capture selectively and rapidly, which is critical for biosensors requiring rapid detection of biological particles. Although EO and DEP have been extensively studied (Table 1-1), this topic has not attracted much attention (Han *et al.* 2017).

Firstly, the frequencies for optimal EO and DEP generation were determined, and the two waveforms were superimposed and applied to the fabricated coplanar electrodes (Fig. 3-1). Selective concentration of *Escherichia coli* K-12 was conducted against 1-μm-diameter polystyrene (PS) beads from a bacteria–bead mixture. MS2 viruses and fluorescein isothiocyanate (FITC)-labelled troponin I antibody (cTnI-Ab) were also tested to determine whether this method would work for nanometer-sized particles. The particles concentrated within targeted areas on the electrodes were quantified with different treatments: no solution (negative control), no signal (positive control), lower frequency signals (EO), higher frequency signals (DEP), and superimposed signals (EO+DEP), and the effects of these treatments were analyzed.

Table 1-1. Electrokinetic studies involving simultaneous treatment of DEP and EO, and signal superposition. PS: polystyrene; EO: electroosmosis; DEP: dielectrophoresis; IDEs: Interdigitated electrodes; EP: electrophoresis; AHA: azidohomoalanine; ITO: indium tin oxide; CTB: cholera toxin subunit B; twDEP: traveling-wave DEP; PBS: phosphate buffered saline; DI: deionized.

	Method	Particle	Medium	AC Excitation & Exposure Time	Electrode Type (Width/Gap)	Electrode Material	Reference
DEP+EO	Narrow DEP electrodes inside wide EO electrodes	1-μm-diam. PS beads	DI water	DEP: 1 Vpp, 1731 Hz, EO: 1 Vpp, 1000 Hz, 60 s	IDEs (EO: 30 μm/25 μm; DEP: 1 μm/1 μm)	Ti/Au	Heeren *et al.* 2007
	Circular DEP-EP electrodes inside wider ring-shaped EO electrodes	*Staphylococcus aureus*	300 mM sucrose solution	DEP-EP: 0.5 V DC bias, EO: 8-12 Vpp, 800 Hz, 3 min	Planar rings	Au	Cheng *et al.* 2013
	Two sinusoidal signals (0° & 180°)	*Escherichia coli*	1.5M AHA (relative permittivity : ~200)	20 Vrms, 400 kHz, 12 s	IDEs (35 μm/35 μm)	Ti/Pt	Gagnon Chang 2005
	Two sinusoidal signals (0° & 180°)	*Saccharomyces cerevisiae*	0.1 mM NaHCO3 (9.15 μS/cm)	6.74 Vrms, 1 kHz, 10 min	Top–bottom	ITO	Zhou *et al.* 2005
	Two sinusoidal signals (0° & 180°)	CTB	10 μM phosphate buffer	1 Vpp, 47 Hz, 20 min	Coplanar (7 μm gap)	Ti/Au/Ti	Gong 2017
	Four sinusoidal signals (0°, 90°, 180° & 270°) for travelling-wave	HL-60 cells	100 μM KCl + 5% glucose (18 μS/cm)	3 kHz, 12 min	Circular sectors	Ti	Lin *et al.* 2016
	Two sinusoidal signals (0° & 180°)	25-μm-diam. barium titanate particles	2-propanol (0.011 μS/cm)	15 Vpp, 60 Hz, 8 s	IDEs (60 μm/40 μm)	Ti	Rezanoor Dutta 2016
	Alternately applied DEP and EO signals (DEP->EO-	1-μm-diam. latex particles	DI water (0.25 μS/cm)	DEP: 1.6 Vpp, 5 kHz, EO: 1.6 Vpp, 300 Hz, 5 min	Square spiral (5–30 μm/5 μm)	Cr/Au	Melvin *et al.* 2005

	>DEP->EO->…)						
Signal Superposition for DEP	DEP+twDEP (sine+sine superposition)	T lymphocyte	Sucrose solution (400 μS/cm)	DEP: 5.2 Vpp, 30 kHz, twDEP: 5.6 Vpp, 350 kHz, unknown time	IDEs (10 μm/10 μm)	-	Pethig *et al.* 2003
	DEP+DEP (sine+sine superposition)	Viable/non-viable yeast cells	Diluted PBS (600 μS/cm)	DEP (focusing): 3.39 Vrms, 60&90 kHz, DEP (sorting): 4.38 Vrms, 5 MHz, 20 s	Liquid electrodes chambers (20 μm/20 μm)	Ti/Pt	Valero *et al.* 2010
	DEP + electrorotaion (sine+sine superposition)	T lymphocyte	Inositol-added medium (326 μS/cm)	DEP (trap): 2 Vpp, 20 kHz, electrorotation: 0.4 Vpp, 100 kHz, 30 s	3D octode (top–bottom quadrupoles; 50 μm gap)	Cr/Au	Han *et al.* 2013
	Pulsed DEP (sine+on-off cycles)	3-μm-diam. PS beads	DI water	Sine: 20 Vpp, 10 MHz, on-off: 0.3 Hz, 10 s	IDEs (30 μm/30 μm)	ITO	Cui *et al.* 2009
	Pulsed DEP (sine+on-off cycles)	Single lambda-DNA	DI water (1.1 μS/cm)	Sine: 20 Vpp, 1 MHz, on-off: 20 Hz, 1-10 s	Coplanar (10 μm gap)	Silicon nanotweezers	Kumemura *et al.* 2011
	Pulsed DEP (sine+square superposition)	10-μm-diam. PS beads	DI water (2 μS/cm)	Sine: 10 Vpp, 50 kHz, square: 10 Vpp, 2 MHz, 1 s	Top–bottom	ITO	Honegger Peyrade 2011
DEP+EO via Signal Superposition	DEP+EO (sine+sine superposition)	*E. coli* K-12/1-μm-diam. PS beads	0.01× PBS (184 μS/cm)	DEP (selective concentration): 5 Vpp, 2 MHz, EO (convection): 1.2 Vpp, 1633 Hz, 30 s	Coplanar (25 μm gap)	ITO	Han *et al.* 2018
		MS2 virus	Diluted in DI water (4 μS/cm)	DEP (concentration) : 10 Vpp, 100 kHz, EO (convection) : 2 Vpp, 1000 Hz, 1 min			
		Troponin I antibody	Diluted in DI water (16 μS/cm)	DEP (concentration) : 10 Vpp, 10 kHz, EO (convection) : 2 Vpp, 500 Hz, 1 min			

1.3. Biosensors Assisted by Electrokinetics

Rapid measurement of pathogenic bacteria is a critical process in medical diagnostics, food industry, and environmental monitoring, among others. Extensively used techniques for such purposes include growth and colony counting, nucleic-acids-based assays, and immunoassays (Kim *et al.* 2015). Electrokinetic technologies such as AC electro-osmosis (EO) and dielectrophoresis (DEP) have been employed for effective manipulation of bacteria, such as separation, enrichment, and mixing, as preliminary steps before detection to enhance the sensitivity of the assay (Salari Thompson 2018; Han

et al. 2018). AC EO represents a fluid motion induced by electrode polarization; therefore, microorganisms that are distant from the electrode can be moved closer to a detection area with flow motion, and this process is not dependent on particle size and type (Gong 2010). On the other hand, AC DEP involves the movement of a polarizable particle in a non-uniform electric field depending on the particle size and the electrical properties of particles and media, thereby enabling concentration of particular microorganisms in a detection area (Kim *et al.* 2015; Freedman *et al.* 2015; Sharma *et al.* 2016; Galvan *et al.* 2018). The positive DEP (pDEP) is extensively used to capture bacterial particles, although it is effective only in regions close to an electrode. Recently, the simultaneous use of AC EO and DEP at a single electrical frequency was reported (Leahy Lai 2017ab); however, the choice of frequency was even more limited than using either AC EO or DEP alone. AC electrothermal (ET) actuation was also applied to induce convective flows in sensors (Lee *et al.* 2016), while additional considerations, such as conformational changes, thermal stress of pathogens, and damages to devices via temperature rise owing to Joule heating, are unavoidable (Salari Thompson 2018; Galvan *et al.* 2018).

Many of previously reported electrokinetics-enhanced biosensors are based on stagnant liquids (Salari Thompson 2018), where analytes can be manipulated more easily than under flowing liquids. If a biosensor is implemented within a pressure-driven flow rather than a stagnant liquid for higher throughput, automation, multiplexed detection, and/or continuous monitoring (Syedmoradi *et al.* 2019), stronger electrical forces need to be exerted on the analytes, such as pDEP, to overcome the hydrodynamic forces and to bind the particles to a detection zone, which usually constitutes a very small area for field-effect transistor (FET)-based sensors (Lee *et al.* 2009). This can be a challenge because an effective region for the pDEP is usually too close to the electrode of the channel surface to drag all the particles flowing from the top surface to the bottom toward the detection zone of a biosensor against the flow direction, especially when the particles flow with high speed and the detection zone is small. Hence, in most studies on electrokinetics-enhanced biosensors for flowing targets, capture efficiencies were either low or not measured, labeling was used, the limits of detection were relatively high, the electrical impedance technique was used for detection by using relatively large electrode areas, and/or sensor selectivity against non-targets was not tested (Table 1), although electrokinetic particle manipulation has been extensively explored for last several decades.

One approach to address this challenge is to align all the particles along two-dimensional surfaces or one-dimensional lines during flow, which is commonly called “particle focusing.” Several particle focusing techniques have been developed in literature. Inertial focusing is a passive technique that is generated by particle inertia under a flow field (Park *et al.* 2009; Cruz *et al.* 2019); however, complicated device structures are needed, and small particles are unlikely to be manipulated by this technique (Ren *et al.* 2016). Acoustic focusing involves surface acoustic waves, showing fast fluidic actuation and contact-free particle manipulations (Ai *et al.* 2013; Ding *et al.* 2013). DEP focusing

incorporates an array of planar or vertical electrodes for applying the DEP forces; however, particle losses are unavoidable because many particles attach to the focusing electrodes in case of the pDEP (Kim *et al.* 2015; Liu *et al.* 2018), and the DEP force is inherently insufficient in regions farther from the electrodes (Gadish Voldman 2006). These three focusing techniques are also strongly dependent on particle sizes; hence, small particles in the range of submicron sizes are difficult to focus (Ding *et al.* 2013; Cruz *et al.* 2019). More importantly, none of these focusing technologies can align all the particles close to the detection area without losses to the channel surfaces, which is critical for development of a biosensor involving pDEP to capture flowing particles.

Herein, a microfluidic FET immunosensor was presented equipped with electrohydrodynamic (EHD) focusing and DEP concentration for continuous and label-free electrical detection of *Staphylococcus aureus* in a 0.01× phosphate buffered saline (PBS) solution. Many flow-type DEP-mediated biosensors have involved impedance measurements with electron transfer through the media (Yang Bashir 2008; Paez-Aviles *et al.* 2016) or pearl chain conductance of bacteria between the electrodes (Suehiro *et al.* 2003) (Table 1). It has been suggested that FET-based sensors adopting silicon nanowires and CNTs are integrated with a microfluidic platform in order to enhance sensitivity and to achieve automated and multiplexed analytical systems (Syedmoradi *et al.* 2019); however, no studies in which particle focusing was implemented with FET-based biosensors under a pressure-driven flow have been reported on.

EHD focusing uses a combination of AC EO and negative DEP (nDEP) rather than pDEP to align flowing particles along one-dimensional lines close to the bottom surface, and Ren *et al.* (2016) demonstrated EHD focusing for the first time using two electrical-bias-free electrodes at a fixed AC frequency (200 Hz) for 4-μm-diameter silica beads. The operation condition in their study was very limited; both AC EO and nDEP were required to occur at the same frequency. In the present study, superimposed signals having two AC frequency components, lower (AC EO with weak pDEP) and higher (dominant nDEP), were implemented without electrical-bias-free electrodes to align incoming 380-nm-diameter polystyrene beads and label-free *Staphylococcus aureus* along one-dimensional lines close to the bottom surface to facilitate pDEP capture downstream. Polystyrene beads were used to demonstrate the enhanced electrokinetic characteristics of the present microfluidic device, as they are widely used in quantitative evaluation of DEP systems with their regular spherical shapes and homogeneities compared to actual biological particles (Chen *et al.* 2019).

The bacteria aligned using EHD focusing were further concentrated downstream using pDEP forces and quantified with a carbon-nanotubes-based FET immunosensor (Fig. 4-3a). This FET sensor consists of two embedded concentration electrodes, two detection (source and drain) electrodes connected to an array of antibody-functionalized and aligned single-walled carbon nanotubes (SWCNTs), and a dielectric layer (Si3N4) to separate these two pairs of electrodes vertically (Sharma *et al.* 2016). The relative electrical conductance change (RCC) between the detection electrodes

owing to the bacteria concentrated on the SWCNTs was continuously measured. A 0.01× PBS solution was used as the medium, with electrical properties similar to drinking or tap water. The selectivity of the sensor platform was tested against *Bacillus subtilis*, *Escherichia coli* C3000, and *Staphylococcus epidermidis* along with its sensitivity. The selectivity was also investigated by DEP-capturing *S. aureus* (target) and *E. coli* C3000 (non-target) on the *S. aureus* antibody-coated SWCNTs under flows without EHD focusing and then by flushing, which has not been clearly reported until now.

Chapter 2. Development of Microelectrode Discretization (MED) Method to Maximize the DEP capture

(Note: This chapter is partially or totally adapted from the published journal paper of myself, Han *et al.* 2019.)

2.1 Theory

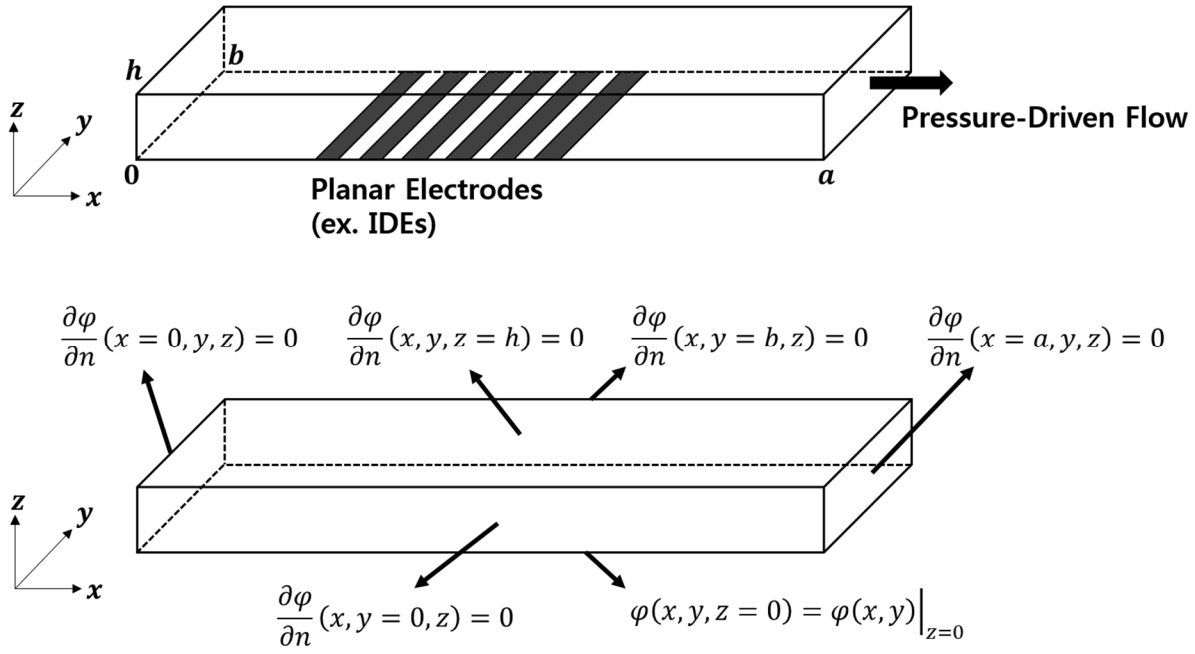

Figure 2-1. Schematic diagram of a microfluidic device having planar electrodes, such as interdigitated electrodes (IDEs), with electrical boundary conditions.

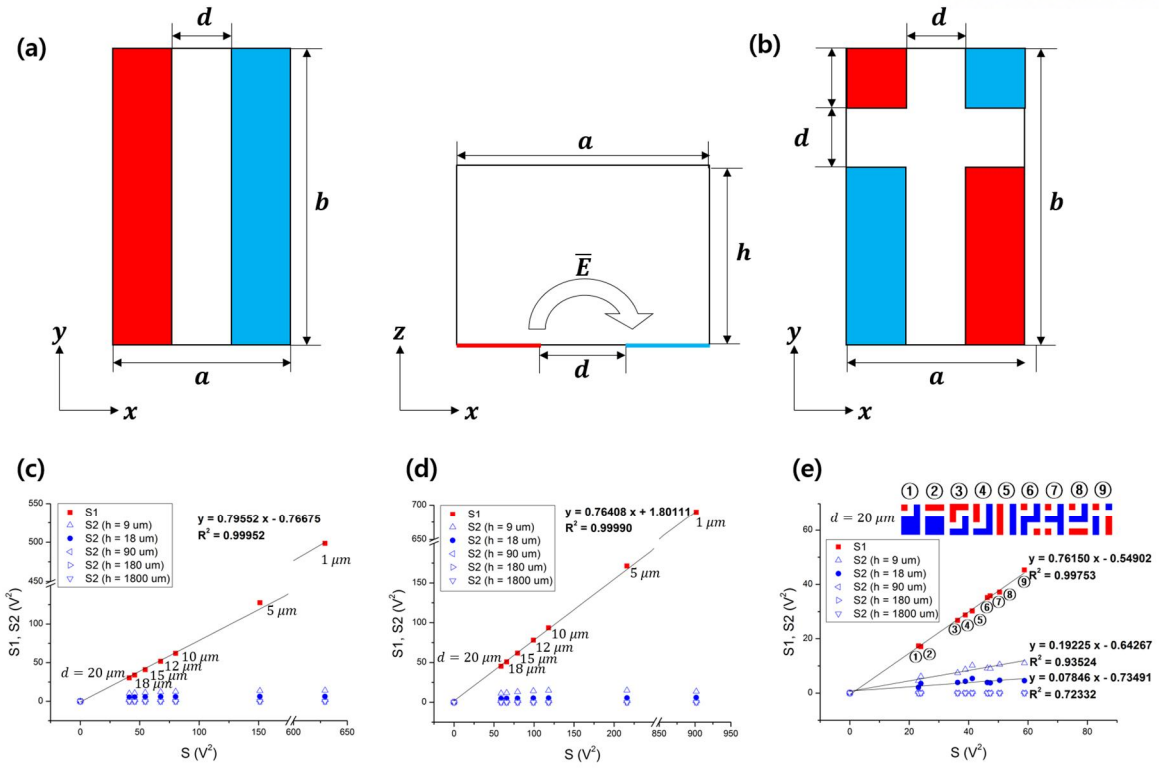

Figure 2-2. (a) Electrode pattern (Example 1) having two line-shaped electrodes and its electric field formation. (b) Electrode pattern (Example 2) having quadrant planar electrodes. (c) Plots of $\mathbf{S_1}$ and $\mathbf{S_2}$ with respect to $\mathbf{S}$ ($\mathbf{V_0}$ is 1 V) of Example 1 and (d) Example 2 for different values of d and h. (e) Plots of $\mathbf{S_1}$ and $\mathbf{S_2}$ with respect to $\mathbf{S}$ for the nine different patterns (including the patterns of example 1 and 2; $\boldsymbol{d}$ is 20 μm) for different values of h.

A polarizable particle suspended in a liquid under both a non-uniform AC electric field and flow field experiences drag force, gravity, buoyancy, DEP force, etc. The time-averaged DEP force exerted on the particle in the medium can be expressed as (Pohl 1951; Huang *et al.* 2001)

$$\overline{F}_{DEP} = 2\pi\varepsilon_m {r_p}^3 Re[f_{CM}(\omega)]\underline{\nabla}\left|\overline{E}_{rms}\right|^2, \quad (1)$$

where ε_m is the electrical permittivity of the medium; r_p is the radius of the particle; $f_{CM}(\omega) = \frac{{\varepsilon_p}^* - {\varepsilon_m}^*}{{\varepsilon_p}^* + 2{\varepsilon_m}^*}$ is the Clausius–Mossotti (CM) factor for the particle and the media, where ${\varepsilon_p}^*$ and ${\varepsilon_m}^*$ are complex permittivities of the particle and the media, respectively; $Re[f_{CM}(\omega)]$ is the real part of the CM factor; ω is the angular frequency (rad/s) of the applied AC signals; and $\overline{E}_{rms}$ is the root-mean-squared electric field intensity. For bacteria, more accurate dielectric modeling is needed for the calculation of the CM factor as their cytoplasm is surrounded by a membrane and wall (Asami *et al.* 1980; Park *et al.* 2011).

IDEs are usually located on the bottom surface ($z = 0$) of a microfluidic channel with a rectangular cross-section (Fig. 2-1). Assuming a homogeneous electrolyte concentration (Green *et al.*

2001; Ren *et al.* 2015), the governing equation for the electric potential is reduced to the Laplace equation, $\nabla^2\varphi = 0$, where φ is the electric potential. A far-field Neumann condition of $\frac{\partial\varphi}{\partial n} = 0$ is applied at the inlet and outlet planes, $x = 0$ and $x = a$ (Oh et al. 2009). The normal currents are continuous at the three electrolyte-wall interfacial planes: $y = 0$, $y = b$, and $z = h$ (Green *et al.* 2001), that is,

$$\left[(\sigma + i\omega\varepsilon)\frac{\partial\varphi}{\partial n}\right]_{electrolyte} = \left[(\sigma + i\omega\varepsilon)\frac{\partial\varphi}{\partial n}\right]_{wall}, \quad (2)$$

where σ is electrical conductivity and ε is electrical permittivity, leading to the Neumann conditions of $\frac{\partial\varphi}{\partial n} = 0$ on the three interfacial planes. The bottom surface of the channel is subjected to an applied electric field, which is given by $\varphi(x, y, z = 0) = \varphi(x, y)|_{z=0}$. The solution set can be obtained by using the method of separation of variables with the five Neumann boundary conditions and can be given by

$$\varphi(x, y, z) = \sum_{m=0}^{\infty}\sum_{n=0}^{\infty} G_{m,n}\cos\frac{m\pi x}{a}\cos\frac{n\pi y}{b}\cosh\gamma_{m,n}(z - h), \quad (3)$$

where

$$\gamma_{m,n} = \sqrt{\left(\frac{m\pi}{a}\right)^2 + \left(\frac{n\pi}{b}\right)^2}, \quad (4)$$

and the coefficient $G_{m,n}$ can be determined by the electric field condition applied on the bottom surface.

The negative z-directional component of the DEP force is directly related with the dielectrophoretic capture onto the electrodes, and the partial derivative of the squared magnitude of electric field intensity in the z direction is given by

$$\frac{\partial|\overline{E}|^2}{\partial z} = \frac{\partial}{\partial z}\left({E_x}^2 + {E_y}^2 + {E_z}^2\right) = 2E_xE_{x,z} + 2E_yE_{y,z} + 2E_zE_{z,z}, \quad (5)$$

where the electric field intensity is defined as

$$\overline{E} = -\underline{\nabla}\varphi = -\frac{\partial\varphi}{\partial x}\hat{\imath} - \frac{\partial\varphi}{\partial y}\hat{\jmath} - \frac{\partial\varphi}{\partial z}\hat{k} = E_x\hat{\imath} + E_y\hat{\jmath} + E_z\hat{k}. \quad (6)$$

From Eqs. 3, 5, and 6,

$$\frac{\partial|\overline{E}|^2}{\partial z}(x, y, z) = \sum_{m=0}^{\infty}\sum_{n=0}^{\infty}\sum_{m\prime=0}^{\infty}\sum_{n\prime=0}^{\infty} H_{m,n,m\prime,n\prime}(x, y)\cosh\gamma_{m,n}(z - h)\sinh\gamma_{m\prime,n\prime}(z - h), \quad (7)$$

where

$$H_{m,n,m\prime,n\prime}(x, y) = 2\gamma_{m\prime,n\prime}G_{m,n}G_{m\prime,n\prime}\left(\frac{mm\prime\pi^2}{a^2}\sin\frac{m\pi x}{a}\cos\frac{n\pi y}{b}\sin\frac{m\prime\pi x}{a}\cos\frac{n\prime\pi y}{b} + \right.$$

$$\left.\frac{nn\prime\pi^2}{b^2}\cos\frac{m\pi x}{a}\sin\frac{n\pi y}{b}\cos\frac{m\prime\pi x}{a}\sin\frac{n\prime\pi y}{b} + {\gamma_{m,n}}^2\cos\frac{m\pi x}{a}\cos\frac{n\pi y}{b}\cos\frac{m\prime\pi x}{a}\cos\frac{n\prime\pi y}{b}\right). \quad (8)$$

According to Eq. 7, the magnitude of the z-direction component of the DEP force decreases exponentially with z, and is equal to zero on the top wall ($z = h$), when the planar electrodes are implemented within the microchannel.

The integration of Eq. (7) throughout the volumetric domain of the microchannels, $\int_0^a\int_0^b\left(\int_0^h\frac{\partial|\overline{E}|^2}{\partial z}dz\right)dydx$, can offer a simple measure of DEP particle capture onto the

electrodes; hence comparisons of the potential planar electrode patterns for a given flow field, particle, and medium can be conducted. The integration can be decomposed into

$$\int_0^h \frac{\partial |\overline{E}|^2}{\partial z} dz = \left[{E_x}^2 + {E_y}^2 + {E_z}^2 \right]_0^h = -S - S_1 + S_2 + S_3 = -(S + S_1 - S_2), \quad (9)$$

where

$$S(x,y) = \left({E_x}^2 + {E_y}^2 \right)\Big|_{z=0}, \quad (10)$$

$$S_1(x,y) = {E_z}^2\Big|_{z=0}, \quad (11)$$

$$S_2(x,y) = \left({E_x}^2 + {E_y}^2 \right)\Big|_{z=h}, \quad (12)$$

$$S_3 = {E_z}^2\Big|_{z=h} = 0. \quad (13)$$

The integral sums of these three factors over the surface can be given by

$$\mathbf{S} = \int_0^a \int_0^b S \, dydx \ (\mathrm{V}^2), \quad (14)$$

$$\mathbf{S_1} = \int_0^a \int_0^b S_1 \, dydx \ (\mathrm{V}^2), \text{ and} \quad (15)$$

$$\mathbf{S_2} = \int_0^a \int_0^b S_2 \, dydx \ (\mathrm{V}^2). \quad (16)$$

The function $\int_0^a \int_0^b \left(\int_0^h \frac{\partial |\overline{E}|^2}{\partial z} dz \right) dydx$ is simplified into $-(S + S_1 - S_2)$, and maximizing **S** and $\mathbf{S_1}$, and minimizing $\mathbf{S_2}$ would maximize the volumetric downward DEP force through the channel.

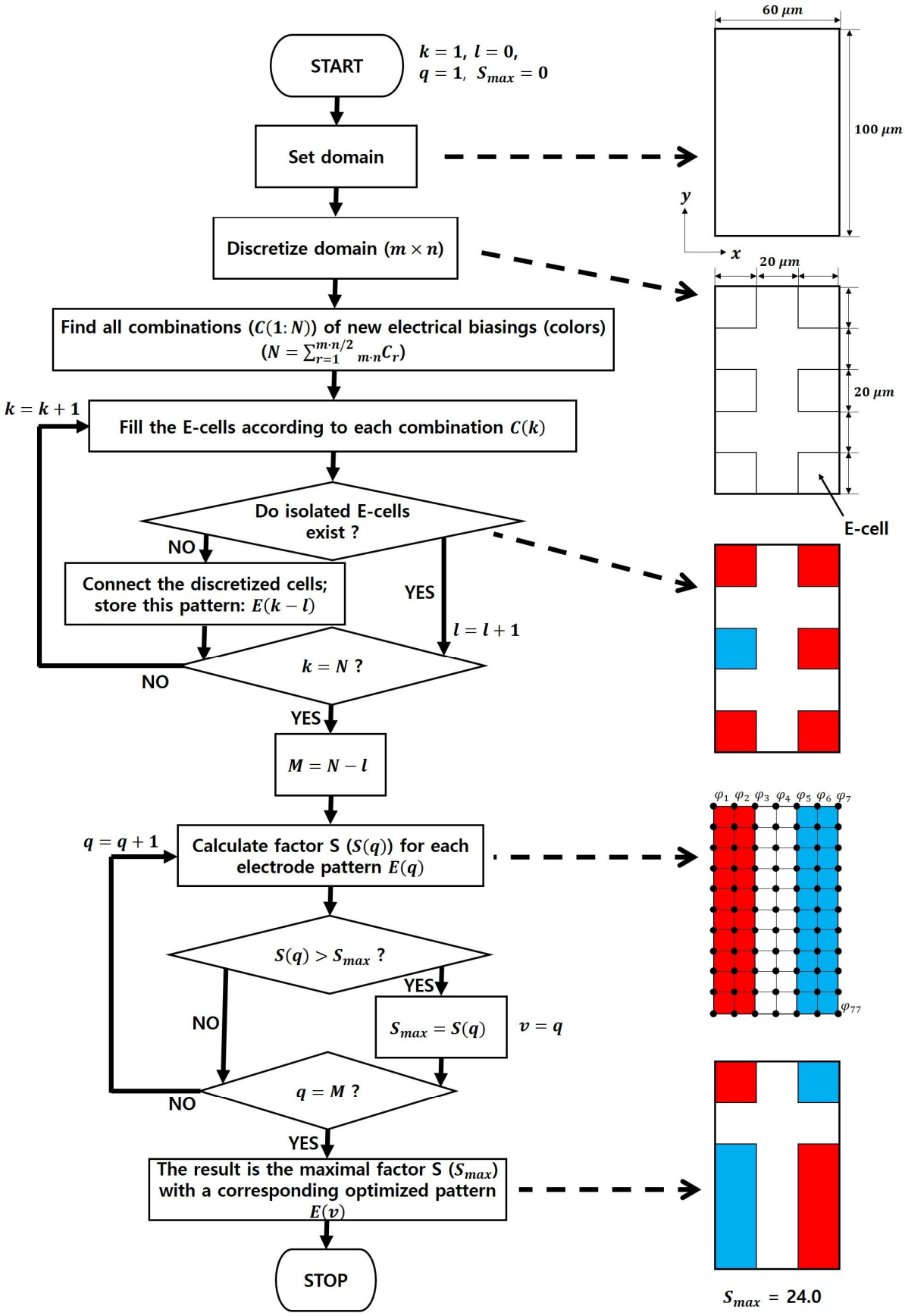

Figure 2-3. Flowchart of the MED process.

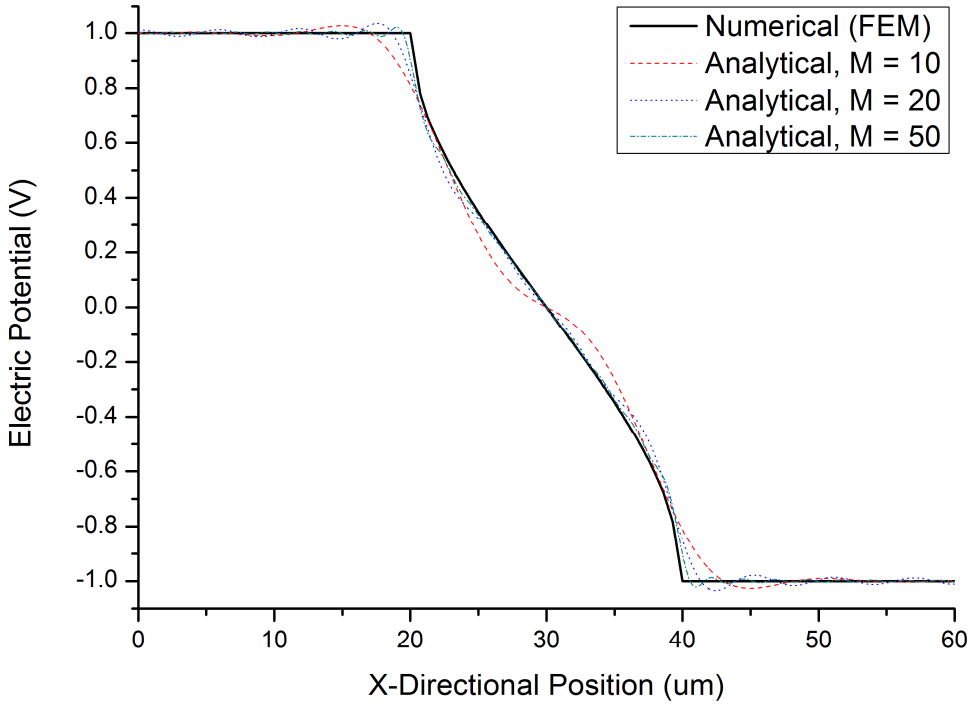

Figure 2-4. Numerically and analytically calculated electric potential distributions of Fig. 2-2a at $\boldsymbol{z = 0}$ ($\boldsymbol{V_0}$ = 1 V, $\boldsymbol{d}$ = 20 μm), where the analytic electric potential was $\boldsymbol{\varphi(x, z = 0)} = \sum_{m=0}^{\infty} \boldsymbol{G_m} \cos\frac{m\pi x}{a} \cosh\left(-\frac{m\pi}{a}h\right)$ under the truncated number of $\boldsymbol{m}$ from 0 to $\boldsymbol{M}$.

Table 2-1. Calculated $\boldsymbol{G_m}$ with $\boldsymbol{m}$ for Fig. 2-2a and Fig. 2-4 ($\boldsymbol{V_0}$ = 1 V, $\boldsymbol{d}$ = 20 μm).

$\boldsymbol{m}$	$\boldsymbol{G_m}$	**12**	-1.02E-21	**25**	1.44E-12	**38**	5.82E-30
0	5.92E-17	**13**	2.85E-07	**26**	-6.35E-27	**39**	-7.48E-19
1	0.801729	**14**	2.30E-21	**27**	-1.04E-13	**40**	1.22E-30
2	-6.37E-18	**15**	-2.14E-08	**28**	-8.94E-28	**41**	-1.17E-19
3	-0.02298	**16**	-8.75E-23	**29**	-1.32E-14	**42**	-3.84E-32
4	2.52E-17	**17**	-1.88E-09	**30**	2.38E-28	**43**	3.25E-20
5	-0.00055	**18**	-5.78E-24	**31**	3.81E-15	**44**	5.51E-33
6	-3.31E-18	**19**	5.92E-10	**32**	1.26E-28	**45**	-2.25E-21

7	0.000196	**20**	2.32E-24	**33**	-2.69E-16	**46**	3.26E-33
8	5.70E-19	**21**	-4.39E-11	**34**	1.12E-28	**47**	-3.89E-22
9	-1.38E-05	**22**	8.33E-25	**35**	-3.83E-17	**48**	7.37E-34
10	-1.08E-20	**23**	-4.78E-12	**36**	9.01E-29	**49**	1.16E-22
11	-8.58E-07	**24**	3.83E-27	**37**	1.08E-17	**50**	2.59E-35

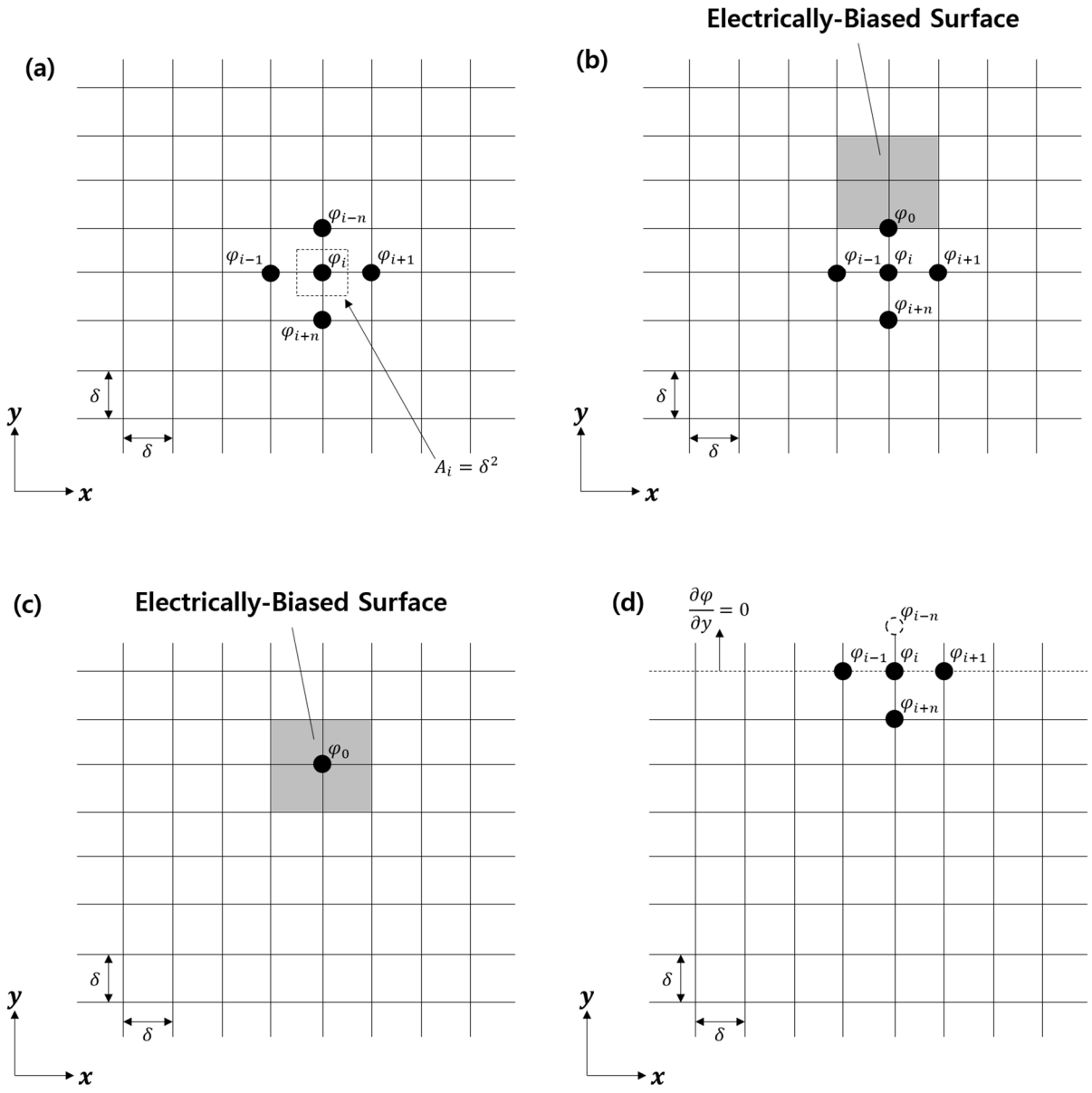

Figure 2-5. Finite difference equations for electric potential on a planar electrode can be derived for several representative cases: **(a)** The electric potential $\boldsymbol{\varphi_i}$ is equal to the average of the electric potentials of the four neighboring points, **(b)** One of the neighboring points is on the boundary of the

electrically-biased surface, **(c)** The electric potential $\boldsymbol{\varphi_i}$ is inside the electrically-biased surface, and **(d)** Some of the neighboring points are on the electrically insulated boundaries.

These three factors were investigated in several examples. The first example involved two line-shaped coplanar electrodes separated by a gap of d, and the electric potentials V_0 and $-V_0$ indicated by red and blue colors, respectively, were applied to the electrodes (Fig. 2-2a). Owing to the symmetry of the electrodes, $E_y = 0$. The electric potential distribution was solved analytically by modifying the previously reported mathematical derivation for the mixed (Dirichlet and Neumann) boundary conditions (Song Bennett 2008), with the convergence of the series solution confirmed (Fig. 2-4, Table 2-1). The second example involved planar quadrant electrodes (Fig. 2-2b). In these two examples, numerical solutions were used to calculate **S,** $\mathbf{S_1}$, and $\mathbf{S_2}$ with several electrode gaps (Fig. 2-2c and 2-2d). At small values of the gap (d) compared to the channel height (h), **S** and $\mathbf{S_1}$ were much larger than $\mathbf{S_2}$, and as the ratio (d/h) increased, **S** and $\mathbf{S_1}$ became closer to $\mathbf{S_2}$ (Figs. 2-2c and 2-2d); however, the gap is usually made small compared to the channel height for high DEP forces. It was observed that $\mathbf{S_1}$ was positive and linearly proportional to **S**, and $\mathbf{S_2}$ was small compared to $\mathbf{S_1}$. These factors were further numerically investigated using COMSOL for nine different electrode patterns, fixing the gap d to 20 μm (Fig. 2-2e). These nine patterns can show possible electric fields around the electrode edges generated by many different electrode shapes. The factors $\mathbf{S_1}$ and $\mathbf{S_2}$ were also linearly proportional to **S**, and $\mathbf{S_2}$ was comparatively small.

The observations from the examples show that maximizing the value of **S** will lead to the electrode pattern that can generate the largest downward DEP force along the volumetric domain according to Eq. (9); hence, relative comparisons between potential electrode patterns for given particles, media, and flow fields can be performed. This method requires only the 2D computation of electric fields on the electrode surface, which would be simpler and faster than the 3D computation through the volumetric domain.

The second-order central difference scheme was then used to determine the electric fields on the bottom surfaces. Laplace equation for the electrical potential on a 2D plane can be shown as

$$\frac{\partial^2 \varphi}{\partial x^2} + \frac{\partial^2 \varphi}{\partial y^2} = 0. \tag{17}$$

According to the second-order central difference scheme, the second order partial derivatives can be approximated as (Fig. 2-5a)

$$\left.\frac{\partial^2 \varphi}{\partial x^2}\right|_i = \frac{\varphi_{i-1} + \varphi_{i+1} - 2\varphi_i}{\delta^2}, \text{ and} \tag{18}$$

$$\left.\frac{\partial^2 \varphi}{\partial y^2}\right|_i = \frac{\varphi_{i-n} + \varphi_{i+n} - 2\varphi_i}{\delta^2}, \tag{19}$$

where i is a grid index, φ_i is the electric potential at grid i, δ is the distance between the neighboring grids, and n is the number of grid columns. The resulting Laplace equation can be given by

$$\varphi_{i-n} + \varphi_{i-1} - 4\varphi_i + \varphi_{i+1} + \varphi_{i+n} = 0. \quad (20)$$

If one of the neighboring grids has a fixed electric potential as shown in Fig. 2-5b, where $\varphi_{i-n} = \varphi_0$ is a fixed electric potential, Eq. 21 is shown as

$$\varphi_{i-1} - 4\varphi_i + \varphi_{i+1} + \varphi_{i+n} = -\varphi_0. \quad (21)$$

If grid *i* and the neighboring grids are biased to the same fixed electric potential, the electric potential at the grid i is simply $\varphi_i = \varphi_0$ (Fig. 2-5c). When the grid i is on an electrically insulated surface, $\varphi_{i-n} = \varphi_{i+n}$ (Fig. 2-5d) and Eq. 22 is given by

$$\varphi_{i-1} - 4\varphi_i + \varphi_{i+1} + 2\varphi_{i+n} = 0. \quad (22)$$

Finite difference equations for electric potentials at all grid points can be obtained in the same manner and solved using MATLAB.

The distributions of electric potential on the bottom surfaces, φ_i, were obtained with various boundary conditions (Fig. 2-5), where i is the grid index. The factor $S_i(x, y)$ can be expressed as

$$S_i(x, y) = {E_{x,i}}^2 + {E_{y,i}}^2 \ (\mathrm{V^2/m^2}), \quad (23)$$

where

$${E_{x,i}}^2 = \left(-\frac{\varphi_{i+1} - \varphi_{i-1}}{2\delta}\right)^2, \text{ and} \quad (24)$$

$${E_{y,i}}^2 = \left(-\frac{\varphi_{i+n} - \varphi_{i-n}}{2\delta}\right)^2, \quad (25)$$

where the grid i is surrounded by four neighboring grids, top $(i - n)$, left $(i - 1)$, right $(i + 1)$, and bottom $(i + n)$; n is the number of grid columns; and δ is the distance between the neighboring grids. (Fig. 2-5). The factor **S** for the entire bottom surface is expressed as

$$\mathbf{S} = \sum_i S_i A_i = \delta^2 \sum_i S_i \ (\mathrm{V^2}), \quad (26)$$

where A_i is an area of the cell occupied by the grid i. The electrode pattern showing the greatest value of **S** can be considered the MED-optimized electrode.

Figure 2-3 shows the algorithm of the MED method and its application to the two simple IDEs (Fig. 2-2a). IDEs are commonly used in many microfluidic systems and were compared with the MED-optimized electrode pattern, with keeping the working volumes, where electric fields are biased on the bottom surfaces, identical for both the electrode patterns. After the domain is set, it is first discretized into equally sized electrode cells (E-cells) and gaps, and each E-cell is filled with either a red (+1 V) or blue (−1 V) color. Consequently, many different electrode patterns can be generated by connecting adjacent E-cells having the same colors horizontally and vertically, and excluding the patterns with isolated E-cells from the external contact pads. To identify isolated E-cells, a point is located at an E-cell and is moved to an adjacent cell having the same color as the original E-cell. The point is then moved to another adjacent same-colored E-cell without coming back to the previous E-cell. If the point

cannot reach the outer surface by repeating this procedure, the original E-cell is determined to be isolated. The factor **S** is then calculated for each of the new patterns. Figure 2-2e shows all the possible electrode patterns using the MED method for these two IDEs. Pattern 9 showed the largest value of **S**, which increased to 24.0 V^2 from 16.5 V^2 (Fig. 2-3). In other words, the new electrode pattern shows enhanced downward DEP forces under the same applied electric potentials compared with the original IDEs.

2.2. Materials and Methods

2.2.1 Materials

The following materials were purchased from commercial sources: a negative tone photoresist (SU-8 2015) and its developer (SU-8 developer) from MicroChem Corp. (USA); polydimethylsiloxane (PDMS; Sylgard® 184) from Dow Corning Corp. (USA); Tygon® microbore tubing (T23-181-471; inner diam.: 0.01 in.) from Saint-Gobain (France); a syringe (10 ml) and its needle (26G; 0.5 in. length) from Korea vaccine (Kovax; Korea); trichloro(1H,1H,2H,2H-perfluoro-octyl)silane (97% purity; 448931) and 4',6-diamidino-2-phenylindole (DAPI; D9564) reagents from Sigma-Aldrich (USA); *Escherichia coli* K-12 (ATCC® 25404™) from PLS (Korea); Luria–Bertani broth (LB broth; 244620) from Becton, Dickinson and Company (USA); and red fluorescent polystyrene beads (Fluoro-Max R0100; diameter: 1 μm) and phosphate buffered saline (PBS; Gibco™ 10010023; 1×, pH 7.4) from Thermo Scientific (USA). Distilled water (18.2 MΩ·cm) was obtained through university- provided water pipelines.

2.2.2 Numerical Analysis

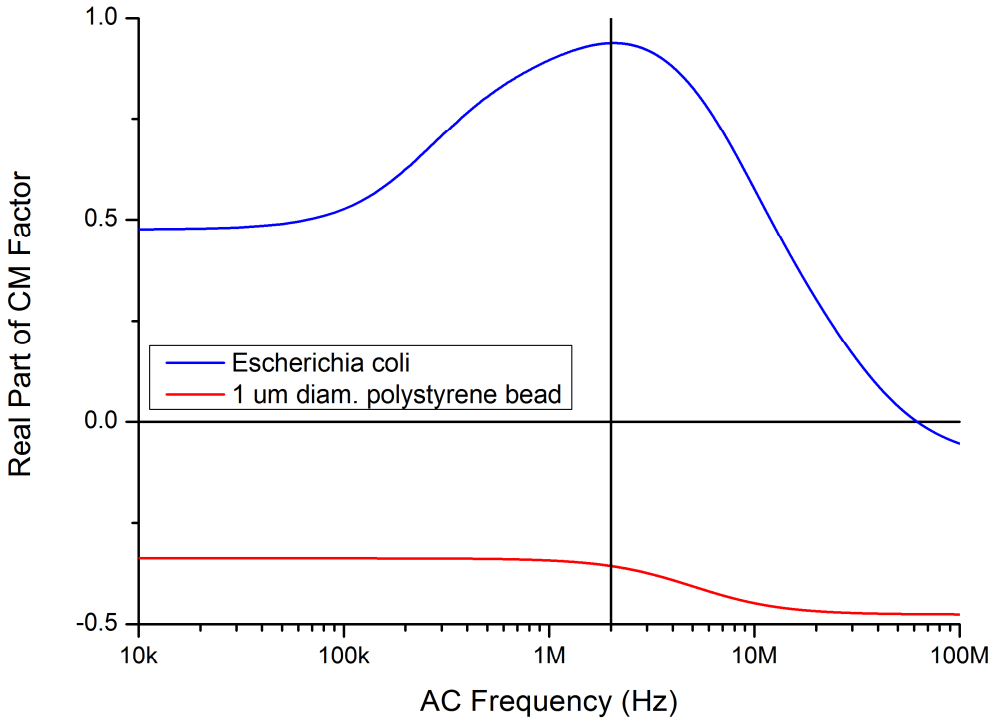

Figure 2-6. Real parts of the Clausius-Mossotti (CM) factors for *E. coli* and 1-µm-diameter polystyrene beads, suspended in 0.01× PBS buffer (199 µS/cm).

The MED algorithms were run using a commercial software, MATLAB R2018a. $Re[f_{CM}(\omega)]$ values were analyzed with respect to the AC frequency for *E. coli* and 1-µm-diameter polystyrene beads suspended in 0.01× PBS buffer using the same software to determine the optimal conditions for the selective capture of the bacteria from a bacteria-bead mixture (Fig. 2-6). A commercial software, COMSOL Multiphysics® 4.3, was also used to calculate the volumetric flow fields, electric fields, and particle trajectories for all the devices having IDEs and MED-optimized electrodes. A 720 µm long (x-), 90 µm wide (y-), and 18 µm high (z-) microchannel with different electrode patterns on the bottom surface was designed. Flow and electrostatics modules were used, and the obtained flow fields and electric potential distributions were used in the particle tracing module.

For steady incompressible laminar flow calculation, the governing equations were $\underline{\nabla} \cdot \overline{u} = 0$ and $\rho(\overline{u} \cdot \underline{\nabla})\overline{u} = \underline{\nabla} \cdot \left[-pI + \mu\left(\underline{\nabla}\overline{u} + (\underline{\nabla}\overline{u})^{\mathrm{T}}\right)\right]$, where $\overline{u}$ is the flow velocity vector, p is static pressure, ρ is the density, and μ is the dynamic viscosity of a fluid. Fully-developed velocity inflow and zero pressure were set at the inlet and outlet, respectively, and the other walls were set to no-slip boundary conditions ($\overline{u} = 0$). Newton-Raphson algorithms were employed to solve the nonlinear

static finite element problems, with an iterative solver being the generalized minimum residual method for the linear systems having non-symmetric matrices in each step, and hence $\overline{u}$ and p fields were obtained along the volumetric domain.

Laplace equation, $\nabla^2\varphi = 0$, was solved to find the electric field potentials, and as for the boundary conditions, external electrical sinusoidal signals were biased to the planar electrodes with 180° out of phases (red and blue electrodes from the MED process), and for the quasi-static electric field, the root-mean-squared (rms) electric potential is expressed as,

$$V_{rms} = \sqrt{\frac{1}{T}\int_{t_0}^{t_0+T}\left(\frac{V_{pp}}{2}\sin\omega t - \frac{V_{pp}}{2}\sin(\omega t+\pi)\right)^2 dt}, \quad (27)$$

where V_{rms} is the rms-valued electric potential, T is the period of the sinusoidal signal, t_0 is an arbitrary time, V_{pp} is the peak-to-peak electric potential of the signal, ω is the angular frequency of the signal, and t is the time. All boundaries except for the electrodes were applied by zero charge (Neumann boundary conditions), and $V_{rms}/2$ and $-V_{rms}/2$ were given on the red and blue electrodes, respectively (Dirichlet boundary conditions) (Green *et al.* 2001; Oh *et al.* 2009). Conjugate gradient method was used as an iterative solver to solve the linear static finite element problems having symmetric matrices for the φ along the entire domain. Electric field vector fields were obtained by $\overline{E} = -\underline{\nabla}\varphi$.

Particle tracing was conducted for the bacteria using the Newtonian force model,

$$m_p\frac{d^2\overline{x}_p}{dt^2} = \overline{F}_{drag} + \overline{F}_{gravity} + \overline{F}_{buoyancy} + \overline{F}_{DEP} = -3\pi\mu d_p\left(\frac{d\overline{x}_p}{dt} - \overline{u}\right) + m_p\frac{\rho_p-\rho}{\rho_p}\overline{g} + \frac{\pi}{4}{d_p}^3\varepsilon_m Re(K)\underline{\nabla}\left|\overline{E}\right|^2, \quad (28)$$

where m_p is the particle mass, $\overline{x}_p$ is the position vector of the particle, d_p is the particle diameter, ρ_p is the particle density, $\overline{g}$ is the gravity vector, ε_m is the electrical permittivity of media, $Re(K)$ is the real part of the CM factor. Here, the bacteria were assumed to be 1-μm-diameter spheres, with ρ_p of 1160 kg/m^3 (Godin *et al.* 2007) and $Re(K)$ of 0.93666 (Fig. 2-6). The predetermined $\overline{u}$ and $\overline{E}$ were used for the particle tracing, and a transient implicit solver generalized alpha was used with automatically chosen time steps. A total of 352 (44×8) particles were equally distributed at the inlet, and their trajectories were analyzed (Fig. 2-11).

To verify the solution convergence, mesh sizes were varied, and the velocity profile, $\left|\partial\left|\overline{E}\right|^2/\partial z\right|$, and final z-directional positions were checked for flow, electrostatics, and particles tracing, respectively. Also, the element order (4, 10, 20, 35 nodes per each tetrahedral element for 1st, 2nd, 3rd, and 4th order elements, respectively) was tested for flow and electrostatic simulations, and time step was controlled to acquire converged particle trajectories. The determined numerical conditions for the converged solutions were listed in Table 2-2.

2.2.3 Preparation of Bacteria-Bead Mixture with Fluorescence Labeling

For the DEP capture experiments in the two types (IDE and MED) of microfluidic channels, the bacteria and beads solutions were prepared separately, and then mixed. For the bacteria, 10 μl of *E. coli* K-12 stock was added to 10 ml of LB broth solution, and the bacteria were grown at 37 °C and 160 rpm in a shaking incubator for 12 h. The solution was then diluted 10 fold in fresh LB broth, and the optical density at 600 nm of the diluted solution was measured as 0.246, corresponding to a bacteria number density of 2.46×10^8 #/ml (Ausubel et al. 2003) The solution was centrifuged at 4000 rpm for 10 min to remove the residual LB broth, and the bacteria were re-suspended in DI water and incubated in DAPI (5 μg/ml) with blocking light for 1 h at 4 °C to distinguish them from the red fluorescent beads (Han *et al.* 2018). The labeled bacteria were centrifuged again and re-suspended in 0.01× PBS buffer. They were serially diluted to reach the bacteria number density of 1×10^7/ml. Red fluorescent polystyrene beads with a diameter of 1 μm were also suspended in 0.01× PBS buffer with a number density of 1×10^7/ml, and this bead solution was then mixed with the bacteria solution. The electrical conductivity of the mixture was measured using a conductivity meter (handylab pH/LF 12; SI Analytics GmbH, Germany), and it was 199 μS/cm at 23.1 °C.

2.2.4 Device Microfabrication and Experimental Setup

All IDE and MED-based microfluidic channels were microfabricated on glass chips. First, a 100 nm thick indium tin oxide (ITO) film was deposited on a glass substrate (wafer with a diameter of 6″) using radio-frequency sputtering, and annealed for 1 h at 400 °C in a furnace to enhance its transparency and reduce its electrical resistance. The ITO electrodes were then made by using conventional photolithography and inductively coupled plasma reactive-ion etching, and treated with oxygen plasma to remove the residual photoresists. The wafer was finally diced into chips (3.5 × 2.5 cm^2).

To fabricate the PDMS microchannel by replica molding, master molds were patterned on a silicon substrate (wafer with a diameter of 6″). SU-8 2015 was spin-coated at 2000 rpm, and the microchannel molds were patterned using conventional photolithography, with the channel mold having a width (y-) of 90.8 (±0.1) μm and a height (z-) of 18.0 (±0.3) μm. The fabricated master molds were silanized for 1 h in an evacuated chamber to aid the release of the microchannel from the mold, and then a PDMS mixture was poured onto the molds and cured at 70 °C for 2 h in an oven. The PDMS microchannel was peeled and cut off, with holes of 1 mm diameter made on its inlet and outlet reservoirs, and bonded with the prepared glass-electrodes chip by aligning the channel and electrodes manually with a microscope.

A 10 ml syringe containing the prepared bacteria-bead mixture was connected to the inlet reservoir of the device through the epoxied tubing, and controlled by a syringe pump (Harvard Pump 11 Elite, 70-4505INT; Harvard Apparatus, USA) with infusing flow rates from 100 to 400 nl/min corresponding average flow velocities of 1.02 (±0.02) to 4.08 (±0.07) mm/s, respectively. Electrical wires were epoxy-bonded to the contact pads of the electrodes and electrically biased by external AC voltages using a two-channel arbitrary function generator (AFG3022C; Tektronix, USA). The electrical potential was varied from 1 to 4 Vpp at a fixed optimal frequency of 2 MHz, which resulted in $Re[f_{CM}(\omega)]$ values of 0.94 and -0.17 for the bacterial capture and bead levitation from electrodes, respectively (Fig. 2-6). These two sinusoidal AC signals had the same amplitudes and frequencies with 180° out of phase. The signals were monitored with a digital oscilloscope (DPO3014; Tektronix, USA).

A cooled interline transfer charge-coupled device camera (ORCA-R2; Hamamatsu, Japan) connected to an inverted fluorescent microscope (Eclipse Ti-U; Nikon, Japan) was used to take images with an exposure time of 100 and 40 ms for bacteria and beads, respectively. The number of captured particles (bacteria or beads) were measured by dividing the total area occupied by the particles by that occupied by a single particle area in the fluorescence images (Han *et al.* 2018; Yang *et al.* 2006).

2.2.5 Statistical Analysis

Each experiment in this study was conducted at least six and three times for the bacteria and beads, respectively. Statistical analysis was performed using one-way analysis of variance (ANOVA) followed by the Tukey post hoc test. Significantly different data (p < 0.05, 0.01, and 0.0001) are designated with asterisks (*, **, and ***, respectively).

2.3. Results and Discussion

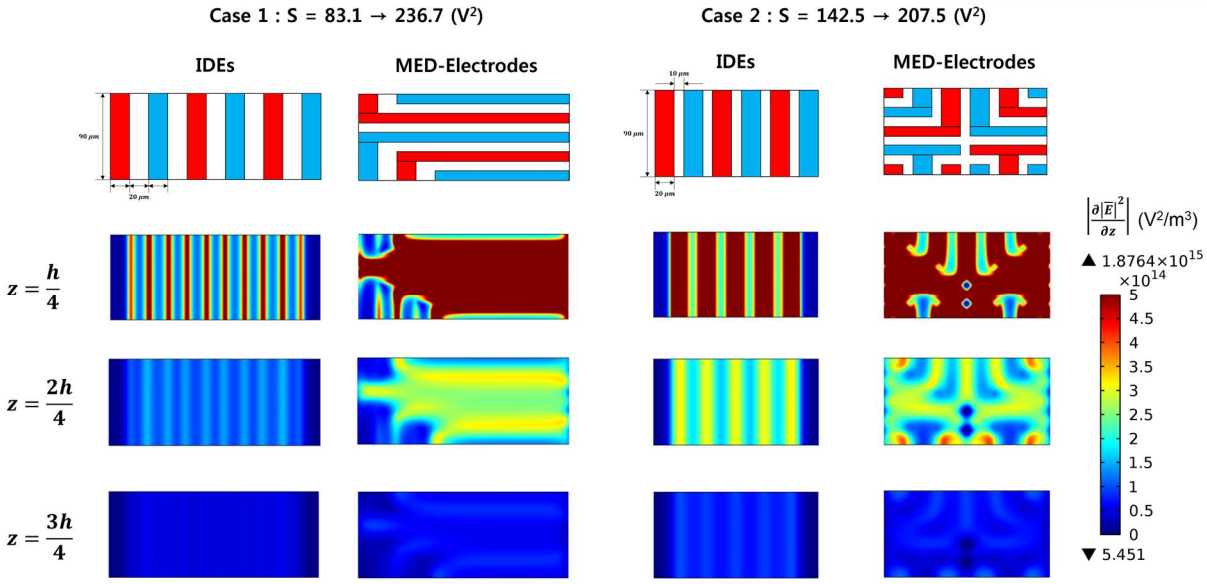

Figure 2-7. MED-optimized electrodes generated from six lines of IDEs having an electrode width of 20 μm and gaps of **(a)** 20 μm and **(b)** 10 μm, with the corresponding $\left|\partial\left|\overline{E}\right|^2/\partial z\right|$ (V^2/m^3) at different heights (h/4, 2h/4, and 3h/4) in the fabricated microfluidic channel having a channel height (h) of 18 μm.

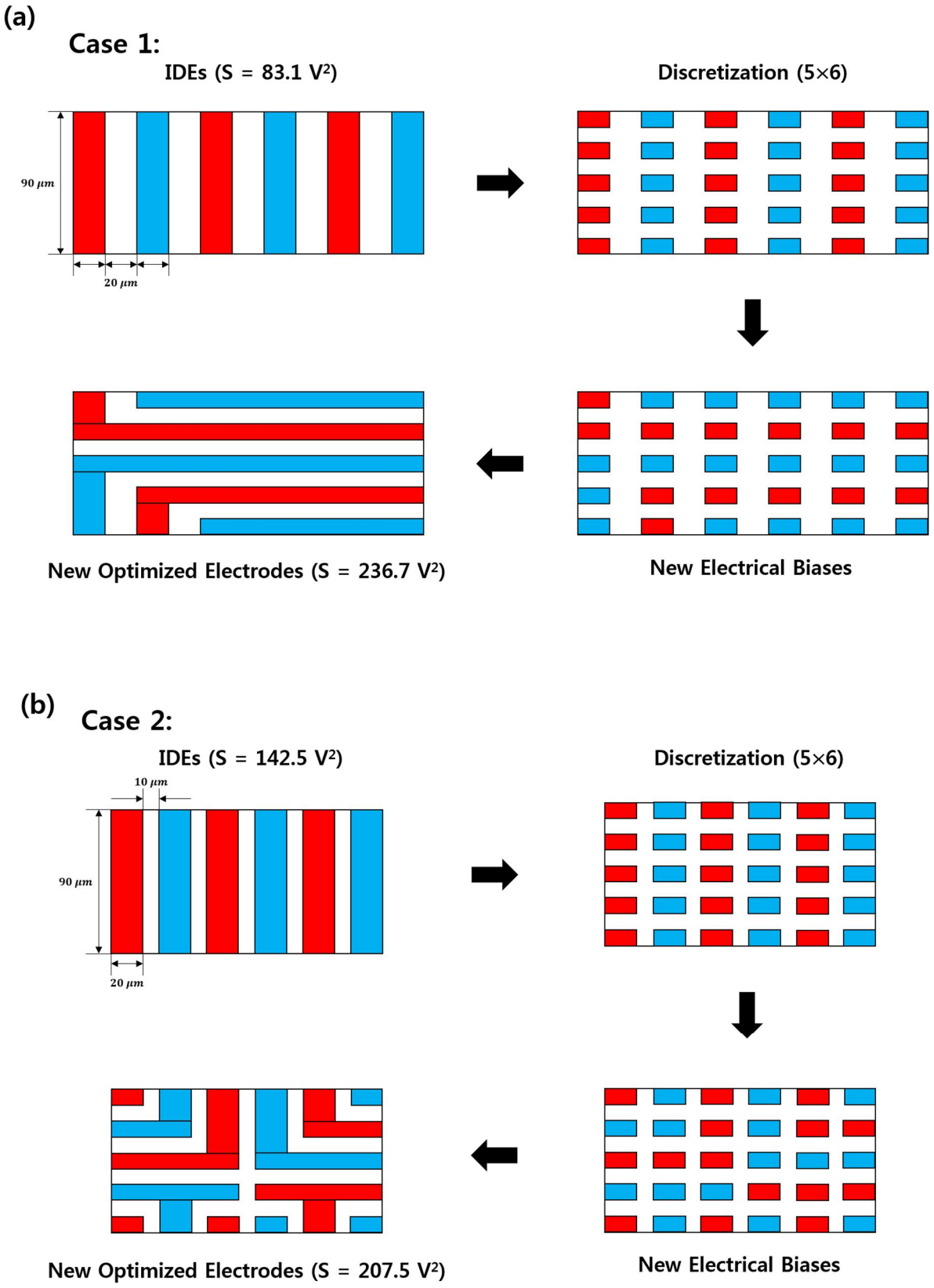

Figure 2-8. MED process for 6 lines of IDEs. **(a)** case 1. **(b)** case 2.

The MED method was applied to two arrays of IDEs consisting of six IDEs with a width of 20 μm and a length of 90 μm. These two arrays of IDEs involved gaps of 20 μm and 10 μm between adjacent electrodes, and the minimal geometric feature size was chosen as 10 μm to allow for simple and inexpensive mask manufacturing for photolithography (Rosenthal Voldman 2005). Six IDEs having a gap of 20 μm (Case 1; **S** = 83.1 V^2) were discretized into 30 equally-sized E-cells (20 μm × 10 μm), and all the possible combinations of the electrodes were tested to determine which one showed the greatest **S** (Fig. 2-8a). The factor **S** value of the MED-optimized electrodes (MED-optimized electrodes) was increased to 236.7 from 83.1 (V^2) under 855 grids, and both the IDEs and MED-optimized electrodes occupied the same working area of 220 × 90 μm^2. Another array of six IDEs having a gap of 10 μm (Case 2; **S** = 142.5 V^2) were also discretized into 30 E-cells (20 μm × 10 μm) under the same grid conditions as in case 1 (Fig. 2-8b), and a new MED-optimized electrode pattern (**S** = 207.5 V^2) was found. Both the IDEs and MED-optimized electrodes occupied the same working area of 170 × 90 μm^2 in case 2.

Table 2-2. Numerical conditions for the converged solutions.

	Laminar Flow	**Electrostatics**	**Particle Tracing**
Tetrahedral Mesh Element Number	104,812	1,332,327	4,738,566
Element Order	2nd (velocity), 1st (pressure)	4th (electric potential)	
Time Step	-	-	6.13e-7 to 1 s
Solving Time	2 min 37 sec	20 min 28 sec	11 hr 39 min 50 sec
RAM Usage	3.35 GB	39.46 GB	15.89 GB

An electrostatics simulation was conducted using COMSOL to calculate $\partial|\overline{E}|^2/\partial z$ for the volumetric rectangular domain (540 × 90 × 18 μm^3) containing each of the four different electrode patterns (IDEs and MED-optimized electrodes in cases 1 and 2) on the bottom surface (Fig. 2-7). The MED-optimized electrodes showed higher downward DEP forces more widely. The corresponding $\int_0^a \int_0^b \left(\int_0^h \partial|\overline{E}|^2/\partial z\, dz\right) dydx$ was also calculated for each of the patterns. The calculated values were changed from the IDEs to the MED-optimized electrodes (from -133.7 to -511.8 (V^2) for case 1 and from -266.4 to -439.0 (V^2) for case 2), showing enhanced DEP forces along the volumetric domain of the devices by using the MED method. As the electrode gap of the IDEs was the smaller in case 2, the ratio of the factor **S** value (MED-optimized electrodes / IDEs), that is, the increase in DEP forces by using the MED method, was more reduced in case 2 (×1.5) than in case 1 (×2.8).

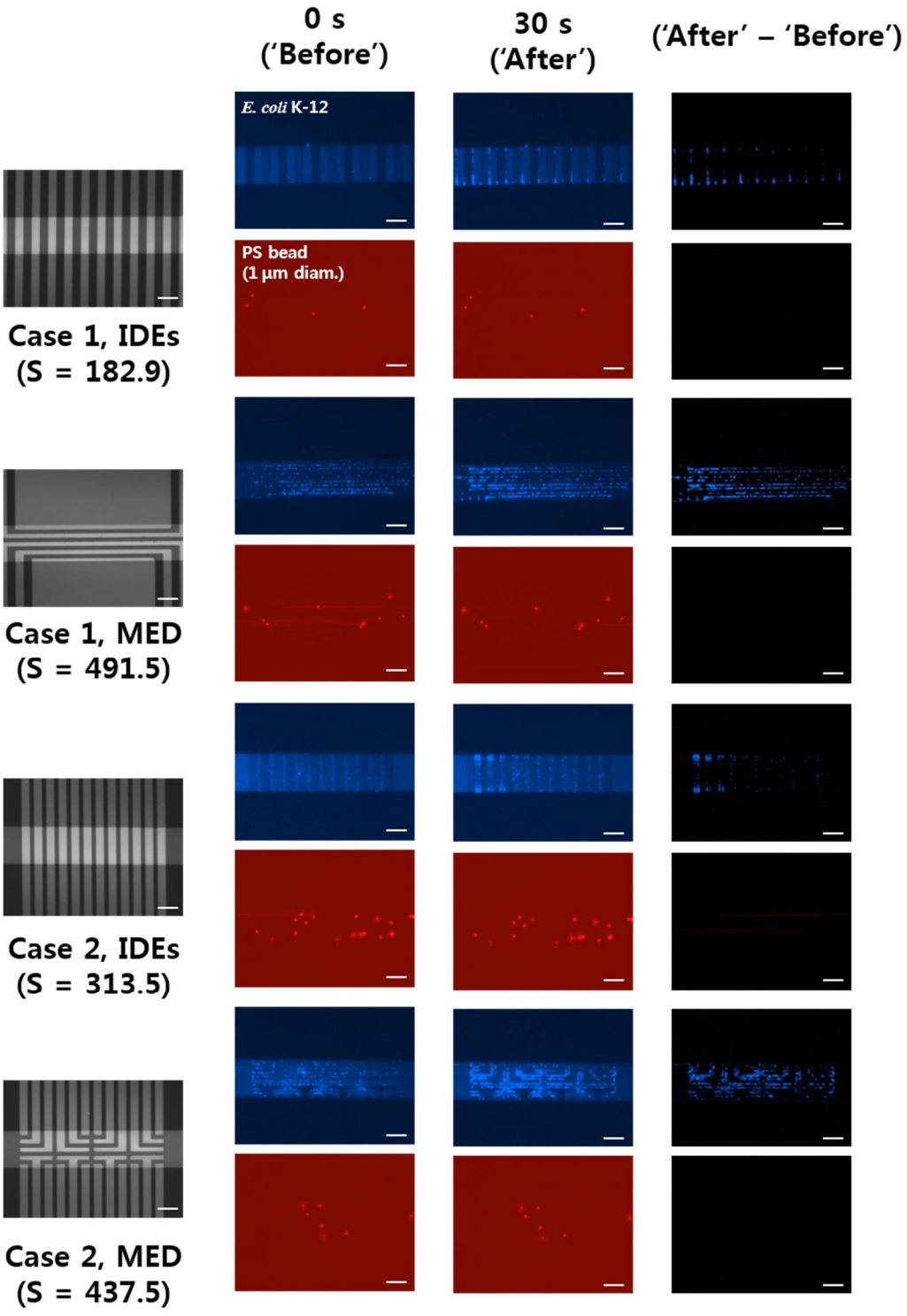

Figure 2-9. Bright field images of electrodes and fluorescence images of DEP-concentrated bacteria against beads before and after biasing the electrical signal of 2 Vpp at 2 MHz with a flow rate of 400 nl/min for all the IDEs and MED-optimized electrodes from cases 1 and 2. The rightmost images were obtained by subtracting the intensity of the "Before" images from that of the "After" images using ImageJ. The white scale bars represent 50 μm.

Figure 2-9 shows the bright field images of the microfabricated electrodes and the fluorescence images of the captured bacteria on the electrodes. Here, all the four patterns, the six lines of IDEs (**S** = 83.1, 142.5), and the corresponding MED-optimized electrodes (**S** = 236.7, 207.5) were duplicated for the measurements of large areas. The resulting 12 lines of IDEs and the duplicated MED-optimized electrodes showed **S** values of 182.9 (case 1, IDEs), 313.5 (case 2, IDEs), 491.5 (duplicated MED-optimized electrodes of case 1), and 437.5 (duplicated MED-optimized electrodes of case 2). Except for the electrode patterns on the bottom surfaces, the other conditions (microchannel dimensions, applied electrical signals, flow rates, bacteria-bead mixture solutions, etc.) were identical for all experiments. Bacteria were captured on the bottom surface by the downward pDEP forces, whereas the beads were levitated by upward nDEP forces from the electrodes. Therefore, the purity of the captured bacteria against the beads, i.e., the separation efficiency,[35] was maintained at more than 99.8% for all the patterns, demonstrating the selective DEP capture of the bacteria.

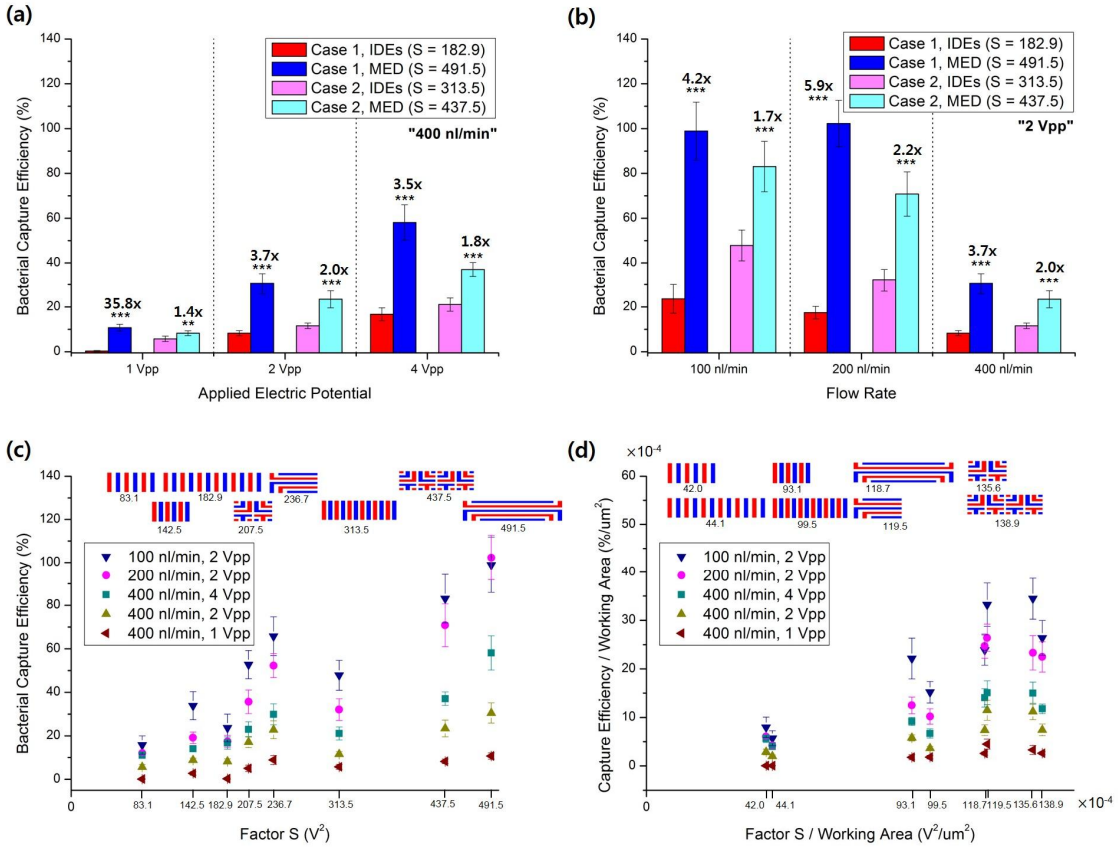

Figure 2-10. Number of bacteria captured after 30 s following electric field activation with **(a)** different applied electric potentials with a fixed flow rate of 400 nl/min and **(b)** different flow rates with a fixed applied electric potential of 2 Vpp. The values on the bars of the MED cases indicate the ratio of the

bacteria captured by the MED-optimized electrodes to those captured by the IDEs, showing the capture enhancement achieved by using the MED-optimized electrodes. **(c)** Bacterial capture efficiency, the ratio of the captured bacteria on the bottom surface to the number of total incoming bacteria, vs. **S** value. **(d)** Bacterial capture efficiency per the working area vs. **S** value per the working area. The average values are shown with their standard deviations indicated as error bars.

Figure 2-10a shows the bacterial capture efficiency at different applied electric potentials (1, 2, and 4 Vpp) at a flow rate of 400 nl/min during the electrical bias time of 30 s for the tested electrode patterns (Fig. 2-9). The number of incoming bacteria (500, 1000, 2000) and the flow velocity (1.02, 2.04, and 4.08 mm/s) increased with increasing flow rates (100, 200, and 400 nl/min, respectively) at the specific time intervals, and the efficiency was defined as the number ratio of the captured bacteria on the bottom surface to the number of total incoming bacteria. Higher bacterial capture efficiencies were observed when the applied electric potentials were higher, when the MED-optimized electrodes were used, or when the electrode patterns had higher values of **S**. Interestingly, although the MED-optimized electrode for case 1 showed a 2.7 times higher value of **S** than the IDEs, the capture efficiency of the MED-optimized electrodes was 35.8 times higher than that of the IDEs for an electric potential of 1 Vpp, demonstrating the effectiveness of the MED-optimized electrodes. The increase in the efficiencies for both the IDEs and MED-optimized electrodes generally decreased with increasing electric potential.

Figure 2-10b shows the bacterial capture efficiency at different flow rates (100, 200, and 400 nl/min) at a constant applied electric potential of 2 Vpp for the same electrode patterns. The MED-optimized electrodes showed much higher capture efficiencies than the IDEs for all the tested flow rates. The higher the value of **S**, the higher the bacteria captured on the electrodes. In fact, the bacterial capture efficiency for the MED-optimized electrodes for case 1 reached almost 100% at flow rates from 100 to 200 nl/min because of the higher electric field gradients of the MED-optimized electrodes, while the IDEs of case 1 showed a bacterial capture efficiency of approximately 20%. Moreover, the bacterial capture efficiency decreased with increasing flow rate except for 200 nl/min for case 1, in which the electric field gradients of the MED-optimized electrode were sufficient to attract all the bacteria.

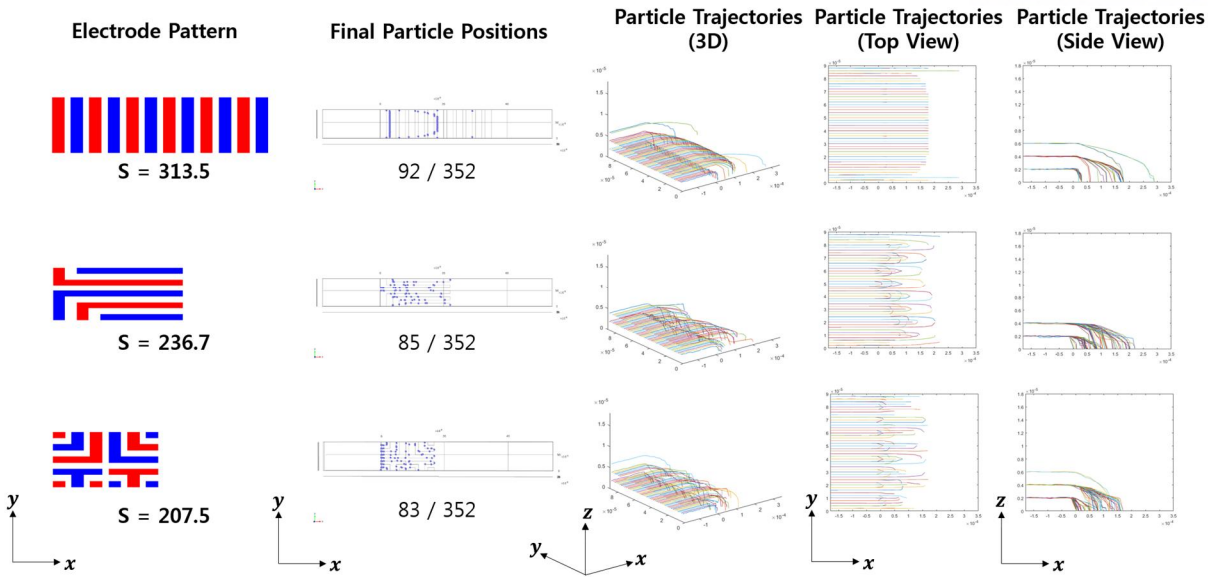

Figure 2-11. Particle trajectories for three electrode patterns having **S** values of 313.5, 236.7, and 207.5 (V^2).

Table 2-3. S values for various electrodes.

Electrode Pattern	Factor S	(Fig. 2-2e)	Electrode Pattern	Factor S	(Fig. 2-8, 2-9, 2-10, 2-11)
	9.6	①		83.1	IDEs (6-line; case 1)
	10.5	②		142.5	IDEs (6-line; case 2)
	14.8	③		182.9	IDEs (12-line; case 1)
	15.6	④		207.5	MED-Electrodes (from 6-line IDEs; case 2)
	16.5	⑤		236.7	MED-Electrodes (from 6-line IDEs; case 1)
	19.2	⑥		313.5	IDEs (12-line; case 2)
	19.2	⑦		437.5	MED-Electrodes (from 12-line IDEs; case 2)
	20.1	⑧		491.5	MED-Electrodes (from 12-line IDEs case 1)
	24.0	⑨			

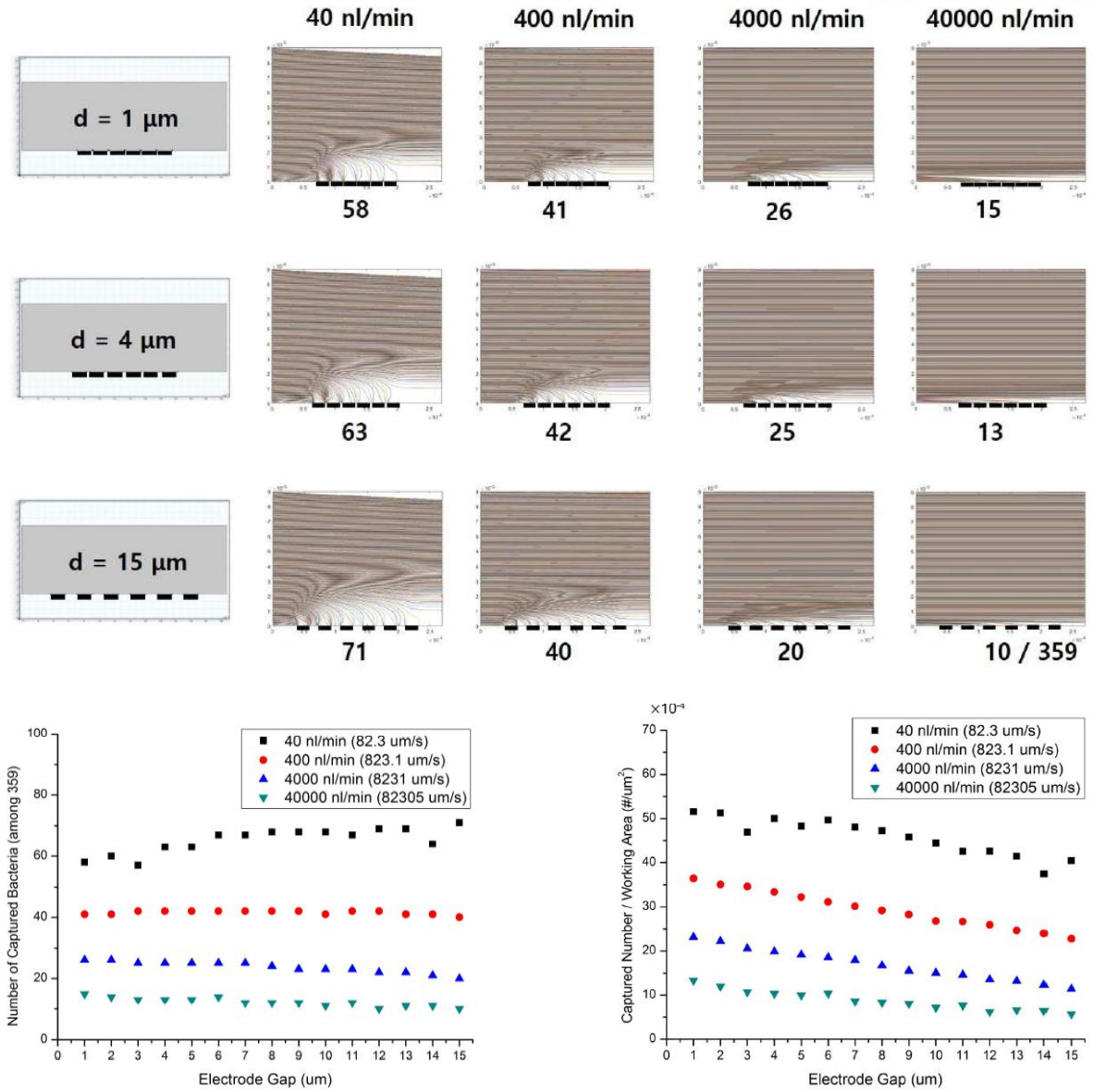

Figure 2-12. The particle tracks for different electrode gaps and flow rates.

It was observed earlier that the bacteria capture generally increased with an increase in **S** for all the electrode patterns considered (eight patterns; six lines of IDEs, 12 lines of IDEs, and every corresponding MED-optimized electrode) under the various flow rates and applied electric potentials (Fig. 2-10c), which was expected from the derivation of **S**. Interestingly, the numbers of bacteria captured with the 12 lines of IDEs (**S** = 313.5) were significantly less ($p < 0.0015$) than or similar ($p < 0.96$) to those captured with the unduplicated MED-optimized electrodes of case 1 (**S** = 236.7) and 2 (**S** = 207.5). As the goal of the MED method is to enhance the volumetric downward DEP force by considering the electric fields on the electrodes alone, the velocity profiles in the microfluidic channels were not considered although they can influence the bacteria capture, as observed in the field-flow fractionation techniques (Yang *et al.* 2000). Therefore, particle trajectories were numerically

investigated for the domains having each of these three patterns. In fact, the number of captured particles was proportional to **S** when 352 simulated particles were uniformly distributed on the inlet surface (Fig. 2-11). In other words, particle capture by DEP may increase with the increasing value of **S** if the particles are uniformly distributed on the inlet surfaces. However, particle positions on the cross-sections may change during the trajectory of the particles through the tubing and channel, and hence particle density may not be fully uniform on the cross-sections.

Furthermore, the DEP force generated by the conventional IDEs are rather periodic (strong-weak-strong-weak-…) in the streamwise direction (Fig. 4). 2D simulations were conducted on six IDEs having 20 μm widths and different gaps ranging from 1 to 15 μm in a 90 μm high microfluidic channel using COMSOL (Fig. 2-11). The flow rates changed from 40 to 40000 nl/min, and -1 V and +1 V were applied to the electrodes. The number of captured particles increased with the electrode gap for lower flow rates and decreased for higher flow rates. This is because the low electric field intensity in the larger gaps may be sufficient for particle capture because of low flow rates. Also, larger gap IDEs have larger working areas, which means that electric field is applied over large areas, and hence the particles under the electric field may have a higher probability to be captured on the electrodes.

Therefore, I also plotted the number of captured particles based on the number density (the number of captured particles/working areas), and the particle capture density decreased with the electrode gap for all flow rates, as shown below. Interestingly, the electrode with 3 μm gap has higher values of S and S/working area, but had lower particle capture density than 12 the electrode with 4 μm gap for 40 nl/min (the lowest flow rate case) although the particle capture density increased with the increasing values of S and S/working area for other flow rates. Even for the lowest flow rate case, the general trend shows that the particle capture density increased with the increasing values of S and S/working area.

As a result, particle capture is quite dependent on the positions of the particles on the inlet surfaces, and the particles were not captured uniformly on the electrodes (Figs. 5 and 7); hence, the number of captured particles may not be linearly proportional to the working area and **S** for IDEs, and care needs to be taken for the direct comparison of **S** values between two different patterns for comparing particle captures (Fig. 2-12). In this case, the area density of **S** values can be considered more appropriate (Fig. 2-10d), and the bacterial capture efficiency per the working area generally increased with the area density of **S** values.

In contrast to IDEs, as the DEP force of the MED-optimized electrodes appeared to be more non-uniform and irregular in the streamwise direction (Fig. 4), particle capture was less sensitive to the initial positions of the bacteria at the inlet, and the particles were captured much more uniformly on the electrodes (Figs. 5 and 7). This can be considered an advantage of the MED-optimized electrodes, which makes them suitable for practical applications.

2.4. Conclusions

An array of IDEs is one of the most widely used planar electrodes in many DEP-based microfluidic devices; however, IDEs often show inefficiencies in DEP particle manipulation owing to the limited DEP-effective region. Herein**,** the MED method was presented that can generate planar electrode patterns with enhanced electric fields by simple electrode discretization and reconstructions. a novel objective function was presented as well, factor **S**, calculated on the electrode surface that enables 2D computation of the downward dielectrophoretic forces or $\partial\left|\overline{E}\right|^2/\partial z$ for the overall volumetric domain. The MED-optimized electrodes were determined based on the value of factor **S,** and as the factor **S** increased, the particle capture increased (Figs. 2-10a and 2-10b). The MED-optimized electrodes captured 1.4 to 35.8 times more bacteria ($p < 0.0016$) than the respective IDEs, with a bacterial purity against the beads of more than 99.8%. In this study, values of factor **S** were computed for the discretized electrodes generated from IDEs for comparison; however, this method can be applied to any planar electrodes. I strongly believe that this method has the potential to be used for many electrode-based microfluidic devices and sensors (Sharma *et al.* 2016; Galvan *et al.* 2018).

Chapter 3. Signal Superimposition of EO and DEP

(Note: This chapter is partially or totally adapted from the published journal paper of myself, Han *et al.* 2018.)

3.1. Theory

The time-averaged dielectrophoretic force exerted on a particle suspended in a medium of electrical permittivity ε_m under a non-uniform electric field is expressed as (Pohl, 1951; Pohl, 1978; Huang *et al.* 2001)

$$\overline{F}_{DEP} = 2\pi\varepsilon_m {r_p}^3 Re[f_{CM}(\omega)]\underline{\nabla}\left|\overline{E}_{rms}\right|^2, \quad (1)$$

where r_p is the radius of the particle, $Re[f_{CM}(\omega)]$ is the real part of the Clausius-Mossotti (CM) factor depending on the angular frequency (rad/s), ω, of AC signals, and $\overline{E}_{rms}$ is the root-mean-squared electric field intensity vector. When the CM factor is not available for a particle suspended in a medium, the optimal magnitude and frequency of the dielectrophoretic force can be experimentally determined by varying the AC frequency.

Regarding the optimal electroosmosis (EO) conditions, when slip flow is induced on the coplanar electrodes due to AC EO, the time-averaged velocity can be expressed as, under an assumption of negligible Stern layer effects (Ramos *et al.* 1999; Oh *et al.* 2009; Swaminathan *et al.* 2015),

$$\langle v_{ACEO}\rangle = \frac{\varepsilon_m {\varphi_0}^2 \Omega^2}{8\mu x(1+\Omega^2)^2}, \quad (29)$$

$$\Omega = \frac{\pi x \varepsilon_m \omega}{2\sigma_m \lambda_D}, \quad (30)$$

where φ_0 is the initial potential, Ω is a non-dimensional frequency, μ is the dynamic viscosity, x is the position starting from the center of the gap between the two coplanar electrodes, σ_m is the electrical conductivity of media, and λ_D is a Debye length. The optimal AC frequency is one that provides the highest $\langle v_{ACEO}\rangle$.

3.2. Materials and Methods

3.2.1. Materials

The following materials were purchased from commercial sources: 4',6-diamidino-2-phenylindole (DAPI; D9564), rhodamine B (Rh-B; R6626), dialysis tubing (D0405-100FT; molecular weight cut-off: 12400), N-hydroxysuccinimide (NHS; 130672), N-(3-dimethylaminopropyl)-N'-ethylcarbodiimidehydrochloride (EDC; 03449) from Sigma-Aldrich (USA); polydimethylsiloxane

(PDMS; Sylgard® 184) from Dow Corning Corp. (USA); sterile Acrodisc® syringe filters with Supor® membrane (4612; pore size: 0.2 μm) from Pall Corporation (USA); phosphate buffered saline (PBS; 20×, pH 7.4) from Biosesang Inc. (Korea); Luria-Bertani broth (LB broth; 244620) and tryptic soy broth (TSB; 211825) from Becton, Dickinson and Company (USA); fluorescent PS beads (Fluoro-Max R0100; diameter: 1 μm) from Thermo Scientific (USA); *Escherichia coli* K-12 (ATCC® 25404™), *Escherichia coli* C3000 (ATCC® 15597™), and MS2 bacteriophages (ATCC® 15597-B1™) from PLS (Korea); and FITC-linked polyclonal antibody to troponin I type 3, cardiac (TNNI3) (LAA478Mu81) from Cloud-Clone Corp. (USA). Distilled water (18.2 MΩ·cm) was obtained through university-established water pipelines.

3.2.2. Numerical Analysis

2D simulation was conducted using a commercial software COMSOL Multiphysics® 4.3. A 4 mm long (x-) and 1.6 mm high (y-) rectangular domain was designed according to the experiments. Quasi-static electric potential and laminar flow fields were calculated with the governing equations and boundary conditions (Fig. 3-3) (Oh *et al.* 2009). The net force fields exerted on the particles were calculated along the domain, with the Newtonian force model, which is given by

$$m_p \frac{d^2\overline{x}_p}{dt^2} = \overline{F}_{drag} + \overline{F}_{gravity} + \overline{F}_{buoyancy} + \overline{F}_{DEP} = -3\pi\mu d_p \left(\frac{d\overline{x}_p}{dt} - \overline{u}\right) + m_p \frac{\rho_p - \rho}{\rho_p}\overline{g} + \frac{\pi}{4} {d_p}^3 \varepsilon_m Re(K) \underline{\nabla}\left|\overline{E}\right|^2 = F_x\hat{\imath} + F_y\hat{\jmath}, \quad (31)$$

where m_p is the particle mass, $\overline{x}_p$ is the position vector of particle, d_p is the particle diameter, ρ_p is the particle density, and $\overline{g}$ is the gravity vector. Here, both bacteria and beads were assumed to be 1-μm-diameter spheres, with ρ_p of 1160 (Godin *et al.* 2007) and 1050 kg/m^3, respectively, and $Re(K)$ values were considered according to Fig. 3-3a.

For the electrostatics, multifrontal massively parallel sparse direct solver was used to solve the linear static finite element problems having symmetric matrices for the φ along the entire domain. The converged solutions for $\left|\underline{\nabla}\left|\overline{E}\right|^2\right|$ were obtained for 305,460 elements with 3rd-order elements for the φ (10 nodes per each element). Flow fields were solved using Newton-Raphson algorithms to solve the nonlinear static finite element problems, with an iterative solver (generalized minimum residual method) for the linear systems having nonsymmetric matrices in each step, and hence $\overline{u}$ and p fields were obtained along the domain, where $\overline{u} = u_x\hat{\imath} + u_y\hat{\jmath}$. Convergence of the flow velocity magnitudes was verified at the number of triangular mesh element of 104,217 with 1st-order elements for u_x, u_y, and p (3 nodes per each element).

Particle tracing was conducted using a transient implicit solver (generalized alpha) with automatically scaled time step sizes. 1020 particles were equally distributed at rest ($\frac{d\overline{x}_p}{dt} = 0$), and the

predetermined $\overline{u}$ and $\underline{\nabla}\left|\overline{E}\right|^2$ were coupled. Numerical convergence of the particle position was verified at the number of triangular mesh element of 305,460 with the time step between 2.9e-8 to 0.5 s.

3.2.3. Microfabrication of Chips and Experimental Set-up

Two 100-nm-thick indium tin oxide (ITO) coplanar electrodes were fabricated on a glass wafer (6 in. diameter) with 25 μm gaps, using the conventional photolithography and radio-frequency sputtering. The ITO electrodes were then annealed for 1 h at 400 ℃ in an oven for transparency and electrical resistance reduction. The wafer was diced into chips (1×1 cm^2) with two coplanar electrodes on each chip, which are shown in the bright field image in Fig. 3-1a. An inverted microscope (Eclipse Ti-U; Nikon, Japan) was used to observe the particle motion around the electrodes, maintaining the optical focus on the transparent electrode surface. A 30 μl PDMS well was located at the center of the chip, and 20 μl of the prepared solution was added into the well. Different electrical signals were then applied to the ITO electrodes for either 30 s (for the bacteria–beads) or 1 min (for the viruses and proteins).

Two dual-channel arbitrary function generators (AFG3022C; Tektronix, USA) were used to generate sinusoidal signals 180° out of phase. Four signals from the two function generators were superimposed by a lab-made voltage adder consisting of impedance buffers and frequency mixers, and the signals were monitored by an oscilloscope (DS2072A; RIGOL Technologies Inc., USA) (Fig. 3-1b).

Videos and images of concentrated fluorescent particles were taken by a cooled interline transfer charge-coupled device camera (ORCA-R2; Hamamatsu, Japan), and the quantities of particles collected in the fixed regions of interests (RoI; 120×360 pixels) between the two ITO electrodes were measured using ImageJ. The numbers of particles in the RoI were determined by dividing the total particle area by the single particle area for the bacteria and beads (Yang *et al.* 2006) and by measuring the integrated intensities for the viruses and proteins (Madiyar *et al.* 2013; Liao Chou 2012). The exposure times for fluorescence imaging and video recordings were 100 ms, 40 ms, 500 ms, and 2 s for the bacteria, beads, viruses, and proteins, respectively, and the videos were recorded using the maximal frame per second setting for each experiment.

3.2.4. Preparation of Biological Particle Solutions with Fluorescence Labeling

Three types of biological particle solutions, bacteria–bead mixtures, viruses, and proteins, were prepared. For the bacteria, 10 μl of *E. coli* K-12 stock was added to 10 ml of LB broth solution, and the

bacteria were grown at 37 ℃ and 160 rpm in a shaking incubator for 12 h. They were centrifuged at 4000 rpm for 10 min to remove the residual LB broth. The remaining sunk bacteria were suspended in DI water for DAPI labeling (excitation/emission: 360/460 nm) to distinguish them from the red fluorescent beads. The labeled bacteria were then centrifuged and re-suspended in 0.01× PBS (Lapizco-Encinas 2004). The bacterial number concentration was determined by performing optical density measurements at 600 nm (Ausubel *et al.* 2003), and the final bacteria concentration was 1×10^7 #/ml. Red fluorescent (excitation/emission: 542/612 nm) PS beads 1 μm in diameter were suspended in 0.01× PBS buffer with a number density of 1×10^7 #/ml, and the bacteria and bead solutions were mixed.

For the virus experiments, freeze-dried MS2 phages were dissolved in 1× PBS to obtain a viral mass concentration of 1 mg/ml. Then, 0.5 ml of the MS2 solution was added to 10 ml of *E. coli* C3000, the host bacterium for MS2 bacteriophages, and incubated at 37 ℃ and 160 rpm for 5 h. The mixture was then centrifuged at 3000 rpm for 10 min to remove the bacteria, and the MS2-laden supernatant was filtered using a membrane filter. The prepared MS2 stock was then labeled with red fluorescence dye Rh-B (excitation/emission: 562/583 nm in water) by coupling EDC and NHS, and the stock and dye were mixed and purified in a dialysis membrane for 1 week to remove the unbound dye (Gitis *et al.* 2002). The concentration of the labeled virus stock solution was approximately 10^7 plaque forming units (pfu)/ml, which was verified by a plaque assay, and the solution was 10,000-fold diluted in DI water. For the protein experiments, FITC-labelled cTnI-Ab was used (excitation/emission: 495/525 nm), and its stock solution was 400-fold diluted in DI water for a mass concentration of 500 ng/ml. The media conductivities of all three test solutions were measured using a conductivity meter (handylab pH/LF 12; SI Analytics GmbH, Germany) (Table 3-2).

3.2.5. Statistical Analysis

Table 3-1. Obtained *p*-values from the statistical analyses.

	p-value		
	Bacteria	**Viruses**	**Proteins**
Overall ANOVA	3.33E-12	1.39E-04	1.11E-04
Means Comparisons (Tukey post hoc test)			
AC EO vs. Positive Control	0.99867	0.03941	0.9863
AC DEP vs. Positive Control	0.0337	6.96E-04	0.13508
AC DEP vs. AC EO	0.02982	0.23652	0.23767

AC EO+DEP vs. Positive Control	0	2.92E-05	2.01E-04
AC EO+DEP vs. AC EO	0	0.0043	3.29E-04
AC EO+DEP vs. AC DEP	0	0.03402	0.00238

Each experiment in this study was performed at least three times. The average values are shown in the figures with their standard deviations indicated as error bars. Statistical analysis was performed using one-way analysis of variance (ANOVA) followed by the Tukey post hoc test (Table S-1). Significantly different results ($p < 0.05$, 0.01, and 0.0001) are designated with asterisks (*, **, and ***, respectively).

3.4. Results and Discussion

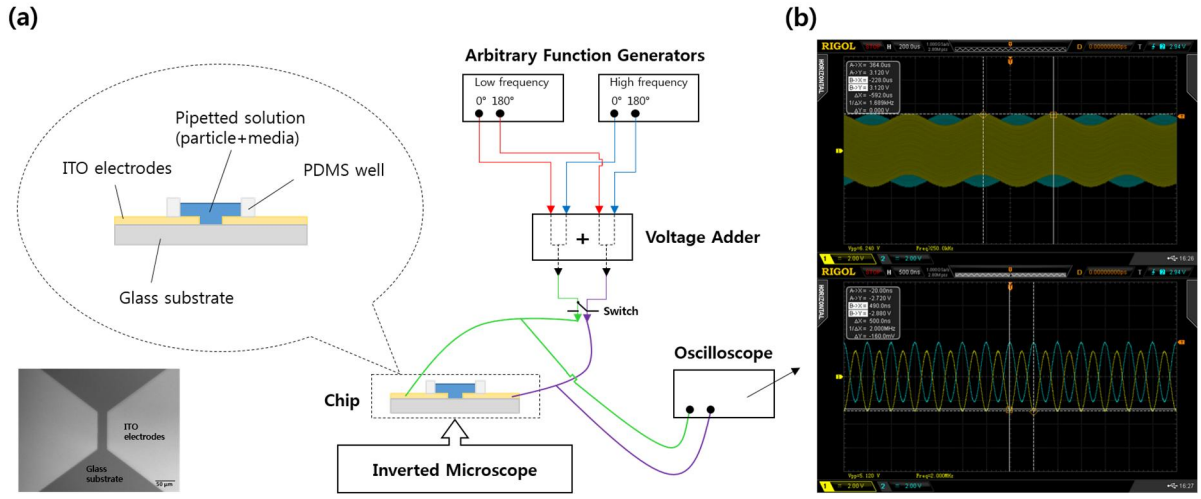

Figure 3-1. (a) Schematic of the experimental setup. **(b)** Superimposed signals: 1.2 Vpp (peak-to-peak), 1633 Hz signal for EO, and 5 Vpp, 2 MHz signal for DEP. Lower frequency (top) and higher frequency (bottom) components of the superimposed signals are shown.

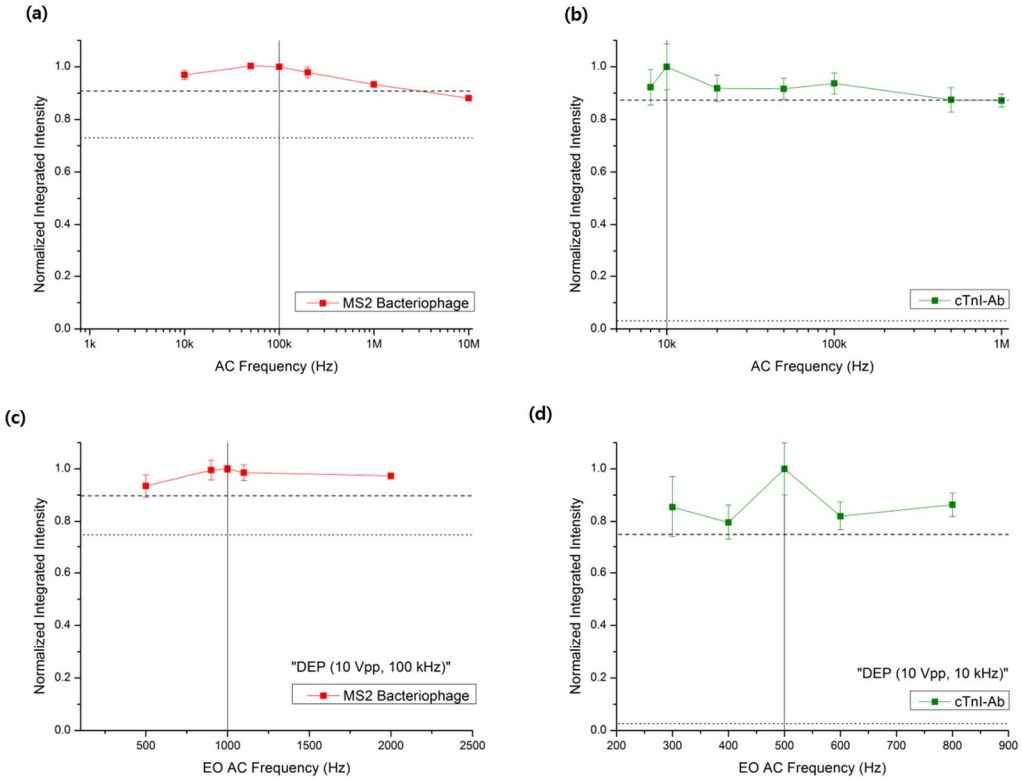

Figure 3-2. Experimentally investigated DEP capture behavior with an applied electrical potential of 10 Vpp for **(a)** MS2 viruses in DI water (4 μS/cm) and **(b)** cTnI-Ab in DI water (16 μS/cm), where the dashed and dotted horizontal lines indicate positive and negative control values, respectively. Experimentally investigated capture behaviors of **(c)** MS2 viruses, and **(d)** cTnI-Ab, when varying the EO frequencies of the superimposed signals with the previously determined DEP signals and fixing the EO electrical potential to 2 Vpp. The dashed and dotted horizontal lines indicate positive and negative control values, respectively.

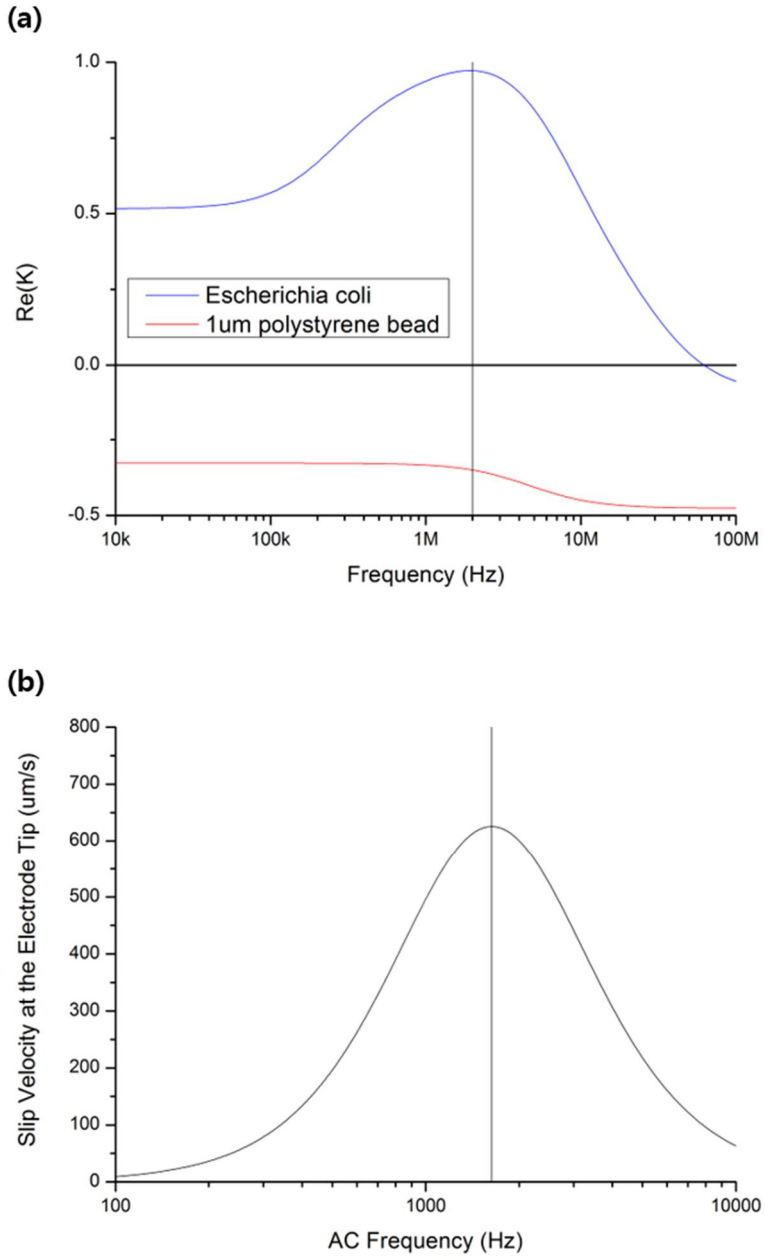

Figure 3-3. (a) Calculated real parts of the Clausius–Mossotti factors for *Escherichia coli* K-12 and 1-μm-diam. polystyrene beads, suspended in 0.01× phosphate buffered saline (PBS) (184 μS/cm). **(b)** Calculated slip velocity magnitude at the electrode tip in 0.01× PBS buffer with an applied electrical potential of 1.2 Vpp.

Table 3-2. Experimental properties and parameters of the particles and media used in this study

	Bacteria-bead mixture	**Virus solution**	**Protein solution**
Particle	*E. coli* K-12 (~0.5 μm wide and ~2 μm long) & 1-μm-diam. PS beads	MS2 bacteriophage (23–28 nm in diameter) [61]	Troponin I antibody (30 kDa)
Media conductivity (measured at 22.9 ℃, μS/cm)	184	4	16
Debye length [60]	7.61 nm (0.01x PBS)	-	-
AC frequency (EO)	1633 Hz	1000 Hz	500 Hz
AC electrical potential (EO)	1.2 Vpp	2 Vpp	2 Vpp
AC frequency (DEP)	2 MHz	100 kHz	10 kHz
AC electrical potential (DEP)	5 Vpp	10 Vpp	10 Vpp

First, the AC electrical potentials and frequencies for DEP and EO of the particles were determined. To determine these values for the optimal DEP-capture of the bacteria against the beads, the real parts of the Clausius–Mossotti (CM) factors for the bacteria and beads were plotted with respect to the AC frequency (Park *et al.* 2011) (Fig. 3-3a). The optimal EO frequency for 0.01× phosphate buffered saline (PBS) was also determined by measuring its electrical conductivity and by using the reported Debye length (Ramos *et al.* 1999) (Fig. 3-3b). For MS2 viruses and cTnI-Ab, no models on their dielectrophoretic responses have been reported on, as would be necessary to determine their CM factors; therefore, their DEP characteristics were experimentally investigated by varying the AC frequency from 8 kHz to 1 MHz for cTnI-Ab and from 10 kHz to 10 MHz for the MS2 viruses, and the frequency providing maximal capture was selected as the optimal DEP frequency (Madiyar et al. 2013; Hölzel et al. 2005) (Figs. 3-2a and 3-2b). As the Debye lengths for the salty stock solutions of the MS2 viruses and cTnI-Ab were not available, the optimal EO frequencies for the media were also experimentally determined by varying the EO frequencies of the superimposed signals, fixing the previously determined DEP signals [10 Vpp (peak-to-peak)], and finding the intermediate frequencies inducing maximal capture with low electric potentials (2 Vpp) (Gong 2010) (Figs. 3-2c and 3-2d). Here, sharp changes in the fluorescence intensities owing to captured viruses and proteins were observed over narrow and low frequency ranges (500 to 2000 Hz and 300 to 800 Hz for viruses and proteins, respectively), which is typical of EO spectra rather than DEP as DEP behavior generally changes with

wider frequency ranges (Morgan *et al.* 1997; Camacho-Alanis Ros 2015). Table 3-2 shows the obtained AC electrical potentials and frequencies for the particles and media.

The used cTnI-Ab had a weak fluorescence due to their small size (30 kDa), so camera exposure time was determined to be 2 s to enhance the fluorescence images. Exposure time of 1–9 s were reported for other proteins (Zhou *et al.* 2011; Williams *et al.* 2013) to enhance the measured signal. Moreover, the protein concentration was kept to 500 ng/ml, under which fluorescence images were not clear, and few clumps of the protein were unavoidable in the solution. The vortex flows of the clumps were occasionally observed near the electrodes when using the lower frequency (EO) and superimposed (EO+DEP), but those were not observed when using the higher frequency (DEP).

AC electrothermal (ET) flows can also be considered an alternative to AC EO flows; however, they are commonly induced by Joule heating through salty media or by heating the substrate. AC ET flow is usually dominant at high frequencies (on the order of MHz) or high electrical conductivities (>1000 μS/cm), especially if the applied electric potential is high (Park *et al.* 2009; Castellanos *et al.* 2003; Oh *et al.* 2009). In the present study, AC ET flow was negligible because low conductivity media were used with relatively low electric potentials and no heat sources. In fact, the maximum measured ET flow velocity owing to Joule heating was reported to be ~7 μm/s under the applied electric potentials of 10 Vpp (at 200 kHz) and electrical conductivity of 10000 μS/cm on 60 μm gap coplanar electrodes (Feldman *et al.* 2007), which was considerably smaller than the measured flow velocities (~107 μm/s and ~135 μm/s for the bacteria and beads respectively) around the facing electrode edges due to AC EO in the present study. These flow velocities were calculated by measuring the moving distances of the particles around the facing electrode edges during time intervals between two frames of the recorded videos. Furthermore, positive DEP (pDEP) with low conductivity media is stronger and easier to use for particle trapping than negative DEP (nDEP) with high conductivity media (Voldman 2006). However, it should also be noted that most of biological functionalities are not designed for low conductivity media, and pDEP and EO tend to drop in high conductivity media (Voldman 2006); hence pDEP and EO can be limited for certain biological applications.

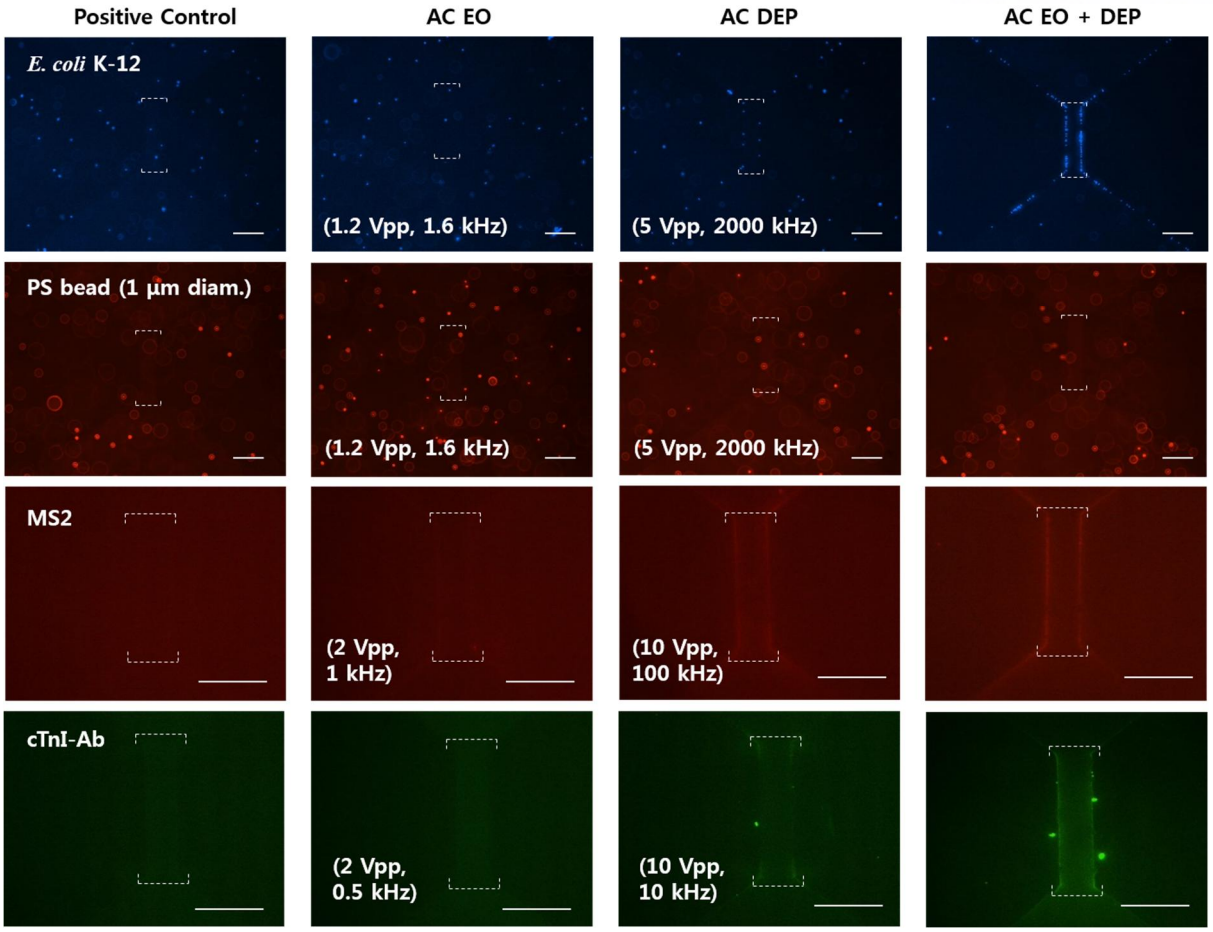

Figure 3-4. Fluorescence images of the concentrated particles after biasing different electrical signals for 30 s (*Escherichia coli* K-12 and polystyrene beads) and 1 min (MS2 viruses and cTnI-Ab). Different types of electrical signals include no signal (positive control), low frequency signals for EO (1.2 Vpp, 1633 Hz for bacteria-bead; 2 Vpp, 1000 Hz for MS2 virus; 2 Vpp, 500 Hz for cTnI-Ab), high frequency signals for DEP (5 Vpp, 2 MHz for bacteria-bead; 10 Vpp, 100 kHz for MS2 virus; 10 Vpp, 10 kHz for cTnI-Ab), and superimposed signals for EO+DEP. The white scale bars represent 50 μm, and the white dashed lines indicate the top and bottom edges of the rectangular RoIs.

Using the obtained DEP and EO conditions, electrokinetic concentration experiments were conducted for the prepared biological particle solutions with single sinusoidal signals (either DEP or EO) and superimposed signals (DEP+EO). Figure 3-4 shows fluorescence images of the particles concentrated using different treatments. The superimposed signals concentrated *Escherichia coli* K-12, MS2 viruses, and cTnI-Ab more effectively than the single treatments, as demonstrated by the shiny lines on the facing edges of the electrodes. Regarding the bead experiments, nDEP occurred at the tested frequency, so the beads were not captured in the region of interest (RoI). We also observed noticeable

particle movement under the superimposed signals in the videos, which was not observed under DEP bias only.

Figure 3-5a shows the numbers of *E. coli* K-12 collected within the RoI over time for different electrical signals. More of the bacteria were captured using the superimposed signals than any of the single electrical signals. In fact, the numbers of *E. coli* K-12 captured by EO and DEP alone are 0.4% and 9.1%, respectively, of the number collected in the superimposed signal case at 30 s. This result can be ascribed to the fact that DEP is usually effective for the particles close to the electrode surface, and EO flow can drag particles over the electrode toward the region between the electrodes without capturing most of them. The bacterial capture with EO alone in this study was not significantly different from that with no signal treatment ($p = 0.999$), whereas the bacterial capture with DEP alone was significantly different from that with no signal treatment ($p = 0.034$). By contrast, the bacterial capture with the superimposed signals was significantly larger than those with the other two electrical treatments. The superimposed signals provided the advantages of both DEP and EO, first moving distant particles toward the region between the electrodes with EO flow, and then capturing the moved particles at a particular position, where the largest electric field occurs, against the flow with pDEP. This superimposition can be employed to enhance the sensor sensitivity and reduce the detection time when used with biosensors (Sharma *et al.* 2016). In fact, the amount of DEP-assisted attachment of cTnI (cardiac troponin I) after 1 min was less than that due to sedimentation for 1 h (Sharma *et al.* 2016) in a cTnI sensor, because the proteins far from the electrode might not be attracted toward the electrode rapidly with DEP alone.

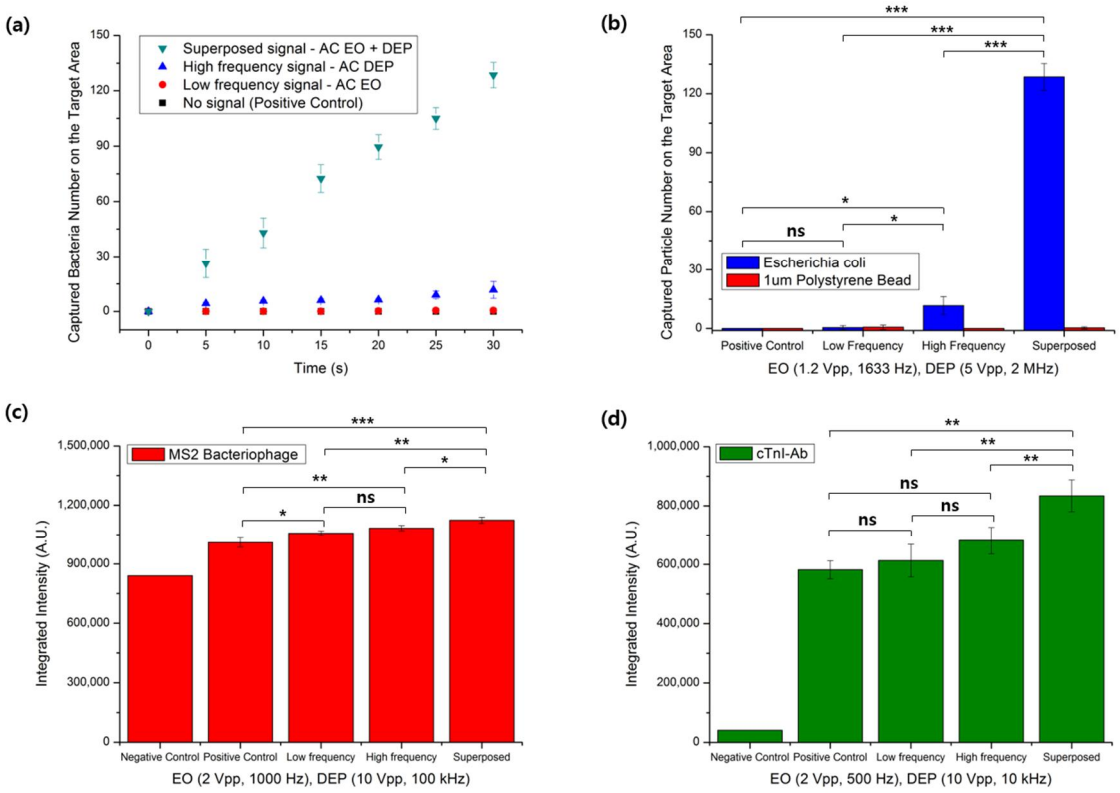

Figure 3-5. Amounts of particles collected within the RoIs using different electrical signals. **(a)** *Escherichia coli K-12* collection over time. **(b)** *E. coli* K-12 and beads collected. **(c)** Integrated intensities of concentrated MS2 viruses. **(d)** Integrated intensities of collected cTnI-Ab. The experiments were conducted for 30 s (*E. coli* K-12 and polystyrene beads) and 1 min (MS2 viruses and cTnI-Ab) using different electrical signals: no solution addition (negative control), no signal after adding the solution (positive control), low frequency EO signals, high frequency DEP signals, and superimposed signals (EO+DEP). Statistical analysis was performed using one-way ANOVA followed by the Tukey post hoc test, and statistically significant results are identified with asterisks (*, **, and *** = p values < 0.05, 0.01 and 0.0001, respectively; ns – not significant).

Figure 3-5b shows the numbers of bacteria and beads captured after applying different treatments for 30 s. A moderate speed of ~119 (±6.3) μm/s around the facing electrode edges was adopted for the superimposed treatments, because it allowed many bacteria over the electrodes to be collected by pDEP while the beads were repelled from the electrode edges by nDEP without inertial attachment to the surface, making it possible to collect the bacteria selectively from the bacteria–bead mixture.

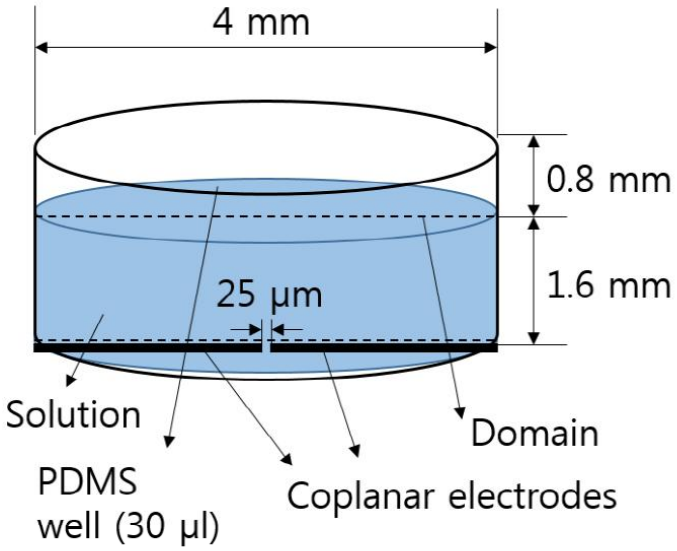

φ: electric potential; $V_{pp,EO}$: peak-to-peak EO potential; ω_{EO}: EO angular frequency; $V_{pp,DEP}$: peak-to-peak DEP potential; ω_{DEP}: DEP angular frequency; $\overline{n}$: normal vector at the boundary; $\overline{u}$: flow velocity vector; ρ: density; p: pressure; I: identity matrix; μ: dynamic viscosity; $\langle v_{ACEO} \rangle$: time-averaged EO slip velocity

Electrostatics

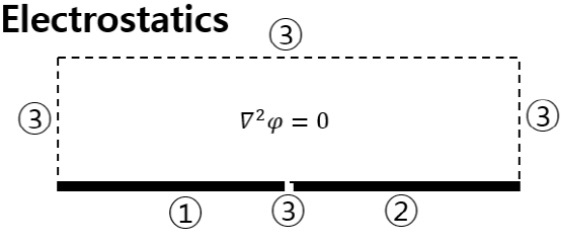

①:
$$\varphi = \frac{V_{pp,EO}}{2}\sin\omega_{EO}t + \frac{V_{pp,DEP}}{2}\sin\omega_{DEP}t$$
②:
$$\varphi = \frac{V_{pp,EO}}{2}\sin(\omega_{EO}t + \pi) + \frac{V_{pp,DEP}}{2}\sin(\omega_{DEP}t + \pi)$$
③:
$$\frac{\partial\varphi}{\partial n} = 0$$

Laminar flow

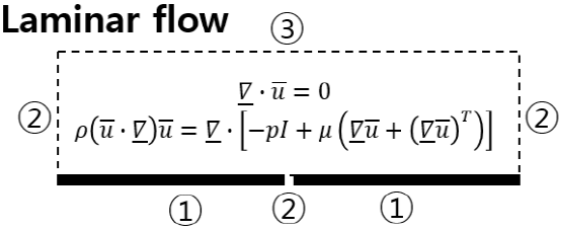

①: $\overline{u} = \langle v_{ACEO} \rangle \hat{\imath}$
②: $\overline{u} = 0$
③: $\overline{n}\cdot\left[-pI + \mu\left(\underline{\nabla}\overline{u} + (\underline{\nabla}\overline{u})^T\right)\right] = 0$

Figure 3-6. Problem formulation for the electrokinetic simulation.

Figure 3-7 shows the calculated net force fields for *E. coli* and PS beads using COMSOL Multiphysics® 4.3, and hydrodynamic drag, gravitational, buoyant, and DEP forces were considered for the force field calculation. The simulation was conducted for actual experimental geometry (Fig. 3-6), but close views around the electrodes were demonstrated here to show the differences between the treatments effectively. DEP (pDEP for bacteria and nDEP for beads) was effective within several microns from the electrode edges, and AC-EO dragged flows containing the particles to the electrode edges. The superimposed signal shows the integrated effect of DEP and EO for the enhanced selective concentration of the bacteria against beads.

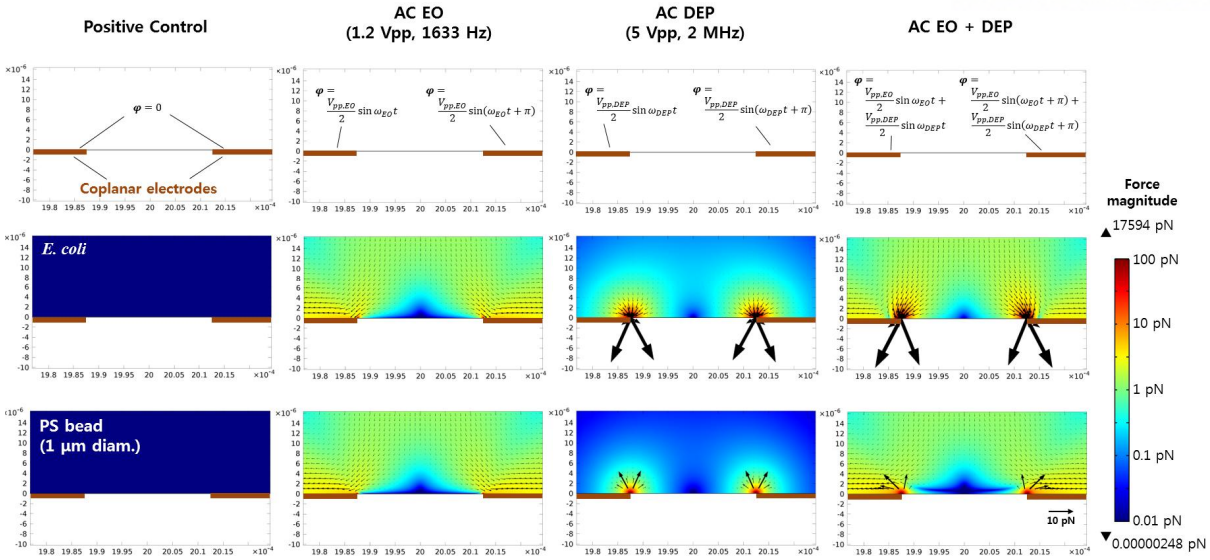

Figure 3-7. Calculated net force fields for *E. coli* and 1 μm-diam. PS beads that are initially at rest under different electrical treatments. Each surface plot represents the magnitude of the resultant forces exerted on the particles, and the black arrows show the force vectors.

The purity of the concentrated bacteria against the beads, i.e., the separation efficiency, was kept more than 99%, where the separation efficiency was defined as the fraction of target particles with respect to all of the particles (target + non-target). High separation efficiencies (over 90%) by DEP for bacterial capture were previously reported using applied voltages of more than 20 Vpp and long electrical activation times (10 min–1 h) (Cheng *et al.* 2009; Kim Soh 2009; Elitas *et al.* 2014). The superimposed signals enhanced the bacterial capture more selectively (>99 %) and more rapidly (30 s) with a low electric potential of DEP (5 Vpp) and simultaneous use of EO (1.2 Vpp).

Figures 3-5c and 3-5d show the quantities of MS2 viruses and cTnI-Ab, respectively, that were collected after applying the different types of signals for 1 min. Although nanometer-sized particles such as viruses and proteins are known to be difficult to manipulate by using DEP due to their small sizes, several studies have demonstrated the successful use of DEP for these particles (Nakano Ros 2013; Dash Mohanty 2014). In those studies, long exposure times (5–30 min) (Green *et al.* 1997; Hughes Morgan 1997; Maruyama *et al.* 2011) or nanoscale electrode gaps (30–500 nm) (Madiyar *et al.* 2013; Hoelzel *et al.* 2005; Liao Chou 2012) under applied voltages of 5–35 Vpp were applied to increase the electric field for capture. It was observed in the present study that significantly more MS2 and cTnI-Ab were captured using the superimposed signals than either DEP (10 Vpp) or EO (2 Vpp) signals alone ($p < 0.035$), with a gap of 25 μm between two electrodes and short electric field exposure time (1 min). The electric field gradient in the present electrodes was not high, compared to the previous DEP studies; however, many of the nanoparticles in the present study were continuously moved to the electrode edges by AC EO, providing those nanoparticles with the chances to be affected by the DEP forces. That is,

applying AC EO corresponded to increasing virus concentration near the electrodes. This was made possible by controlling the voltages and frequencies of DEP and EO separately, thereby precluding electrolysis as well as increasing the electric field intensity for capture.

3.4. Conclusions

Rapid and selective electrokinetic concentration has been demonstrated of bacteria, viruses, and proteins on two coplanar electrodes via superimposition of AC EO with DEP. The superimposed signals moved the particles distant from the electrodes toward the high electric field area with EO irrespective of the particle size, and then captured the particles selectively at a particular position, i.e., the highest electric field spot, against the flow with pDEP. Significantly more bacteria were captured using the superimposed signals than were collected using the other two treatments, EO and DEP. Moreover, the bacteria were selectively and rapidly concentrated with high purity against polystyrene beads from the mixture. The concentrations of collected nanometer-sized biological particles such as MS2 viruses and cTnI-Ab proteins were also enhanced by using this superimposition (EO + DEP) technique. This technique allowed for a relatively large gap between two electrodes and short electric field exposure time, and high capture efficiency. I strongly believe that the superimposition of AC EO and DEP can be applied to many biosensors requiring the rapid detection of biological particles with simple coplanar electrodes (Gong 2010; Sharma *et al.* 2016).

Chapter 4. Integrated Microfluidic System of EHD Focusing, DEP Concentration, and Electrical Detection of Bacteria

(Note: This chapter is partially or totally adapted from the published journal paper of myself, Han and Jang 2020.)

4.1. Materials and Methods

4.1.1 Numerical Analysis

3D simulations were conducted using the commercial software COMSOL Multiphysics® 4.3 to verify EHD focusing. A 4 mm long (x-), 200 μm wide (y-), and 49 μm high (z-) microchannel was designed with different electrode patterns on the bottom surface. All the boundary conditions used for the electric and flow fields are shown in Fig. S-5. The Laplace equation $\nabla^2\varphi = 0$ was first solved to find the quasi-static electric field, where φ is electric potential. The conjugate gradient method was used as an iterative solver for φ along the entire domain. The electric field vector fields were obtained from $\overline{E} = -\underline{\nabla}\varphi$. The governing equations for the flow fields were $\underline{\nabla} \cdot \overline{u} = 0$ and $\underline{\nabla} \cdot \left[-pI + \mu\left(\underline{\nabla}\overline{u} + \left(\underline{\nabla}\overline{u}\right)^{\mathrm{T}}\right)\right] = 0$, where $\overline{u}$ is the flow velocity vector, p is static pressure, and μ is the dynamic viscosity of the fluid. The EO slip flow (boundary conditions ⑥-(a) and ⑥-(b) in Fig. S-5) at the focusing electrodes is expressed as $\langle U_{EO}\rangle = \frac{\Lambda\varepsilon_m{\varphi_0}^2\Omega^2}{8\mu y(1+\Omega^2)^2}$, where $\Lambda = \frac{C_S}{C_S+C_D} \cong 0.5$ (C_S and C_D are Stern and diffuse layer capacitances, respectively)[2], ε_m is the electrical permeability of the medium (fluid), φ_0 is the initial potential, and Ω is a non-dimensional frequency defined as $\Omega = \frac{\Lambda\pi\varepsilon_m\omega}{2\sigma_m\lambda_D}$ with angular frequency ω, electrical conductivity of medium σ_m, and Debye length λ_D. Here, the y coordinate is equal to zero at the center of the focusing electrode gap. The Newton–Raphson algorithm was employed along with an iterative solver using the generalized minimum residual method; hence, the $\overline{u}$ and p fields were obtained along the volumetric domain.

Particle tracing was conducted for the bead using the Lagrangian discrete phase model equation $m_p\frac{d^2\overline{x}_p}{dt^2} = \overline{F}_{drag} + \overline{F}_{gravity} + \overline{F}_{buoyancy} + \overline{F}_{DEP} = -3\pi\mu d_p\left(\frac{d\overline{x}_p}{dt} - \overline{u}\right) + m_p\frac{\rho_p-\rho}{\rho_p}\overline{g} + \frac{\pi}{4}{d_p}^3\varepsilon_m Re(K)\underline{\nabla}\left|\overline{E}\right|^2$, where m_p is the particle mass, $\overline{x}_p$ is the position vector of the particle, d_p is the particle diameter, ρ_p is the particle density, $\overline{g}$ is the gravity vector, ε_m is the electrical permittivity of the medium, and $Re(K)$ is the real part of the Clausius–Mossotti factor. Here, the beads were 380-nm-diameter spheres, with ρ_p of 1050 kg/m^3. Predetermined $\overline{u}$ and $\overline{E}$ values were used for particle

tracing, and a transient implicit-solver-generalized alpha was used with automatically chosen time steps. A total of 114 (19×6) particles were thus uniformly distributed at the inlet, and their position vectors were calculated with time. All the solutions numerically converged when the mesh exceeded 789,653 elements, and the 4th, 2nd, and 1st order elements were used for the electric potential, flow velocity, and pressure, respectively (with 4, 10, 20, and 35 nodes per tetrahedral element for the 1st, 2nd, 3rd, and 4th order elements respectively). The trajectories of the beads (Fig. 4-7c) were then obtained with zero electric potentials at the concentration electrodes.

4.1.2 Preparation of bead and bacteria solutions

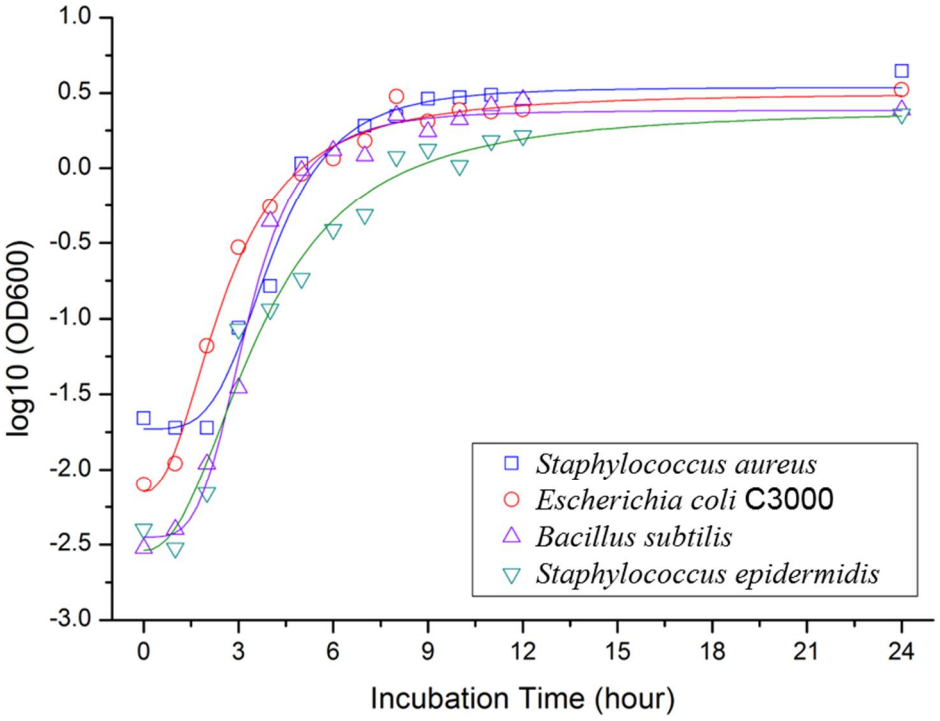

Figure 4-1. Bacterial growth curves measured for the present study.

Bacterial strains *S. aureus* (ATCC® 25923™), *B. subtilis* (ATCC® 21332™), *E. coli* C3000 (ATCC® 15597™), and *S. epidermidis* (ATCC® 12228™) were cultured on Luria–Bertani (LB) agar plates separately for 24 h at 37 °C. Each colony was then inoculated into 10 mL of LB broth (244620; Becton, Dickinson and Company, USA) and grown at 37 °C and 160 rpm in a shaking incubator for 4–6 h according to the late-log-phase growth condition (Fig. 4-1), which was determined by measuring optical density at 600 nm. The grown bacteria were diluted serially and centrifuged at 4000

rpm for 10 min to remove the residual LB broth. A 0.01× solution of PBS [100-fold diluted PBS (pH 7.4; Gibco™ 10010023; Thermo Scientific, USA) in deionized water (18.2 MΩ·cm; from university-provided water pipelines)] was used as the medium to simulate drinking water; the electrical properties (conductivity, Debye length, etc.) of the 0.01× PBS and drinking water were similar. The label-free bacteria were re-suspended in the prepared media.

For the particle capture experiments with beads and bacteria, 380-nm-diameter red (excitation/emission: 542/612 nm) fluorescent polystyrene beads (Fluoro-Max R400; Thermo Scientific, USA) were suspended in 0.001× PBS buffer to obtain a number density of 5×10^5 #/mL. The *S. aureus* and *E. coli* C3000 in 0.01× PBS solution were also labeled separately with SYTO™ 9 (S34854; Thermo Scientific, USA) (excitation/emission: 483/503 nm) (2.5 μM) at concentrations of 10^7 CFU/mL (Lapizco-Encinas *et al.* 2004). The electrical conductivity was measured using a conductivity meter (handylab pH/LF 12; SI Analytics GmbH, Germany), and these values were 200 μS/cm and 21 μS/cm for 0.01× PBS and 0.001× PBS, respectively, at room temperature.

4.1.3 Device microfabrication and surface modification

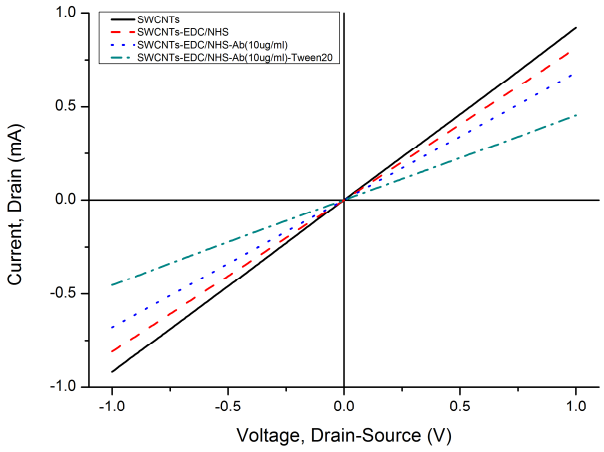

Figure 4-2. *I-V* graphs for the detection electrodes with SWCNT channels modified with EDC/NHS, *S. aureus* antibody, and Tween20.

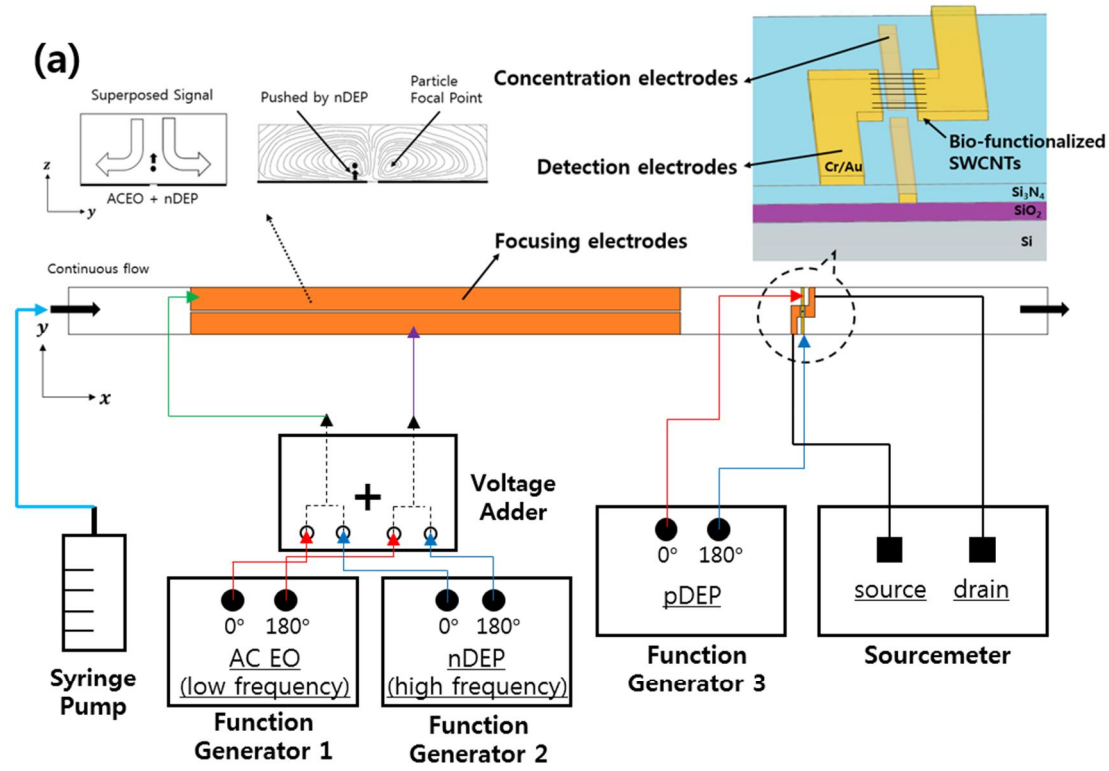

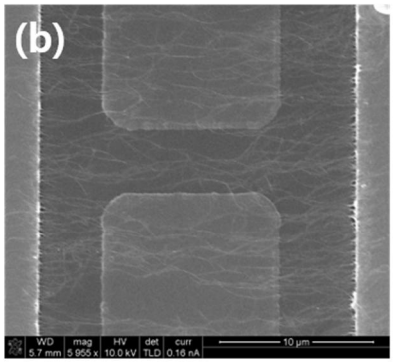

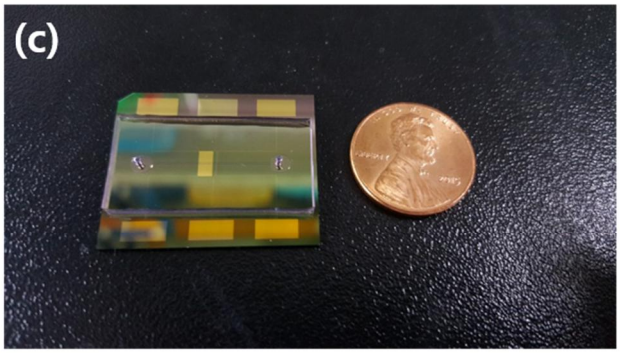

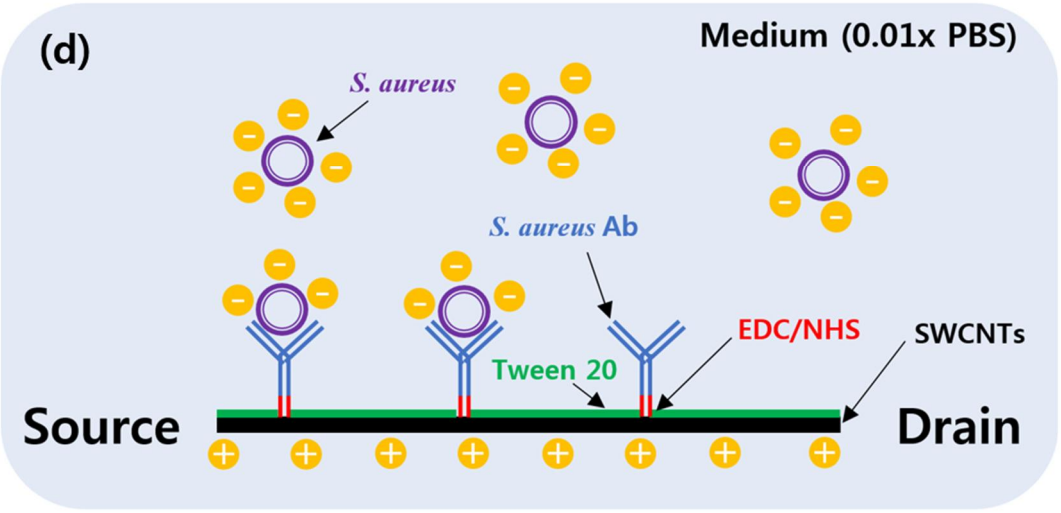

Figure 4-3. (a) Device configuration and experimental set-up with three pairs of electrodes: focusing, concentration, and detection electrodes. (b) Field-emission scanning electron microscope image showing deposition of high-density aligned single-walled carbon nanotubes (SWCNTs) between the detection electrodes via alternating current dielectrophoresis (DEP). (c) Image of the fabricated device. (d) Functionalization scheme of the FET immunosensor and illustration of the FET by the capture of negatively charged *S. aureus*. The binding of the negatively charged bacteria onto the bio-functionalized SWCNTs induces holes in the p-type semiconductor, resulting in the increase of electrical currents.

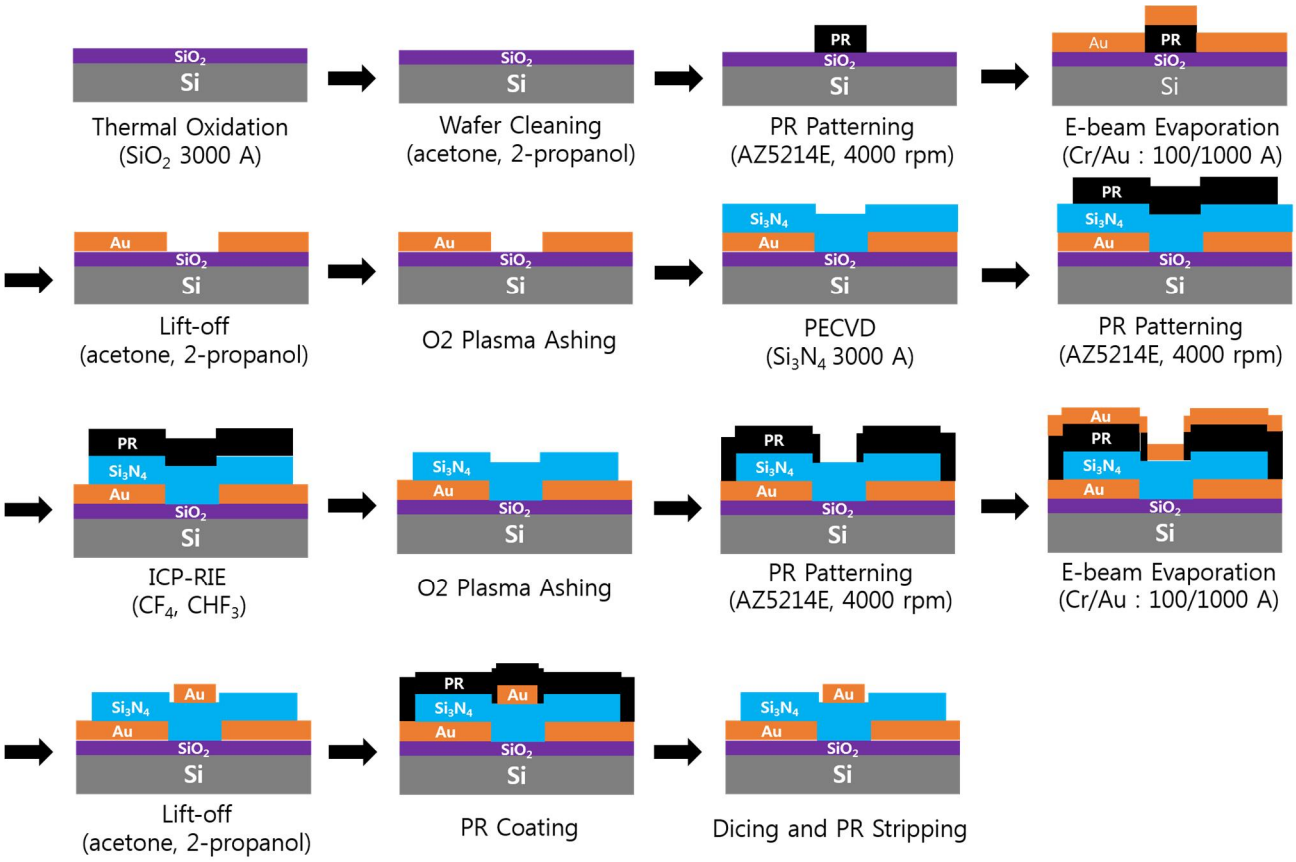

Figure 4-4. Microfabrication process of the microfluidic immunosensor chip.

A 6-inch SiO_2/Si wafer was pre-cleaned by ultra-sonication in acetone and isopropyl alcohol for 5 min each. A pair of Cr/Au coplanar rectangular concentration electrodes (thickness: 10/100 nm) were deposited on the wafer. A 300-nm-thick dielectric Si_3N_4 layer was fabricated on the concentration electrodes using plasma enhanced chemical vapor deposition. The dielectric layer was then etched, and the residual photoresists were removed with oxygen plasma. The focusing and detection electrodes (Cr/Au thickness: 10/100 nm, respectively) were deposited using electron beam

evaporation, and the wafer was diced into chips of 35 mm × 25 mm (Fig. 4-4). The embedded concentration electrodes (gap: 5 μm) and two source and drain electrodes (gap: 20 μm; width: 50 μm) were used for the pDEP capturing and conductance measurements, respectively.

The SWCNT channels were prepared between the detection electrodes and functionalized as described in a previous work6. Briefly, SWCNT powders (98% semiconducting) were suspended in N,N-Dimethylformamide (DMF; 3057-4405; Daejung chemicals, Korea) through ultra-sonication and centrifugation (concentration: 10 μg/mL). Then, 5 μL of the prepared SWCNT suspension was applied between the two detection electrodes, and aligned SWCNT bridges were formed by applying DEP at 5 Vpp and 200 kHz for 30–60 s (Fig. 4-3b). Polyclonal anti-*S. aureus* (ab20920, Abcam, UK) in 1× PBS (concentration: 10 μg/mL) was then immobilized on the SWCNTs by incubation at 37 °C for 2 h via EDC(1-Ethyl-3-(3-dimethylaminopropyl)carbodiimide)-NHS (N-Hydroxysuccinimide) chemistry. SuperBlock T20 blocking buffer (0.05% Tween-20; 37536, Thermo Scientific, USA) was incubated for 30 min at room temperature to prevent non-specific attachment to the SWCNTs (Mao *et al.* 2013) (Fig. 4-3d). All the surface modifications were performed through a polydimethylsiloxane (PDMS) well around the SWCNTs, and the sensors were rinsed with 1× PBS and dried after each modification step. The current–voltage (I-V) curves were measured after each modification step (Fig. 4-2). All the bio-functionalized sensors were stored at 4 °C before further use to maintain stability (Lin *et al.* 2014).

4.1.4 Experimental set-up

PDMS microchannels (width/height: 200 μm/49 μm) with two 1-mm-diameter holes at the inlet and outlet reservoirs were manufactured as described in a previous work (Han *et al.* 2019) and bonded onto the bio-functionalized sensor chips by aligning manually with a microscope (Fig. 4-3c). A syringe pump (Harvard Pump 11 Elite, 70-4505INT; Harvard Apparatus, USA) was used to infuse the prepared beads or bacterial solution into the prepared microfluidic device. External AC voltages were applied to the contact pads.

For the bead capture experiments, a lab-made voltage adder was used to superimpose signals from two function generators (AFG3022C; Tektronix, USA) (Han *et al.* 2018). The superimposed signals were applied to the focusing electrodes to activate EO vortices (1.25 Vpp, 5.4 kHz) and nDEP pushing (10 Vpp, 3 MHz) to align the particles along the stagnant lines (Fig. 4-3a). Another function generator (WW5064; Tabor, Israel) was used for the pDEP capture (10 Vpp, 200 kHz) of beads on the SWCNT channels. Here, each function generator offered sinusoidal signals that were 180° out of phase via the two-channel sources. A cooled interline transfer camera (ORCA-R2; Hamamatsu, Japan) connected to an inverted fluorescent microscope (Eclipse Ti-U; Nikon, Japan) was used to obtain images at an exposure time of 100 ms. The number of beads captured in a specified area (20×50 μm^2)

between the two detection electrodes was counted with ImageJ by dividing the total area occupied by the particles by the area occupied by a single bead in the fluorescence images (Yang *et al.* 2006; Han *et al.* 2018).

For the bacterial quantification experiments, EHD focusing (1.5 Vpp, 9 kHz) and concentration (10 Vpp, 8 MHz) electrodes were biased for 10 min, and the RCC of the SWCNTs was measured throughout the experiments via the detection electrodes using a source meter (2635B; Keithley Instruments, USA) at a fixed source–drain voltage of 100 mV. The RCC was computed as $(G–G_0)/G_0$, where G is the electrical conductance measured in real-time and G_0 is the equilibrated electrical conductance measured under steady flow before the actuation of AC signals. The stabilized RCC (SRC) was also computed as $(G_S–G_0)/G_0$, where G_S is the stabilized electrical conductance measured after the 10-min-bacterial attachment (Wasik *et al.* 2018).

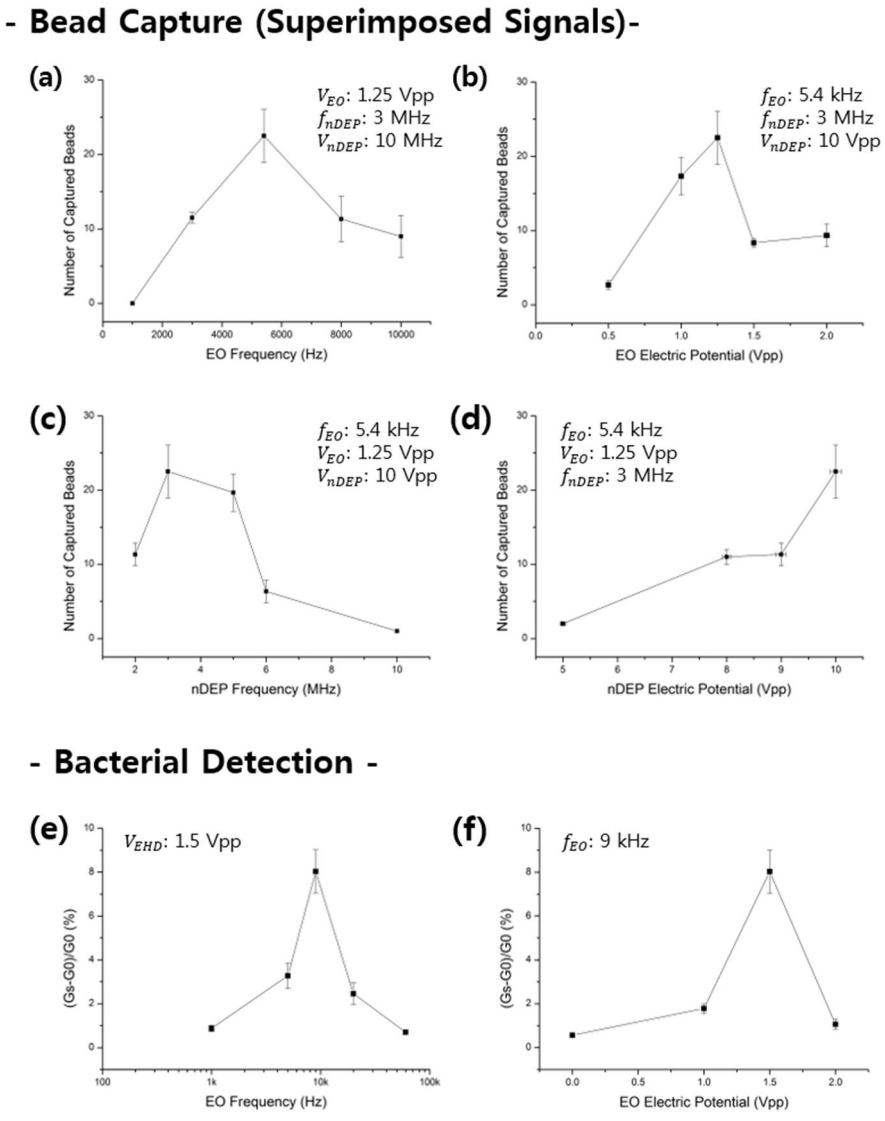

Figure 4-5. Optimization process of the frequencies and electric potentials for EHD focusing. Among the four electrical components of the superimposed signals for bead capture, one parameter, namely **(a)** EO frequency, **(b)** EO electric potential, **(c)** negative DEP (nDEP) frequency, and **(d)** nDEP electric potential, was varied while the other three parameters were fixed. Between the two components of the sinusoidal signals for bacterial detection, one parameter, namely **(e)** EO frequency or **(f)** EO electric potential, was varied while the other parameter was fixed.

The optimization process for the voltages and frequencies of EHD focusing in these two experiments was conducted. Alternating current (AC) frequencies and electric potentials were experimentally determined for electrohydrodynamic (EHD) focusing. Four parameters were investigated in the bead capture experiments, namely electro-osmosis (EO) frequency, EO electric potential, negative dielectrophoresis (nDEP) frequency, and nDEP electric potential. The number of captured beads (i.e., 380-nm-diameter polystyrene beads) was compared with the DEP fixed at the concentration electrodes, where one parameter among the aforementioned four parameters was varied while the other three were fixed. Figure 4-5a shows the number of captured beads with varying EO frequency, showing that the peak value was 5.4 kHz. The maximal capture occurred at an EO potential of 1.25 Vpp. A larger convection speed could be induced when the EO potential was higher, but the risk of particle loss by inertial impaction could also increase (Fig. 4-5b). A frequency of 3 MHz was deemed best for the nDEP frequency (Fig. 4-5c). Although stronger nDEP forces were generated with this higher frequency in the megahertz regime, the superimposed signals were unstable when the nDEP frequency exceeded 3 MHz owing to the lab-made voltage adder limitations. Figure 4-5d shows that the nDEP electric potential in this case was determined as 10 Vpp, which was the maximal output voltage from the function generator.

For bacterial detection experiments, a pair of sinusoidal signals were used for EHD focusing. Only two parameters were investigated, i.e., EHD frequency and EHD electric potential, and one parameter was varied while the other was fixed. Then, the relative electrical conductance change (RCC) between the detection electrodes were compared. Here, the DEP (8 MHz, 10 Vpp) was applied to the concentration electrodes. Figure 4-5e shows the stabilized relative electrical conductance change (SRC) was the highest at 9 kHz. The SRC was also the highest at an EHD potential of 1.5 Vpp when the frequency was fixed at 9 kHz (Fig. 4-6f).

The frequencies for DEP concentration were determined according to the Clausius–Mossotti (CM) factors under a maximal voltage output of 10 Vpp (peak-to-peak). Each experiment in this study was performed at least thrice, and the mean values are shown with their standard deviations indicated as error bars.

4.2. Results and Discussion

4.2.1 Enhanced DEP capture of nanometer-sized beads aided by EHD focusing

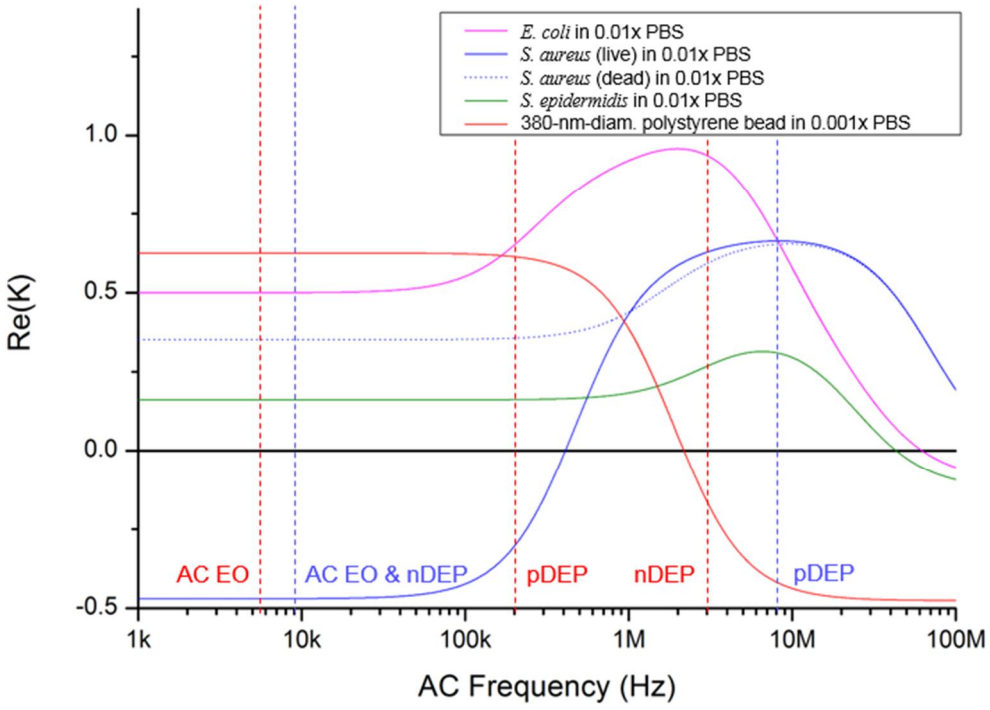

Figure 4-6. Clausius–Mossotti factors of selected bacteria and a bead. They are functions of electrical permittivities and conductivities of media and particles, where all of wall, membrane, and cytoplasm were considered in the calculation in case of bacteria. The dielectric property of *B. subtilis* is unknown. Red and blue vertical dashed lines indicate the AC frequencies for the beads and *S. aureus* experiments, respectively.

Figure 4-3 shows a schematic of the designed microfluidic immunosensor consisting of three pairs of coplanar electrodes: focusing (10 μm gap), concentration (5 μm gap), and detection (20 μm gap) electrodes with experimental set-up. The focusing electrodes were designed for EHD focusing of the particles based on the AC EO vortex with nDEP on the y-z plane during continuous transport in the streamwise (x) direction. This means that stagnant particle focal points were formed inside the AC EO vortices while being pushed by the nDEP; thus, the incoming particles were confined around the focal points. As these points were located close on the bottom surface as well as close to the center of

the CNT channel in the streamwise direction, they were effectively captured using the concentration electrodes via pDEP. The real parts of the CM factors for the beads were found to determine their DEP behaviors, and were 0.63 (at 5.4 kHz), 0.61 (at 200 kHz), and -0.16 (at 3 MHz) (Fig. 4-6) (Park *et al.* 2011).

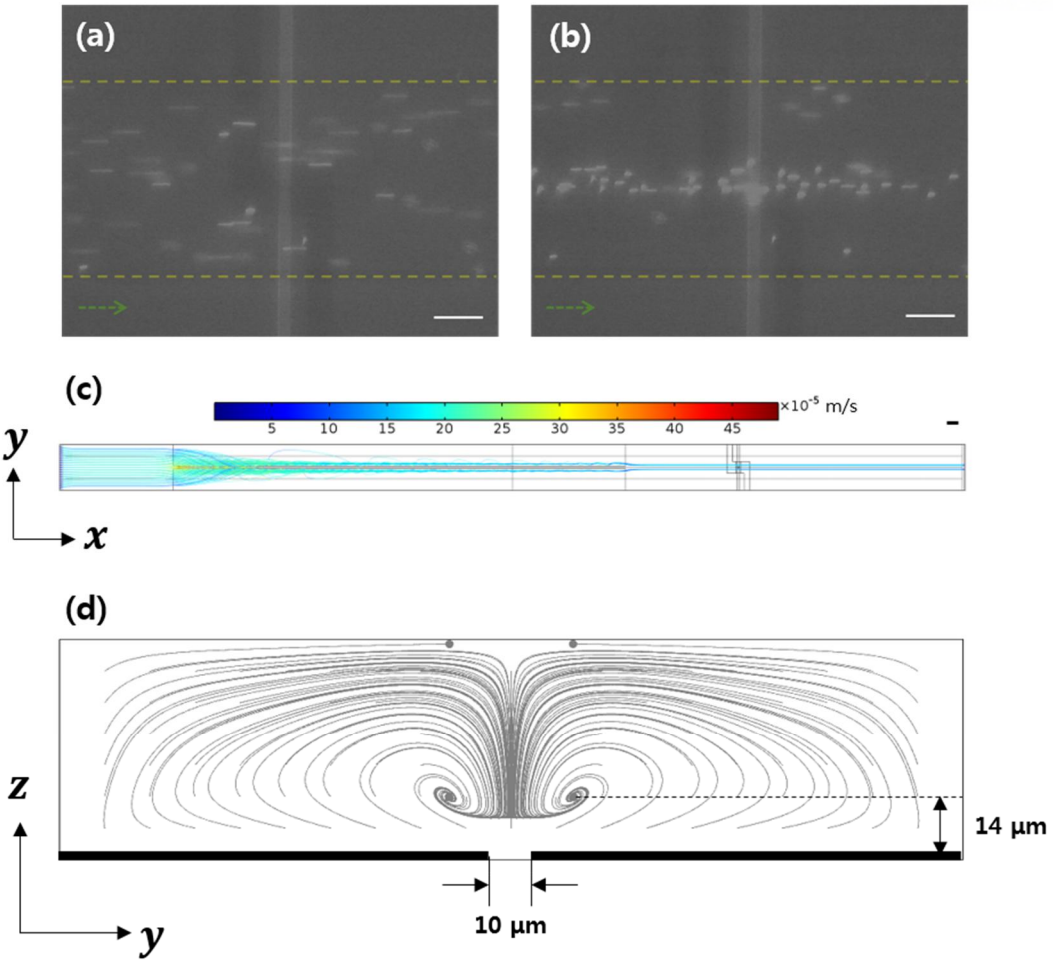

Figure 4-7. Fluorescence images of 380-nm-diameter polystyrene beads flowing over the detection electrodes **(a)** without and **(b)** with EHD focusing (1500 Hz, 1 Vpp) at a flow rate of 83.3 nL/min and number concentration of 1×10^7 #/mL. The yellow dashed lines and green arrows indicate the side walls of the microchannels and the flow direction, respectively. Calculated trajectories of the 380-nm-diameter beads with EHD focusing; **(c)** top view where the color represents the speeds of the beads, and **(d)** cross-sectional view at the detection area where the black bold lines on the bottom show the focusing electrodes. **(e)** Beads captured between the detection electrodes after biasing the focusing and detection electrodes with different electrical signals, for a flow rate of 200 nL/min. **(f)** Number of beads captured in an area (20×50 μm^2) between the two detection electrodes after biasing with different electrical signals for 5 min. **(g)** Measured number of captured beads for 1 min and capture efficiencies with different flow rates at a fixed number concentration of 5×10^5 #/mL. The white and black scale bars in **(a)-(c)** and **(e)** represent 50 μm.

It was observed that EHD focusing of the 380-nm-diameter beads was not easy to accomplish by the AC EO signal alone. Both AC EO vortices and weak pDEP attachment onto the focusing electrodes occurred at a frequency of 5.4 kHz. Hence, another nDEP signal (3 MHz) was superimposed on the AC EO signals, and the superimposed signals having both low (AC EO) and high (nDEP) frequency components were applied to the focusing electrodes. Successful particle focusing using the superimposed signals were then demonstrated experimentally (Figs. 4-7a-b) and numerically (Figs. 4-7c-d). The fluorescence images were obtained over the detection electrodes, and computer simulations were obtained with Comsol Multiphysics software (please see supplementary information). The beads were delivered to the DEP-effective region close to the concentration electrodes with minimal losses. The number of beads observed on the detection area were 14.6 times greater than those without EHD focusing, and no beads were captured without DEP concentration (Figs. 4-7e-f).

Both the number of captured beads and the corresponding capture efficiencies were analyzed (Fig. 4-7g) with respect to the flow rate, and the efficiency is defined as the number of beads captured in the detection area divided by the number of incoming beads. The beads were most captured at a flow rate of 200 nL/min (at an incoming number rate of 100 #/min) and a flow velocity of 340 μm/s. At this condition, the capture efficiency was approximately 23%. This is in contrast with an efficiency of ~0.1% for the electrode-deposited cantilever sensors in a microfluidic device (Leahy Lai 2017b), and efficiencies for electrokinetic capture on a narrow detection area have been rarely reported.

4.2.2 Quantification of bacteria via focusing-concentration-detection

The I-V curves measured after each functionalization step of the sensors showed ohmic contacts between the SWCNTs and detection electrodes (Fig. 4-2). For the biosensing of *S. aureus* in the microfluidic device, *S. aureus* particles were focused by the AC EO and nDEP, both of which simultaneously occurred at the same low frequency (9 kHz) (Fig. 4-6), and the confined bacteria were delivered to the DEP-effective region above the concentration electrodes and captured by pDEP (8 MHz) on the SWCNTs.

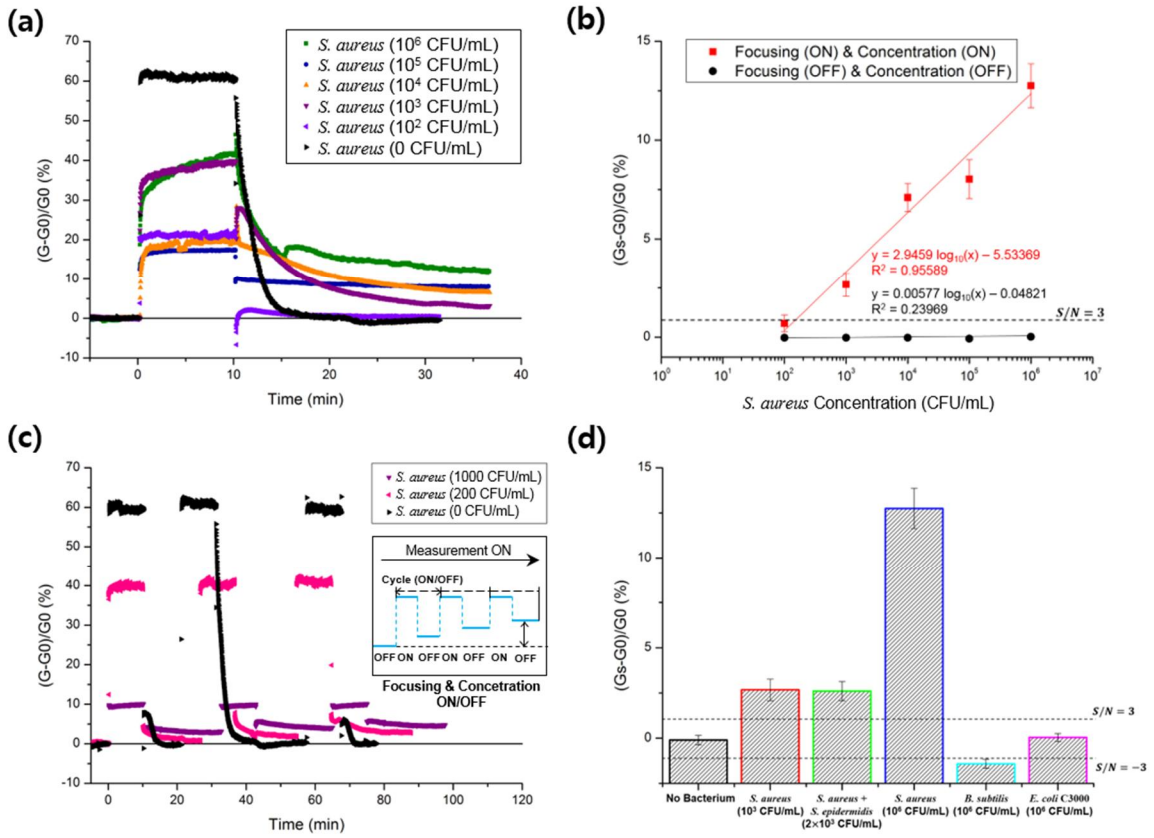

Figure 4-8. **(a)** Measurement of the relative electrical conductance change of SWCNTs with different *S. aureus* concentrations. **(b)** Stabilized relative electrical conductance change (SRC) as a function of *S. aureus* concentrations. **(c)** Continuous monitoring of *S. aureus* at different bacterial concentrations (0, 200, and 1000 CFU/mL) for three repeated cycles where each cycle consists of turning on both EHD focusing and DEP concentration for 10 min and then turning off while measuring the RCC throughout the cycle. **(d)** Selectivity tests against *S. epidermidis*, *B. subtilis*, and *E. coli* C3000. S/N refers to the signal-to-noise ratio.

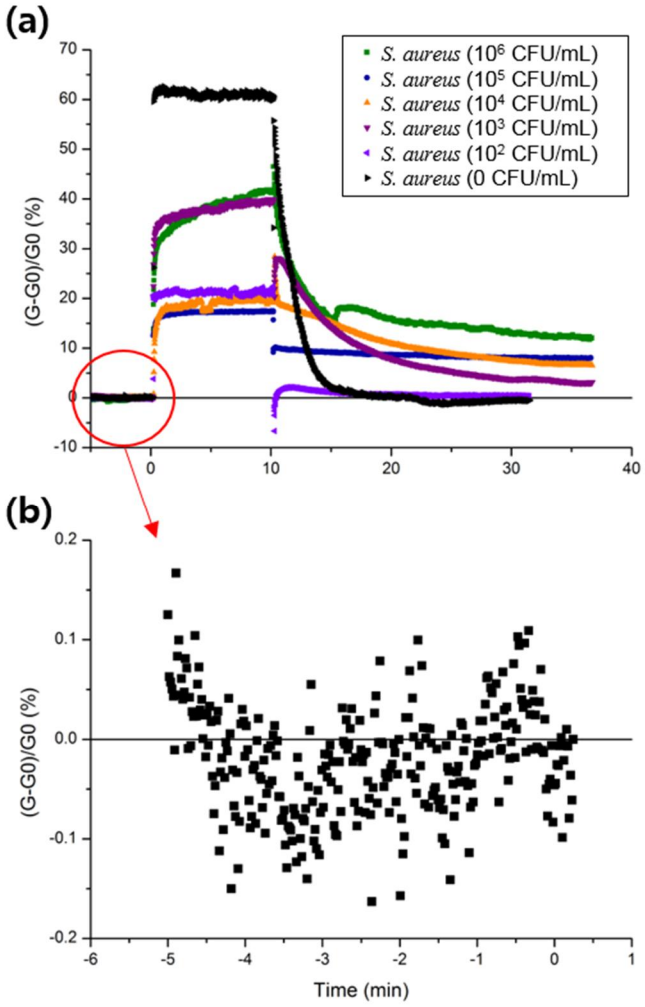

Figure 4-9. (a) Figure 5-8a; **(b)** example showing electrical conductance variations with time.

Figure 5a shows real-time measurements of *S. aureus* with different bacterial concentrations (from 10^2 to 10^6 CFU/mL) at the inlet. Before biasing the focusing and concentration electrodes, i.e. less than 0 min in Fig. 5-8a, the conductance variation was very small with a standard deviation (or noise) of 0.27% (Fig. 4-9). The RCC owing to the captured bacteria was measured after turning off both the biases at 10 min for all bacterial concentrations, and the RCC was stabilized around 35 min. The SRC increased with increasing bacterial concentrations (Fig. 4-8b). That is, bacterial capture induced increases in the electrical conductance through the SWCNTs. In fact, as the surface of bacteria is negatively charged in the 0.01× PBS buffer, the binding of the negatively charged bacteria onto the bio-functionalized SWCNTs induces holes in the p-type semiconductor, resulting in the increase of electrical currents at the fixed source–drain voltages (Jiang *et al.* 2004; Wu *et al.* 2017). The conductance signals measured during the first 10 min bias from 0 min, which was for focusing

and bacterial capture, was caused by interference with the electric field of the concentration electrodes.

Figure 4-8b shows the calibration plot of the microfluidic immunosensor with respect to the *S. aureus* concentrations. The linear relationship (R^2=95.6%) between the SRCs and the logarithmic *S. aureus* concentrations was maintained in a range of 200 to 10^6 CFU/mL. This linearity did not continue when the bacterial concentration was around 10^7 CFU/mL, possibly because of attachment of too many bacteria beyond the capability of the bio-receptors on the SWCNTs. Interestingly, this characteristic was also reported in DEP-enhanced surface plasmon resonance sensors (Galvan *et al.* 2018). The limit of detection (LOD) of the present immunosensor was calculated to be 150 CFU/mL based on the three signal-to-noise (S/N) ratio (3-sigma). The SRCs were smaller than the 3-sigma when both the focusing and concentration were not turned on. Further, the measured relative standard deviation for 10^4 CFU/mL was 10.0%. The measurement of bacteria with a wide dynamic range (200 to 10^6 CFU/mL) and improved LOD was rendered possible owing to the serial enrichment operation of EHD focusing and DEP concentration, and sensitive detection through the functionalized SWCNTs.

Figure 4-8c shows continuous measurements of *S. aureus* at different bacterial concentrations (0, 200, and 1000 CFU/mL) at the inlet during three repeated cycles; each cycle consists of turning on the EHD focusing and DEP concentration for 10 min and then turning off while measuring the RCC throughout the cycle. The measured values of SRC were -0.32%, 0.21%, and 0.07% at 0 CFU/mL, 0.78%, 1.84%, and 2.82% at 200 CFU/mL, and 3.05%, 4.05%, and 4.68% at 1000 CFU/mL. The SRCs increased with the number of cycles at 200 and 1000 CFU/mL. That is, *S. aureus* in the solution was continuously captured with the number of cycles until the bio-functionalized SWCNTs were spatially filled with the bacteria.

Figure 4-8d shows the selectivity test against a mixture of *S. aureus* and *S. epidermidis*, *E. coli* C3000, and *B. subtilis*. A bacterial mixture (2×10^3 CFU/mL, 1:1 ratio) of *S. aureus* and *S. epidermidis* showed SRCs similar to that of pure *S. aureus* (10^3 CFU/mL). Each of *B. subtilis* (10^6 CFU/mL) and *E. coli* C3000 (10^6 CFU/mL) showed SRCs smaller than the 3-sigma. Most incoming *E. coli* and *S. epidermidis* were possibly attached to the focusing electrodes by pDEP with 9 kHz signals, whereas much less losses of *S. aureus* occurred by nDEP during focusing (Fig. 3) (Asami *et al.* 1980; Johari *et al.* 2003; Sanchis *et al.* 2007).

4.2.3 Additional sensor selectivity based on antigen–antibody affinity

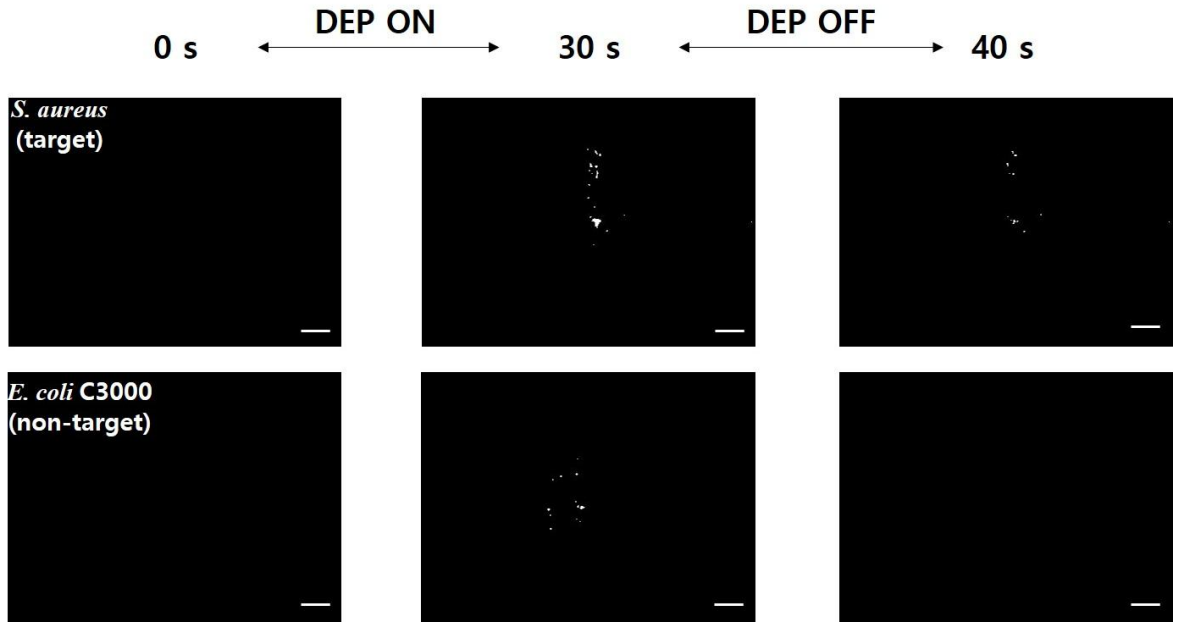

Figure 4-10. Fluorescence images of *S. aureus* (target) and *E. coli* C3000 (non-target) when the concentration electrodes (10 Vpp, 8 MHz) alone were activated and then deactivated. Each bacterial sample was of concentration 10^7 CFU/mL, and the scale bars represent 50 μm. When the electrodes were deactivated, most of the captured target (*S. aureus*) were still bound on the SWCNTs, whereas all the captured non-target (*E. coli* C3000) flowed away without non-specific binding.

Although the present EHD focusing can offer a great amount of selectivity to the sensors if the dielectrophoretic properties, such as the CM factors, of the bacteria to be quantified are known, this may not work if a mixture of two or more bacteria show similar dielectrophoretic behaviors. For example, although the optimal frequency for capture of *S. aureus* (target) is 8 MHz (Fig. 4-6), this frequency is also good for capturing *E. coli* C3000 (non-target), which is a risky factor to increase the non-specific binding of non-target bacteria on the bio-receptors. Therefore, I tested whether the present microfluidic immunosensor can prevent non-specific binding owing to pDEP in case where the electrokinetic separation of bacteria does not work sufficiently because of similar dielectrophoretic characteristics. In this regard, I turned off the EHD focusing in the experiment.

Both *S. aureus* and *E. coli* C3000 were captured on the SWCNTs coated with *S. aureus* antibodies when the concentration electrodes (10 Vpp, 8 MHz) alone were activated (Fig. 4-10), where an upright fluorescent microscope (Eclipse 80i; Nikon, Japan) with a CCD camera (CoolSNAP^{TM} DYNO; photometrics®, USA) was used to obtain images and videos with an exposure

time of 200 ms. When the electrodes were deactivated, most of the captured *S. aureus* were still bound on the SWCNTs, whereas all the captured *E. coli* C3000 flowed away without non-specific binding (see supplementary video). The pDEP can usually increase non-specific binding of particles on the surface, but this was prevented owing to the blocking buffer treatment (SuperBlock T20) and continuous channel flow. Few studies on avoiding electrokinetics-related non-specific binding have been reported; harsh electrothermal fluid motion was intentionally induced to remove non-specific binding in an assay (Liu *et al.* 2014), or blocking agent and secondary antibody amplification were treated after the DEP capture of different bacteria (Galvan *et al.* 2018). This FET immunosensor thus enabled an increase in sensitivity due to EHD focusing and pDEP concentration while maintaining a high level of selectivity against various non-target microorganisms, and high selectivity and low cross reactivity is highly required to address fundamental challenges in FET-based biosensors (Syedmoradi *et al.* 2019).

This electrokinetics-enhanced microfluidic sensor can be used for detection of several other target analytes unless medium conductivity is very high. The main parameters, AC frequency and media conductivity, can be adjusted for a particular target since both EO and nDEP should be generated for EHD focusing, and pDEP should be generated for concentration. For example, EO and nDEP occurred simultaneously at 9 kHz on the focusing electrodes for *S. aureus* detection in the present study; however, it may be difficult to avoid attachment to the electrodes during focusing in the case of *S. epidermidis* because pDEP can occur for this bacterium. In this case, an AC signal above 40 MHz can be superimposed with the 9 kHz (EO+pDEP) signal to generate a stronger nDEP, resulting in EO and nDEP, which was also observed when collecting 380-nm-diameter beads in this study.

4.2.4 Negligible electrothermal flow effect

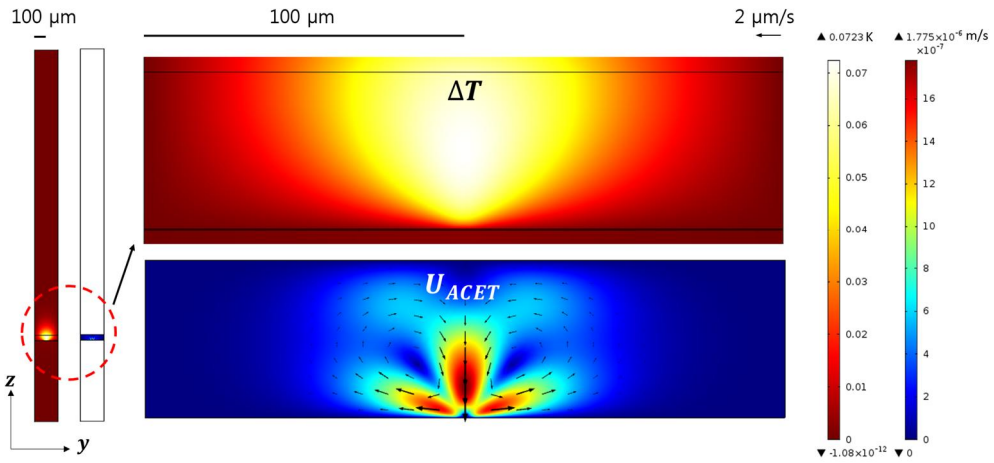

Figure 4-11. Computed temperature rises and electrothermal velocity magnitudes in 0.01× PBS (10 Vpp, 8 MHz) around the concentration electrodes.

2D simulations were conducted using the same software with the above 3D simulations to estimate the AC electrothermal effect in the experiments. A cross-sectional (y-z plane) domain was set at the concentration electrodes (5-μm-gap), with considering silicon substrate (675-μm-thick), SiO_2 layer (300-μm-thick), Si_3N_4 layer (300-μm-thick), 0.01x PBS; (49-μm-thick), and PDMS (2.4-mm-thick). Electric governing equation $\nabla^2\varphi = 0$ was solved for the all set domain with boundary conditions of $\frac{\partial\varphi}{\partial n}$ at the all outer boundaries and $\varphi = \frac{V_{pp,pDEP}}{2}\sin\omega_{pDEP}t$ and $\varphi = -\frac{V_{pp,pDEP}}{2}\sin\omega_{pDEP}t$ at each concentration electrodes, where $V_{pp,pDEP}$ and ω_{pDEP} is peak-to-peak voltage and angular frequency of AC signal for positive DEP, respectively. Thermal governing equation of $k\nabla^2 T + \frac{\sigma_m}{2}\left|\overline{E}\right|^2 = 0$ was solved for all of the set domain with boundary conditions of $T = 23$ ℃ at entire the outer boundaries, where k is thermal conductivity and T is temperature (Green *et al.* 2001; Loire *et al.* 2012). Flow governing equations of $\underline{\nabla}\cdot\overline{u} = 0$ and $\underline{\nabla}\cdot\left[-pI + \mu\left(\underline{\nabla}\overline{u} + \left(\underline{\nabla}\overline{u}\right)^{\mathrm{T}}\right)\right] + \overline{F}_{ACET} + \overline{F}_{bouyancy} = 0$ was solved for 0.01x PBS (0.02 S/m) domain only, with the boundary conditions of $\overline{u} = 0$. Here, $\overline{F}_{ACET} = \frac{\varepsilon_m}{2}\left[(c_\varepsilon - c_\sigma)\frac{\underline{\nabla}T\cdot\overline{E}}{1+(\omega_{pDEP}\varepsilon_m/\sigma_m)}\overline{E} - \frac{1}{2}c_\varepsilon\underline{\nabla}T\left|\overline{E}\right|^2\right]$ and $\overline{F}_{bouyancy} = -\rho_m(T - 23\ ℃)\beta\overline{g}$, where $c_\varepsilon \cong -0.004\ ℃^{-1}$, $c_\sigma \cong 0.02\ ℃^{-1}$, ρ_m is a density of media, $\beta \cong 0.001\ ℃^{-1}$, and $\overline{g}$ is gravity vector (Green *et al.* 2001; Loire *et al.* 2012). As results of calculations, the maximal possible temperature rise and flow velocity was 0.07 ℃ and 1.78 μm/s, respectively. The maximum temperature rises were calculated to be 0.68 ℃ and 6.24 ℃ in 0.1x PBS (0.186 S/m) and 1x PBS (1.59 S/m), respectively.

Chapter 5. Summary and Future Perspective

An array of IDEs is one of the most widely used planar electrodes in many DEP-based microfluidic devices; however, IDEs often show inefficiencies in DEP particle manipulation owing to the limited DEP-effective region. Herein, a MED method was presented that can generate planar electrode patterns with enhanced electric fields by simple electrode discretization and reconstructions. A novel objective function, factor **S**, was presented as well calculated on the electrode surface that enables 2D computation of the downward dielectrophoretic forces or $\partial\left|\overline{E}\right|^2/\partial z$ for the overall volumetric domain. The MED-optimized electrodes were determined based on the value of factor **S,** and as the factor **S** increased, the particle capture increased (Figs. 6a and 6b). The MED-optimized electrodes captured 1.4 to 35.8 times more bacteria ($p < 0.0016$) than the respective IDEs, with a bacterial purity against the beads of more than 99.8%. In this study, values of factor **S** were computed for the discretized electrodes generated from IDEs for comparison; however, this method can be applied to any planar electrodes. I strongly believe that this method has the potential to be used for many electrode-based microfluidic devices and sensors (Sharma *et al.* 2016; Galvan *et al.* 2018).

I have demonstrated the rapid and selective electrokinetic concentration of bacteria, viruses, and proteins on two coplanar electrodes via superimposition of AC EO with DEP. The superimposed signals moved the particles distant from the electrodes toward the high electric field area with EO irrespective of the particle size, and then captured the particles selectively at a particular position, i.e., the highest electric field spot, against the flow with pDEP. Significantly more bacteria were captured using the superimposed signals than were collected using the other two treatments, EO and DEP. Moreover, the bacteria were selectively and rapidly concentrated with high purity against polystyrene beads from the mixture. The concentrations of collected nanometer-sized biological particles such as MS2 viruses and cTnI-Ab proteins were also enhanced by using this superimposition (EO + DEP) technique. This technique allowed for a relatively large gap between two electrodes and short electric field exposure time, and high capture efficiency. I strongly believe that the superimposition of AC EO and DEP can be applied to many biosensors requiring the rapid detection of biological particles with simple coplanar electrodes (Gong 2010; Sharma *et al.* 2016).

An integrated microfluidic immunosensor platform was presented with serial EHD focusing, DEP concentration, and FET-based electrical detection through bio-functionalized SWCNTs for continuous monitoring of flowing label-free *S. aureus*. The EHD focusing incorporated a combination of AC EO and nDEP to reduce transportation losses to the channel surfaces via signal superimposition. In the feasibility test, more 380-nm-diameter polystyrene beads (approximately 15 times) were concentrated on the detection area with EHD focusing than without focusing, thereby showing the potential for detecting large-sized viruses with the proposed microfluidic immunosensor

platform. Quantification of label-free *S. aureus* in 0.01× PBS with similar electrical properties to tap water was also performed with this platform, showing high linearity (R^2=0.956), enhanced LOD of 150 CFU/mL, capture and detection time of 35 min, and high level of specificity to *S. aureus* against *S. epidermidis*, *E. coli* C3000, and *B. subtilis* through electrical (EHD focusing and DEP concentration) manipulation and biological (antibody and blocking agent) interaction.

References

Ai, Y., Sanders, C. K., Marrone, B. L. Separation of *Escherichia coli* Bacteria from Peripheral Blood Mononuclear Cells Using Standnig Surface Acoustic Waves. *Anal Chem* **85**, 9126-9134 (2013).

Albrecht, D. R., Sah, R. L., Bhatia, S. N. Geometric and Material Determinants of Patterning Efficiency by Dielectrophoresis. *Biophys. J.* **87**, 2131-2147 (2004).

Asami, K., Hanai, T., Koizumi, N. *Biophys. J.* **31**, 215-228 (1980).

Ausubel, F. M. *et al. Current Protocols in Molecular Biology* (John Wiley & Sons, Inc., 2003).

Becker, F. F. *et al.* Separation of human breast cancer cells from blood by differential dielectric affinity. *Proc. Natl. Acad. Sci. USA* **92**, 860-864 (1995).

Brown, A. D. B., Smith, C. G., Rennie, A. R. Pumping of water with ac electric fields applied to asymmetric pairs of microelectrodes. *Phys. Rev. E* **63**, 016305 (2000).

Camacho-Alanis, F., Ros, A. Protein dielectrophoresis and the link to dielectric properties. *Bioanalysis* **7**, 353-371 (2015).

Castellanos, A., Ramos, A., Gonzalez, A., Green, N. G., Morgan, H. Electrohydrodynamics and dielectrophoresis in microsystems: scaling laws. *J. Phys. D: Appl. Phys.* **36**, 2584-2597 (2003).

Chen, J.-K., Weng, C.-N., Yang, R.-J. Assessment of three AC electroosmotic flow protocols for mixing in microfluidic channel. *Lab Chip* **9**, 1267-1273 (2009).

Chen, J.-L., Shih, W.-H., Hsieh, W.-H. AC electro-osmotic micromixer using a face-to-face, asymmetric pair of planar electrodes. *Sens. Actuators B: Chem.* **188**, 11-21 (2013).

Chen, Q., Cao, Z., Yuan, Y. J. Study on non-bioparticles and *Staphylococcus aureus* by dielectrophoresis. *RSC Adv.* **10**, 2598-2614.

Chen, Q., Yuan, Y. J. A review of polystyrene bead manipulation by dielectrophoresis. R*SC Adv.* **9**, 4963-4981.

Cheng, I.-F., Chang, H.-C., Chen, T.-Y., Hu, C., Yang, F.-L. Rapid (<5 min) identification of pathogen in human blood by electrokinetic concentration and surface-enhanced raman spectroscopy. *Sci. Rep.* **3**, 2365-2372 (2013).

Cheng, I.-F., Froude, V. E., Zhu, Y., Chang, H.-C., Chang, H.-C. A continuous high-throughput bioparticle sorter based on 3D traveling-wave dielectrophoresis. *Lab Chip* **9**, 3193-3201 (2009).

Chou, C.-F., Tegenfeldt, J. O., Bakajin, O., Chan, S. S., Cox, E. C., Darnton, N., Duke, T., Austin, R. H. *Biophys. J.* **83**, 2170-2179 (2002).

Couniot, N., Francis, L. A., Flandre, D. Resonant dielectrophoresis and electrohydrodynamics for high-sensitivity impedance detection of whole-cell bacteria. *Lab Chip* **15**, 3183-3191 (2015).

Cruz, J., Graells, T., Wallden, M., Hjort, K. Inertial focusing with sub-micron resolution for separation of bacteria. *Lab Chip* **19**, 1257-1266 (2019)

Cui, H.-H., Voldman, J., He, X.-F., Lim, K.-M. Separation of particles by pulsed dielectrophoresis. *Lab Chip* **9**, 2306-2312 (2009).

Das, C. M., Becker, F., Vernon, S., Noshari, J., Joyce, C., Gascoyne, P. R. C. Dielectrophoretic Segregation of Different Human Cell Types on Microscope Slides. *Anal. Chem.* **77**, 2708-2719 (2005).

Dash, S., Mohanty, S., Dielectrophoretic separation of micron and submicron particles: a review. *Electrophoresis* **35**, 2656-2672 (2014).

Dastider, S. G., Barizuddin, S., Dweik, M., Almasri, M. A micromachined impedance biosensor for accurate and rapid detection of *E. coli* O157:H7. *RSC Adv.* **3**, 26297-26306 (2013).

Del Moral-Zamora, B., Punter-Villagrassa, J., Oliva-Brañas, A. M., Álvarez-Azpeitia, J. M., Colomer-Farrarons, J., Samitier, J., Homs-Corbera, A., Miribel-Català, P. L. Combined dielectrophoretic and impedance system for on-chip controlled bacteria concentration: Application to *Escherichia coli*. *Electrophoresis*, **36**, 1130-1141 (2015).

Demircan, Y., Koyuncuoglu, A., Erdem, M., Ozgur, E., Gunduz, U., Kulah, H. Label-free detection of multidrug resistance in K562 cells through isolated 3D-electrode dielectrophoresis. *Electrophoresis* **356**, 1149-1157 (2015).

Ding, X., Li, P., Lin, S.-C. S., Stratton, Z. S., Nama, N., Guo, F., Slotcavage, D., Mao, X., Shi, J., Costanzo, F., Huang, T. J. Surface acoustic wave microfluidics. *Lab Chip* **13**, 3626-3649 (2013).

Dürr, M., Kentsch, J., Müller, T., Schnelle, T., Stelzle, M. Microdevices for manipulation and accumulation of micro- and nanoparticles by dielectrophroesis. *Electrophoresis* **24**, 722-731 (2003).

Elitas, M., Martinez-Duarte, R., Dhar, N., McKinney, J. D., Renaud, P. Dielectrophoresis-based purification of antibiotic-treated bacterial subpopulations. *Lab Chip* **14**, 1850 (2014).

Feldman, H. C., Sigurdson, M., Meinhart, C. D. AC electrothermal enhancement of heterogeneous assays in microfluidics. *Lab Chip* **7**, 1553-1559 (2007).

Freedman, K., Otto, L. M., Ivanov, A. P., Barik, A., Oh, S.-H., Edel, J. B. Nanopore sensing at ultra-low concentrations using single-molecule dielectrophoretic trapping. *Nat. Commun.* **7**, 10217 (2015).

Gadish, N., Voldman, J. High-throughput positive dielectrophoretic bioparticle microconcentrator. *Anal. Chem.* **78**, 7870-7876 (2006).

Gagnon, Z., Chang, H.-C. Aligning fast alternating current electroosmotic flow fields and characteristic frequencies with dielectrophoretic traps to achieve rapid bacteria detection. *Electrophoresis* **26**, 3725-3737 (2005).

Gagnon, Z., Mazur, J., Chang, H.-C. Integrated AC electrokinetic cell separation in a closed-loop device. *Lab Chip* **10**, 718-726 (2010).

Galvan, D.D., Parekh, V., Liu, E., Liu, E.-L., Yu, Q. Sensitive Bacterial Detection via Dielectrophoretic-Enhanced Mass Transport Using Surface-Plasmon-Resonance Biosensors (2018).

Gitis, V., Adin, A., Nasser, A., Gun, J., Lev, O. Fluorescent dye labeled bacteriophages – a new tracer for the investigation of viral transport in porous media: 1. introduction and characterization. *Water Res.* **36**, 4227-4234 (2002).

Godin, M., Bryan, A. K., Burg, T. P. Measuring the mass, density, and size of particles and cells using a suspended microchannel resonator. *Appl. Phys. Lett.* **91**, 123121 (2007).

Gong, J.-R. Label-free attomolar detection of proteins using integrated nanoelectronic and electrokinetic devices. *Small* **6**, 967-973 (2010).

Green, N. G., Morgan, H., Milner, J. J. Manipulation and trapping of sub-micron bioparticles using dielectrophoresis. *J. Biochem. Biophys. Methods* **35**, 89-102 (1997).

Green, N. G., Ramos, A., Gonzalez, A., Castellanos, A., Morgan, H. Electric field induced fluid flow on microelectrodes: the effect of illumination. *J. Phys. D: Appl. Phys.* **33**, L13-L17 (2000).

Green, N. G., Ramos, A., Gonzalez, A., Castellanos, A., Morgan, H. Electrothermally induced fluid flow on microelectrodes. J. Electrostat. 53, 71-87 (2001).

Green, N. G., Ramos, A., Morgan, H. Numerical solution of the dielectrophoretic and travelling wave forces for interdigitated electrode arrays using the finite element method. *J. Electrostat.* **56**, 235-254 (2002).

Hamada, R., Takayama, H., Shonishi, Y., Mao, L., Nakano, M., Suehiro, J. A rapid bacteria detection technique utilizing impedance measurement combined with positive and negative dielectrophoresis. *Sens. Actuator. B-Chem.* **181**, 439-445 (2013).

Han, C.-H., Ha, H. W., Jang, J. Two-dimensional computational method for generating planar electrode patterns with enhanced volumetric electric fields and its application to continuous dielectrophoretic bacterial capture. *Lab Chip* **19**, 1772 (2019).

Han, C.-H., Jang, J. Integrated microfluidic platform with electrohydrodyamic focusing and carbon nanotubes-based field-effect transistor immunosensor for continuous, selective, and label-free quantification of bacteria. *Lab Chip* accepted (2020).

Han, C.-H., Woo, S. Y., Bhardwaj, J., Sharma, A., Jang, J. Rapid and selective concentration of bacteria, viruses, and proteins using alternating current signal superimposition on two coplanar electrodes. *Sci. Rep.* **8**, 14942 (2018).

Han, C.-H., Woo, S. Y., Sharma, A., Jang, J. Rapid and selective electrokinetic concentration of bacteria using AC signal superposition on two coplanar electrodes. In *proceedings of the 21st international conference on miniaturized systems for chemistry and life sciences (MicroTAS 2017)*, Oct 22-26, 1315-1317 (2017).

Han, S.-I., Joo, Y.-D., Han, K.-H. An electrorotation technique for measuring the dielectric properties of cells with simultaneous use of negative quadrupolar dielectrophoresis and electrorotation. *Analyst* **138**, 1529 (2013).

Heeren, A., Luo, C. P., Henschel, W., Fleischer, M., Kern, D. P. Manipulation of micro- and nano-particles by electro-osmosis and dielectrophoresis. *Microelectron. Eng.* **84**, 1706-1709 (2007).

Hölzel, R., Calander, N., Chiragwandi, Z., Willander, M., Bier, F. F. Trapping single molecules by dielectrophoresis. *Phys. Rev. Lett.* **95**, 128102 (2005).

Honegger, T., Peyrade, D. Moving pulsed dielectrophoresis. *Lab Chip* **13**, 1538 (2013).

Huang, C.-C., Bazant, M. Z., Thorsen, T. Ultrafast high-pressure AC electro-osmotic pumps for portable biomedical microfluidics. *Lab Chip* **10**, 80-85 (2010).

Hunag, Y., Ewalt, K. L., Tirado, M., Haigis, R., Forster, A., Ackley, D., Heller, M. J., O'Connell, J. P., Krihak, M. Electric Manipulation of Bioparticles and Macromolecules on Microfabricated Electrodes. *Anal. Chem.* **73**, 1549-1559 (2001).

Hughes, M. P., Morgan, H. Dielectrophoretic trapping of single sub-micrometre scale bioparticles. *J. Phys. D: Appl. Phys.* 31, 2205-2210 (1998).

Iswardy, E., Tsai, T.-C., Cheng, I-F., Ho, T.-C., Perng, G. Ch., Chang, H.-C. A bead-based immunofluorescence-assay on a microfluidic dielectrophoresis platform for rapid dengue virus detection. *Biosens. Bioelectron.* **95**, 174-180 (2017).

Jiang, W., Saxena, A., Song, B., Ward, B. B., Beveridge, T. J., Myneni, S. C. B. Elucidation of Functional Groups on Gram-Positive and Gram-Negative Bacterial Surfaces Using Infrared Spectroscopy. *Langmuir* **20**, 11433-11442 (2004).

Johari, J., Hübner, Y., Hull, J. C., Dale, J. W., Hughes, M. P. Dielectrophoretic assay of bacterial resistance to antibiotics. *Phys. Med. Biol.* **48**, N193-N198 (2003).

Khoshmanesh, K., Zhang, C., Tovar-Lopez, F. J., Nahavandi, S., Baratchi, S., Kalantar-zadeh, K., Mitchell, A. Dielectrophoretic manipulation and separation of microparticles using curved microelectrodes. *Electrphoresis* **30**, 3707-3717 (2009).

Kim, M., Jung, M., Kim, Y.., Lee, C., Woo, K., Yang, J. H., Yang, S. A microfluidic device for label-free detection *Escherichia coli* in drinking water using positive dielectrophoretic focusing, capturing, and impedance measurement. *Biosens. Bioelectron.* **74**, 1011-1015 (2015).

Kim, U., Soh, H. T. Simultaneous sorting of multiple bacterial targets using integrated dielectrophoretic-magnetic activated cell sorter. *Lab Chip* **9**, 2313-2318 (2009).

Kinio, S., Mills, J. K. Design of optimal electrode geometries for dielectrophoresis using fitness based on simplified particle trajectories. *Biomed. Microdevices* **18**, 69 (2016).

Kumemura, M. *et al.* Single-DNA-molecule trapping with silicon nanotweezers using pulsed dielectrophoresis. *J. Micromech. Microeng.* **21**, 054020 (2011).

Kuzmanovic, D. A., Elashvili, I., Wick, C., O'Connell, C., Krueger, S. Bacteriaphage MS2: molecular weight and spatial distribution of the protein and RNA components by small-angle neutron scattering and virus counting. *Structure* **11**, 1339-1348 (2003).

Lapizco-Encinas, B. H., Simmons, B. A., Cummings, E. B., Fintschenko, Y. Dielectrophoretic concentration and separation of live and dead bacteria in an array of insulators. *Anal. Chem.* **76**, 1571-1579 (2004).

Leahy, S., Lai, Y. A cantilever biosensor exploiting electrokinetic capture to detect *Escherichia coli* in real time. *Sens. Actuator. B-Chem.* **238**, 292-297 (2017a).

Leahy, S., Lai, Y. A cantilever biosensor based on a gap method for detecting *Escherichia coli* in real time. *Sens. Actuator. B-Chem.* **246**, 1011-1016 (2017b).

Lee, W. C., Lee, H., Lim, J., Park, Y. J. An effective electrical sensing scheme using AC electrothermal flow on a biosensor platform based on a carbon nanotube network. *Appl. Phys. Lett.* **109**, 223701 (2016).

Liang, E., Smith, R. L., Clague, D. S. Dielectrophoretic manipulation of finite sized species and the importance of the quadrupolar contribution. *Phys. Rev. E* **70**, 066617 (2004).

Liao, K.-T., Chou, C.-F. Nanoscale molecular traps and dams for ultrafast protein enrichment in high-conductivity buffers. *J. Am. Chem. Soc.* **134**, 8742-8745 (2012).

Li, H., Bashir, R. Dielectrophoretic separation and manipulation of live and heat-treated cells of Listeria on microfabricated devices with interdigitated electrodes. *Sens. Actuators B* **86**, 215-221 (2002).

Li, M., Li, W.H., Zhang, J., Alici, G., Wen, W. A review of microfabrication techniques and dielectrophoretic microdevices for particle manipulation and separation. *J. Phys. D: Appl. Phys.* **47**, 063001 (2014).

Lin, H.-Y., Huang, C.-H., Hsieh, W.-H., Liu, L.-H., Lin, Y.-C., Chu, C.-C., Wang, S.-T., Kuo, I-T., Chau, L.-K., Yang, C.-Y. On-line SERS Detection of Single Bacterium Using Novel SERS Nanoprobes and A Microfluidic Dielectrophoresis Device. *Small* **10**, 4700-4710 (2014).

Lin, S.-C., Tung, Y.-C., Lin, C.-T. A frequency-control particle separation device based on resultant effects of electroosmosis and dielectrophoresis. *Appl. Phys. Lett.* **109**, 053701 (2016).

Liu, J., Jasim, I., Abdullah, A., Shen, Z., Zhao, L., El-Dweik, M., Zhang, S., Almasri, M. An integrated impedance biosensor platform for detection of pathogens in poultry products. *Sci. Rep.* **8**, 16109 (2018).

Liu, T., Sin, M. L. Y., Pyne, J. D., Gau, V., Liao, J. C., Wong, P. K. Electrokinetic stringency control in self-assembled monolayer-based biosensors for multiplex urinary tract infection diagnosis. *Nanomed. Nanotechnol.* **10**, 159-166 (2014).

Loire, S., Kauffmann, P., Mezic, I., Meinhart, C. D. A theoretical and experimental study of ac electrothermal flows. *J. Phys. D: Appl. Phys.* **45**, 185301 (2012).

Madiyar, F. R., Syed, L. U., Culbertson, C. T., Li, J. Manipulation of bacteriophages with dielectrophoresis on carbon nanofiber nanoelectrode arrays. *Electrophoresis* **34**, 1123-1130 (2013).

Manchester, M., Steinmetz, N. F. *Viruses and Nanotechnology* (Springer-Verlag, 2009).

Mao, S., Yu, K., Chang, J., Steeber, D. A., Ocola, L. E., Chen, J. Direct Growth of Vertically-oriented Graphene for Field-Effect Transistor Biosensor. *Sci. Rep.* **3**, 1696 (2013).

Markx, G. H., Pethig, R. Dielectrophoretic separation of cells: continuous separation. *Biotechnol. Bioeng.* **45**, 337-343 (1995).

Maruyama, H., Kotani, K., Masuda, T., Honda, A., Takahata, T., Arai, F. Nanomanipulation of single influenza virus using dielectrophoretic concentration and optical tweezers for single virus infection to a specific cell on a microfluidic chip. *Microfluid. Nanofluid* **10**, 1109-1117 (2011).

Mavrogiannis, N., Crivellari, F., Gagnon, Z. R. Label-free biomolecular detection at electrically displaced liquid interfaces using interfacial electrokinetic transduction (IET). *Biosens. Bioelectron.* **77**, 790-798 (2016).

Melvin, E. M., Moore, B. R., Gilchrist, K. H., Grego, S., Velev, O. D. On-chip collection of particles and cells by AC electroosmotic pumping and dielectrophoresis using asymmetric microelectrodes. *Biomicrofluidics* **5**, 034113 (2011).

Morgan, H., Green, N. G. Dielectrophoretic manipulation of rod-shaped viral particles. *J. Electrostat.* **42**, 279-293 (1997).

Morgan, H., Hughes, M. P., Green, N. G. Separation of submicron bioparticles by dielectrophoresis. *Biophys. J.* **77**, 516-525 (1999).

Nakano, A., Luo, J., F., Ros, A. Temporal and Spatial Temperature Measurement in Insulator-Basd Dielectrophoretic Devices. *Anal. Chem.* **86**, 6516-6524 (2014).

Nakano, A., Ros, A., Protein dielectrophoresis: advances, challenges, and applications. *Electrophoresis* **34**, 1085-1096 (2013).

Oh, J., Hart, R., Capurro, J., Noh, H. Comprehensive analysis of particle motion under non-uniform AC electric fields in a microchannel. Lab Chip 9, 62-78 (2009).

Paez-Aviles, C., Juanola-Feliu, E., Punter-Villagrasa, J., del Moral Zamora, B., Homs-Corbera, A., Colomer-Farrarons, J., Miribel-Catala, P. L., Samitier, J. Combined Dielectrophoresis and Impedance Systems for Bacteria Analysis in Microfludic On-Chip Platforms. *Sensors* **16**, 1514.

Park, J.-S., Song, S.-H., Jung, H.-I. Continuous focusing of microparticles using inertial lift force and vorticity via multi-orifice microfluidic channels. *Lab Chip* **9**, 939-948 (2009).

Park, S., Koklu, M., Beskok, A. Particle trapping in high-conductivity media with electrothermally enhanced negative dielectrophoresis. *Anal. Chem.* **81**, 2303-2310 (2009).

Park, S., Zhang, Y., Wang, T.-H, Yang, S. Continuous dielectrophoretic bacterial separation and concentration from physiological media of high conductivity. *Lab. Chip.* **11**, 2893 (2011).

Pethig, R., Talary, M. S., Lee, R. S. Enhancing traveling-wave dielectrophoresis with signal superposition. *IEEE Eng. Med. Biol. Mag.* **22**, 43-50 (2003).

Pohl, H. A. *Dielectrophoresis* (Cambridge University Press, 1978).

Pohl, H. A. The motion and precipitation of suspensions in divergent electric fields. *J. Appl. Phys.* **22**, 869-871 (1951).

Ramadan, Q., Samper, V., Poenar, D., Liang, Z., Yu, Chen., Lim, T.M. Simultaneous cell lysis and bead trapping in a continuous flow microfluidic device. *Sens. Actuators. B- Chem.* **113**, 944-955 (2006).

Ramos, A., Morgan, H., Green, N. G., Castellanos, A. AC electric-field-induced fluid flow in microelectrodes. *J. Colloid Interface Sci.* **217**, 420-422 (1999).

Ren, Y., Liu, J., Liu, W., Lang, Q., Tao, Y., Hu, Q., Hou, L., Jiang, H. Scaled particle focusing in a microfluidic device with asymmetric electrodes utilizing induced-charge electroosmosis. *Lab Chip* **16**, 2803-2812 (2016).

Ren, Y., Liu, W., Jia, Y., Tao, Y., Shao, J., Ding, Y., Jiang, H. Induced-charge electroosmotic trapping of partiles. *Lab Chip* **15**, 2181 (2015).

Rezanoor, M. W., Dutta, P. Combined AC electroosmosis and dielectrophoresis for controlled rotation of microparticles. *Biomicrofluidics* **10**, 024101 (2016).

Rosenthal, A., Voldman, J. Dielectrophoretic Traps for Single-Particle Patterning. *Biophys. J.* **88**, 2193-2205 (2005).

Sabounchi, P., Morales, A. M., Ponce, P., Lee, L. P., Simmons, B. A., Davalos, R. V. Sample concentration and impedance detection on a microfluidic polymer chip. *Biomed. Microdevices* **10**, 661-670 (2008).

Sadeghian, H., Hojjat, Y., Soleimani, M. Interdigitated electrode design and optimization for dielectrophoresis cell separation actuators. *J. Electrostat.* **86**, 41-49 (2017).

Salari, A., Thompson, T. Recent advances in AC electrokinetic sample enrichment techniques for biosensor development. *Sens. Actuator. B-Chem.* **255**, 3601-3615 (2018).

Sanchis, A., Brown, A. P., Sancho, M., Martinez, G., Sebastian, J. L., Munoz, S., Miranda, J. M. Dielectric Characterization of Bacterial Cells Using Dielectrophoresis. *Bioelectromagnetics* **28**, 393-401 (2007).

Sanghavi, B. J., Varhue, W., Rohani, A., Liao, K.-T., Bazydlo, L. A. L., Chou, C.-F., Swami, N. S. Ultrafast immunoassays by coupling dielectrophoretic biomarker enrichment in nanoslit channel with electrochemical detection on graphene. *Lab Chip* **15**, 4563-4570 (2015).

Sang, S., Feng, Q., Jian, A., Li, H., Ji, J., Duan, Q., Zhang, W., Wang, T. Portable microsystem integrates multifunctional dielectrophoresis manipulations and a surface stress biosensor to detect red blood cells for hemolytic anemia. *Sci. Rep.* **6**, 33626 (2016).

Sasaki, N., Kitamori, T., Kim, H.-B. AC electroosmotic micromixer for chemical processing in a microchannel. *Lab Chip* **6**, 550-554 (2006).

Sharma, A., Han, C.-H., Jang, J. Rapid electrical immunoassay of the cardiac biomarker troponin I through dielectrophoretic concentration using imbedded electrodes. *Biosens. Bioelectron.* **82**, 78-84 (2016).

Song, H., Bennett, D. J. An Analytical Method for Dielectrophoresis and Traveling Wave Dielectrphoresis Generated by an n-Phase Interdigitated Parallel Electrode Array. *J. Fluids Eng.* **130**, 081605 (2008).

Studer, V., Pepin, A., Chen, Y., Ajdari, A. An integrated AC electrokinetic pump in a microfluidic loop for fast and tunable flow control. *Analyst* **129**, 944-949 (2004).

Suehiro, J., Shutou, M., Hatano, T., Hara, M. High sensitive detection of biological cells using dielectrophoretic impedance measurement method combined with electropermeabilization. *Sens. Actuator. B-Chem.* **96**, 144-151 (2003).

Swaminathan, V. V., Shannon, M. A., Bashir, R. Enhanced sub-micron colloidal particle separation with interdigitated microelectrode arrays using mixed AC/DC dielectrophoretic scheme. *Biomed. Microdevices* **17**, 29 (2015).

Tada, S., Nakanishi, A., Eguchi, M., Ochi, K., Baba, M., Tsukamoto, A. Enhancement of continuous-flow separation of viable/nonviable yeast cells using a nonuniform alternating current electric field with complex spatial distribution. *Biomicrofluidics* **10**, 034110 (2016).

Valero, A., Braschler, T., Demierre, N., Renaud, P. A. Miniaturized continuous dielectrophoretic cell sorter and its applications. *Biomicrofluidics* **4**, 022807 (2010).

Voldman, J. Dielectrophoretic traps for cell manipulation. *BioMEMS Biomed. Nanotechnol.* **4**, 159-186 (2006).

Voldman, J., Gray, M. L., Toner, M., Schmidt, M. A. A Microfabrication-Based Dynamic Array Cytometer. *Anal. Chem.* **74**, 3984-3990 (2002).

Wasik, D., Mulchandani, A., Yates, M. V. Point-of-Use Nanobiosensor for Detection of Dengue Virus NS1 Antigen in Adult Aedes Aegypti: A Potential Tool for Improved Dengue Surveillance. *Anal. Chem.* **90**, 679-684 (2018).

Wang, X.-B., Hunag, Y., Wang, X., Becker, F.F., Gascoyne, P.R.C. Dielectrophoreic Manipulation of Cells with Spiral Electrodes. *Biophys. J.*, **72**, 1887-1899 (1997).

Wang, X.–B., Vykoukal, J., Becker, F. F., Gascoyne, P. R. C. Separation of polystyrene microbeads using dielectrophoretic/gravitational field-flow-fractionation. *Biophys. J.* **74**, 2689-2701 (1998).

Wei, Z., Li, X., Zhao, D., Yan, H., Hu, Z., Liang, Z., Li, Z. Flow-Through Cell Electroporation Microchip Integrating Dielectrophoretic Viable Cell Sorting. *Anal. Chem.* **86**, 10215-10222 (2014).

Wu, G., Dai, Z., Tang, X., Lin, Z., Lo, P. K., Meyyappan, M., Lai, K. W. C. Graphene Field-Effect Transistors for the Sensitive and Selective Detection of *Escherichia coli* Using Pyrene-Tagged DNA Aptamer. *Adv. Healthcare Mater.*, 1700736 (2017).

Williams, E. H. *et al.* Selective streptavidin bioconjugation on silicon and silicon carbide nanowires for biosensor applications. *J. Mater. Res.* **28**, 68-77 (2013).

Yang, J., Huang, Y., Wang, X.-B., Becker, F. F., Gascoyne, P. R. C. Differential analysis of human leukocytes by dielectrophoretic field-flow-fractionation. *Biophys. J.* **78**, 2680-2689 (2000).

Yang, L., Banada, P. P., Chatni, M. R., Lim, K. S., Bhunia, A. K., Ladisch, M., Bashir, R. A multifunctional micro-fluidic system for dielectrophoretic concentration coupled with immune-capture of low numbers of *Listeria monocytogenes*. *Lab Chip* **6**, 896-905 (2006).

Yang, L., Bashir, R. Electrical/electrochemical impedance for rapid detection of foodborne pathogenic bacteria. *Biotechnol. Adv.* **27**, 135-150 (2008).

Yoon, G. H., Park, J. Topological design of electrode shapes for dielectorphoresis based devices. *J. Electrostat.* **68**, 475-486 (2010).

Zellner, P., Shake, T., Sahari, A., Behkam, B., Agah, M. Off-chip passivated-electrode, insulator-based dielectrophoresis. *Anal. Bioanal. Chem.* **402**, 6657-6666 (2013).

Zhou, H., White, L. R., Tilton, R. D. Lateral separation of colloids or cells by dielectrophoresis augmented by AC electroosmosis. *J. Colloid Interface Sci.* **285**, 179-191 (2005).

Zhou, J., Lin, J., Zhou, C., Deng, X., Xia, B. Cytotoxicity of red fluorescent protein DsRed is associated with the suppression of Bcl-xL translation. *FEBS Lett.* **585**, 821-827 (2011).

Acknowledgements

My deep gratitude goes first to my advisor, Prof. Jaesung Jang. Starting from my undergraduate research intern period, he guided and inspired me to become an independent researcher. It was lucky to meet such a generous and true mentor in my life. I deeply respect my advisor for his enthusiasm on research and positive advising, etc. I always wish his health and happiness. Also, I appreciate the committee members of my dissertation, Prof. Hyungson Ki, Prof. Taesung Kim, Prof. Sung Kuk Lee and Prof. Joo Hun Kang at Ulsan National Institute of Science and Technology (UNIST), for giving me the valuable comments and making time for my doctoral defense. In addition, I am grateful to UNIST and National Research Foundation of Korea for funding my research.

I would like to thank my coworkers who did experiments, analysis, writing manuscript, or discussion with me. I am thankful to Dr. Seongkyeol Hong who was a kind senior with teaching and helping me a lot for my adaptation in the laboratory, and his diligence and patience motivated me. I acknowledge Dr. Abhinav Sharma for developing new biosensors together and giving me valuable advices for my research. I am thankful to Seong Yong Woo for making a voltage adder and helping me for the connection of electrical devices and instruments. I thank Dr. Jyoti Bhardwaj and Chanhwi Park for preparing virus-laden samples and the corresponding plaque assay. Thank you for your effort of microfabrications of chips and alignments of carbon nanotubes, Daesoon Lee and Woojin Park. Discussion about bioaerosols with Junbeom Jang and Jaegil Lee was helpful as well. I acknowledge the students from Daegu Science High School and Busan Science High School during the research and education program from 2013 to 2017, for sharing many creative and active opinions to develop new devices. I thank the staff in UNIST Central Research Facilities for their help in microfabrications.

I want to thank the students and alumni of our Sensors and Aerosols Laboratory: Myeong-Woo Kim, Nhan Dihn Ngo, Wonyoung Jeon, Minju Cha, Hyeona Lee, Dr. Renu Singh, Sivaranjani Devarakonda, Dr. Jeonghyun Kim, Prof. SangJun Moon and Prof. Suveen Kumar. Especially Sivaranjani was somewhat mischievous to me and vice versa, but our funny memory helped me a lot for making my days in laboratory not boring.

I am thankful to my school colleagues during my graduate period in the Department of Mechanical Engineering at UNIST, Dr. Hoon Yi, Dr. Jiyun Jeon, Dr. Jongwan Lee, Kangik Cho, Beomsang Kim, Dr. Dogyeong Ha and Dr. Haram Yeo. We encouraged ourselves each other a lot for our graduate researches, and many kind words from them comforted me indeed.

I want to thank my undergraduate friends in UNIST, Cheolwoo Cho, Taehyun Kim, Junsu Park, Donghyeok Kim, Dr. Woo Cheol Jeon and Hagyeong Seo. My campus life was not lonely nor boring with them in dormitory, campus and Guyeong-ri.

And I say hello to my friends from Sangsan High School, Jaehyeon Yoo, Karam Cho, Suho Yun, C.P.A., Sung Bin Han, M.D., Changwoo Oh and Yeong-jin Jang. We were together in the period

of preparing university entrance, and the valuable moments we shared were helpful for keeping my study going on.

I would like to thank the members of MENSA Korea for our valuable social activities to contribute to a better world.

I am always grateful to my brave childhood friend Su Won Im for saving me from drowning in a river. I owe you my life.

Lastly, I deeply thankful to my family. Thank you my younger sister Yoon Jeong Han and my uncle Ilsoo Yoon. I am infinitely grateful to my grandmother Jeong Ok Lee, my grandfather Jong Ryeol Yoon and my mother Moonsoo Yoon.

Curriculum Vitae

Chang-Ho Han, Ph.D.

Postdoctoral Researcher
Department of Mechanical Engineering
Ulsan National Institute of Science and Technology (UNIST), Ulsan 44919, Republic of Korea (S. Korea)
Mobile: +82-10-4764-7544
E-mail: chhanrok@gmail.com

Research Interests

- Electrokinetics
- Microfluidic Biosensors and Biomedical Devices
- Hydrodynamic and Aerodynamic Particle-Fluid Dynamics
- Optimization Methods

Education

- **Doctor of Philosophy** *Advisor: Prof. Jaesung Jang* Mar. 2014 – Feb. 2021
  Department of Mechanical Engineering, UNIST, Ulsan, Korea
  Dissertation title: Electrokinetics-assisted electrical sensors for rapid detection of bacteria
- **Bachelor of Science** Mar. 2010 – Feb. 2014
  School of Mechanical and Advanced Materials Engineering, UNIST, Ulsan, Korea

Research Experience

- **Graduate Research Assistant** Mar. 2014 – Feb. 2021
  Sensors & Aerosols Lab. (Prof. Jaesung Jang)
  Department of Mechanical Engineering, UNIST, Ulsan, Korea
- **Undergraduate Research Intern** May. 2012 – Feb. 2014
  Sensors & Aerosols Lab. (Prof. Jaesung Jang)
  School of Mechanical and Advanced Materials Engineering, UNIST, Ulsan, Korea

Skills

- **Programming/Simulation Software**: MATLAB, COMSOL Multiphysics, ANSYS Fluent, etc.
- **Microfabrication**: Photolithography, Chemical Vapor Deposition, Sputtering, Etching, etc.
- **Language**: Korean (native), English, Japanese

Publications

[*: corresponding author]

International Peer-Reviewed Journal Papers

(First authorship)

[4] **C.-H. Han**, C. Park, W. Park, D. Lee, J. Jang*, 2021, "Investigation of dielectrophoretic behaviors of various label-free viruses using a carbon-nanotube-based field-effect transistor sensor" (in preparation).

[3] **C.-H. Han**, J. Jang*, 2020, "Integrated microfluidic platform with electrohydrodynamic focusing and carbon nanotubes-based field-effect transistor immunosensor for continuous, selective, and label-free quantification of bacteria," *Lab on a Chip* (in press).

[2] **C.-H. Han**, H. W. Ha, J. Jang*, 2019, "Two-dimensional computational method for generating planar electrode patterns with enhanced volumetric electric fields and its application to continuous dielectrophoretic bacterial capture," *Lab on a Chip*, 19, 1772-1782 [Back Cover].

[1] **C.-H. Han**, S. Y. Woo, J. Bhardwaj, A. Sharma, J. Jang*, 2018, "Rapid and selective concentration of bacteria, viruses, and proteins using alternating current signal superimposition on two coplanar electrodes," *Scientific Reports*, 8, 14942.

(Co-authorship)

[3] J. Bhardwaj, S. Hong, **C.-H. Han**, J. Lee, J. Jang, J. Jang*, 2021, "Recent advancement on measurements of pathogenic airborne viruses: review" (in preparation).

[2] S. Hong, J. Bhardwaj, **C.-H. Han**, J. Jang*, 2016, "Gentle Sampling of Submicronmeter Airborne Virus Particles Using a Personal Electrostatic Particle Concentrator," *Environmental Science and Technology*, 50, 12365-12372.

[1] A. Sharma, **C.-H. Han**, J. Jang*, 2016, "Rapid electrical immunoassay of the cardiac biomarker troponin I through dielectrophoretic concentration using imbedded electrodes," *Biosensors and Bioelectronics*, 82, 78-84 [News Broadcast].

International Conference Presentations and Posters

(First authorship)

[6] **C.-H. Han**, J. Jang*, 2021, "Electrokinetics-enhanced, label-free, selective, and electrical quantification of bacteria using a microfluidic sensor platform," *Biosensors 2020*, Jul. 26-29, Busan Exhibition & Convention Center (BEXCO), Busan, Korea.

[5] **C.-H. Han**, H. W. Ha, J. Jang*, 2018, "Microelectrode Discretization Method to Enhance Dielectrophoretic Forces in a Microfluidic Device," *The 10th International Symposium on Microchemistry and Microsystems (ISMM 2018)*, Jun. 19-21, Hanwha Resort Haeundae Tivoli, Busan, Korea [Best Poster Award].

[4] **C.-H. Han**, J. Jang*, 2018, "Enhanced Dielectrophoretic Capture of Submicron Particles using Continuous Electrohydrodynamic Focusing in a Microfluidic Device," *The 13th Annual Institute of Electrical and Electronics Engineers (IEEE) International Conference on Nano/Micro Engineered and Molecular Systems (IEEE-NEMS 2018)*, Apr. 22-26, Grand Hyatt Singapore, Singapore.

[3] **C.-H. Han**, S. Y. Woo, A. Sharma, J. Jang*, 2017, "Rapid and Selective Electrokinetic Concentration of Bacteria Using AC Signal Superposition on Two Coplanar Electrodes," *The 21st International Conference*

on Miniaturized Systems for Chemistry and Life Sciences (MicroTAS 2017), Oct. 22-26, Savannah International Trade & Convention Center, Savannah, Georgia, the United States of America (USA).

[2] **C.-H. Han**, J. Jang*, 2016, "High-throughput alternating current electrohydrodynamic particle separator having convection and separation electrodes," *Biosensors 2016*, May. 25-27, Svenska Massan, Gothenburg, Sweden.

[1] **C.-H. Han**, H. W. Ha, J. Jang*, 2015, "Microelectrode Discretization (MED) Method for a Dielectrophoretic Particle Collector," *The 9th IEEE International Conference on Nano/Molecular Medicine and Engineering (IEEE-NANOMED 2015)*, Nov. 15-18, Waikiki Beach, Hawaii, USA.

(Co-authorship)

[4] A. Sharma, **C.-H. Han**, J. Jang*, 2016, "Rapid Electrical Immunoassay of the Cardiac Biomarker Troponin I through Dielectrophoretic Concentration," *The 4th International Conference on Electronic Materials and Nanotechnology for Green Environment (ENGE 2016)*, Nov. 6-9, Ramada Plaza Jeju Hotel, Jeju, Korea [Invited Talk].

[3] S. Hong, **C.-H. Han**, J. Jang*, 2016, "Gentle Sampler of Submicron Airborne Viruses via Electrostatic Forces," *American Association for Aerosol Research (AAAR) 35th Annual Conference*, Oct. 17-21, Oregon Convention Center, Portland, Oregon, USA.

[2] A. Sharma, **C.-H. Han**, S. Hong, J. Jang*, 2015, "Rapid Electrical Concentration and Detection of Cardiac Biomarker Troponin I," *The 9th IEEE International Conference on Nano/Molecular Medicine and Engineering (IEEE-NANOMED 2015)*, Nov. 15-18, Waikiki Beach, Hawaii, USA.

[1] S. Hong, H. Lee, **C.-H. Han**, J. Jang*, 2014, "New Electrostatic Aerosol Concentrator for Bioaerosol Detection," *2014 International Aerosol Conference (IAC 2014)*, Aug. 28 - Sep. 2, BEXCO, Busan, Korea.

Domestic Conference Presentations and Posters

(First authorship)

[12] **C.-H. Han**, S. Y. Woo, J. Bhardwaj, A. Sharma, J. Jang*, 2019, "Rapid and selective concentration of bacteria, viruses, and proteins using alternating current signal superimposition of dielectrophoresis and electroosmosis," *2019 Korean Society of Mechanical Engineers (KSME) Ulsan Spring Annual Meeting*, May. 24, University of Ulsan, Ulsan, Korea (in Korean: 유전영동과 전기삼투의 교류 신호 중첩을 이용한 박테리아, 바이러스, 프로틴의 신속하고 선택적인 채집).

[11] **C.-H. Han**, S. Y. Woo, A. Sharma, J. Jang*, 2018, "Collection of Bacteria on Two Coplanar Electrodes using AC Signal Superimposition," *2018 KSME Spring Annual Meeting*, May. 24-25, Pukyong National University, Busan, Korea (in Korean: 교류 신호 중첩을 이용한 공면 전극쌍으로의 박테리아 채집).

[10] **C.-H. Han**, G. H. Kim, D. Kim, J. H. Park, J. Y. Ha, J. Jang*, 2017, "Continuous Electrohydrodynamic Focusing of Particles and Their Enhanced Dielectrophoretic Capture in a Microfluidic Device," *2017 KSME Fall Annual Meeting*, Nov. 1-3, International Convention Center Jeju (ICC Jeju), Jeju, Korea (in Korean: 미세유체 장치에서 입자의 연속적인 전기수력학적 집중 및 향상된 유전영동식 채집).

[9] **C.-H. Han**, D. Kim, J. H. Park, J. Jang*, 2017, "Continuous Particle Collection Based on Dielectrophoresis

Aided by Electrothermal Flow in Electrically High Conductive Media," *2017 KSME Spring Annual Meeting*, May. 25-26, Pukyong National University, Busan, Korea (in Korean: 고전기전도도 용액에서의 전열유동 보조 유전영동 기반 연속적인 입자 채집).

[8] **C.-H. Han**, M.-W. Kim, G. H. Kim, D. Kim, J. H. Park, J. Y. Ha, J. Jang*, 2016, "A Microfluidic Device for Selective Collection of Bacteria Based on AC Dielectrophoresis and Cross-Sectional Electrothermal Flow," *2016 KSME Fall Annual Meeting*, Dec. 14-16, Kangwonland Resort, Jeongseon, Korea (in Korean: 교류 유전영동 및 횡단면 전열유동 기반의 선택적인 박테리아 채집을 위한 미세유체 장치).

[7] **C.-H. Han**, A. Sharma, J. Jang*, 2016, "Dielectrophoretic Bacteria Capture Using Planar Microelectrodes in Wide Ranges of Media Electrical Conductivities," *2016 KSME Spring Annual Meeting*, May. 19-20, Pukyong National University, Busan, Korea (in Korean: 평면 전극을 이용한 넓은 범위의 용액 전기전도도에서의 유전영동식 박테리아 채집).

[6] **C.-H. Han**, M. S. Kim, T. Y. Park, W. G. Jeong, H. W. Ha, J. Jang*, 2015, "Dielectrophoresis and Electroosmosis-Based Electrohydrodynamic Particle Separator using Microfluidic Channel," *2015 KSME Fall Annual Meeting*, Nov. 10-14, ICC Jeju, Jeju, Korea (in Korean: 미세유체 채널을 이용한 유전영동 및 전기삼투 기반의 전기수력학적 입자 분리 장치).

[5] **C.-H. Han**, J. Jang*, 2015, "3D Simulation of a Serpentine Channel Type Small Size Electrostatic Filter for Airborne Particles," *2015 Korean Association for Particle and Aerosol Research (KAPAR) Annual Meeting*, Jul. 8-10, Yongpyong Resort, Pyeongchang, Korea (in Korean: 공기 중 미세입자 여과를 위한 구불구불한 채널 타입 소형 정전기식 필터의 3D 시뮬레이션).

[4] **C.-H. Han**, S. Hong, H. Lee, J. Jang*, 2015, "3D Simulation of an Electrostatic Particle Concentrator (EPC) for Ultrafine Airborne Particles," *2015 KSME Spring Annual Meeting*, May. 21-22, BEXCO, Busan, Korea (in Korean: 공기 중 초미세입자 채집을 위한 정전기식 입자 채집 장치에 대한 3D 시뮬레이션) [Excellent Poster Award].

[3] **C.-H. Han**, M. S. Kim, T. Y. Park, S. J. Lee, W. G. Jeong, H. W. Ha, J. Jang*, 2014, "Design of a Planar Microelectrode Pattern for Dielectrophoresis-based Bacteria Microseparators," *2014 KSME Fall Annual Meeting*, Nov. 11-14, Kimdaejung Convention Center, Gwangju, Korea (in Korean: 유전영동 기반의 박테리아 분리장치의 평면 미세 전극에 대한 설계).

[2] **C.-H. Han**, D. M. Kim, J. H. Song, H. W. Chung, J. U. Heo, J. Jang*, 2014, "3D Simulation of a Dielectrophoretic Bacteria Separator Using a Microfluidic Channel Having Periodic Cross-sectional Areas," *2014 KSME Fall Annual Meeting*, Nov. 11-14, Kimdaejung Convention Center, Gwangju, Korea (in Korean: 단면이 규칙적으로 변하는 미세유체 채널을 이용한 유전영동 기반의 박테리아 분리 장치에 대한 3D 시뮬레이션).

[1] **C.-H. Han**, G. Kim, T. Park, H. Yang, Y. Han, J. Jang*, 2013, "Design and Numerical Analysis of an Electrostatic Filter for Airborne Particles and Viruses," *2013 KSME Fall Annual Meeting*, Dec. 18-20, Kangwonland Resort, Jeongseon, Korea (in Korean: 공기 중 미세입자 및 바이러스 여과를 위한 정전기식 필터의 설계 및 수치해석).

(Co-authorship)

[5] S. Hong, **C.-H. Han**, J. Jang*, 2016, "Collection of Airborne Virus Using Electrostatic Particle Concentrator," *2016 KAPAR Annual Meeting*, Jun. 29 – Jul. 1, ICC Jeju, Jeju, Korea (in Korean: 공기 중 바이러스 채집을 위한 정전식 입자 농축기) [Best Paper Award].

[4] M.-W. Kim, S. Hong, **C.-H. Han**, S.-Y. Lee, J. Jang*, 2015, "Radiative heat flux sensor using two resistance temperature detectors towards smart firefighter's garment," *2015 KSME Fall Annual Meeting*, Nov. 10-14, ICC Jeju, Jeju, Korea (in Korean: 스마트 소방복에 사용될 두 개의 백금 저항 측온기를 이용한 복사열유속 센서).

[3] A. Sharma, **C.-H. Han**, S. Hong, J. Jang*, 2015, "Electrical Detection of Cardiac Biomarker Troponin I via Electrical Concentration," *2015 Korean Society for Biotechnology and Bioengineering (KSBB) Spring Meeting and International Symposium*, Apr. 15-17, Yeosu Expo Convention Center, Yeosu, Korea.

[2] S. Hong, K. Kim, **C.-H. Han**, M.-S. Choi, S.-Y. Lee, J. Jang*, 2014, "Fabrication and Test of Thin Film Pt-RTD Sensors for Smart Firefighting Garment," *2014 KSME Spring Annual Meeting*, May 22-23, Korea Institute of Industrial Technology (KITECH), Ansan, Korea (in Korean: 스마트 화재진압복용 미세 온도센서의 제작 및 시험).

[1] S. Hong, **C.-H. Han**, S.-Y. Lee, J. Jang*, 2013, "Micro Radiation Heat Flux Sensor Using Pt-RTDs and Reflective Films," *2013 KSME Fall Annual Meeting*, Dec. 18-20, Kangwonland Resort, Jeongseon, Korea (in Korean: 측온저항체와 반사필름을 이용한 미세 복사열유속계).

Patents (Registered)

[7] J. Jang, **C.-H. Han**, 2020, "Electrode for dielectrophoresis based particle capture," Korea patent, 10-2156239-0000, Sep. 9 (in Korean: 유전영동기반 입자 채집용 전극).

[6] J. Jang, **C.-H. Han**, 2019, "Electrode for separating particles based on dielectrophoresis and electroosmosis, and an apparatus for separating particles including the same," Korea patent, 10-1947233-0000, Feb. 1 (in Korean: 유전영동과 전기삼투를 이용한 입자 분리 전극 및 이를 포함하는 입자 분리 장치).

[5] J. Jang, **C.-H. Han**, A. Sharma, 2018, "Dielectrophoresis-based biosensor," Korea patent, 10-1866060-0000, Jun. 1 (in Korean: 유전영동 기반의 바이오 센서).

[4] J. Jang, S. Hong, **C.-H. Han**, S.-Y. Lee, 2017, "Radiative heat flux sensor device," Korea patent, 10-1778841-

0000, Sep. 8 (in Korean: 복사열유속 측정 장치).

[3] J. Jang, **C.-H. Han**, H. W. Ha, 2016, "Electrode generation method for dielectrophoresis based particles separation or capture," Korea patent, 10-1693103-0000, Dec. 29 (in Korean: 유전영동기반 입자 분리 및 채집 장치용 전극 생성 방법).

[2] J. Jang, **C.-H. Han**, 2015, "Dielectrophoresis based particle separator using serpentine channel," Korea patent, 10-1561693-0000, Oct. 13 (in Korean: 격벽 구조를 갖는 유전영동 기반의 입자 분리 장치).

[1] J. Jang, **C.-H. Han**, 2015, "Small-sized electrostatic airborne particle filter," Korea patent, 10-1533839-0000, Jun. 29 (in Korean: 소형 정전기식 미세 입자 필터)

References

- **Jaesung Jang, Ph.D.** (graduate research advisor)
  Professor
  Department of Mechanical Engineering, UNIST, Ulsan, Korea
  E-mail: jjang@unist.ac.kr
- **Taesung Kim, Ph.D.** (doctoral defense committee)
  Professor
  Department of Mechanical Engineering, UNIST, Ulsan, Korea
  E-mail: tskim@unist.ac.kr
- **Hyungson Ki, Ph.D.** (doctoral defense committee)
  Professor
  Department of Mechanical Engineering, UNIST, Ulsan, Korea
  E-mail: hski@unist.ac.kr